UNIVERSITÀ DEGLI STUDI DI MILANO

Scuola di Dottorato in Fisica, Astrofisica e Fisica Applicata
Dipartimento di Fisica

Corso di Dottorato in Fisica, Astrofisica e Fisica Applicata
Ciclo XXXV

Probing band magnetism at different dimensions: energy, spin and time-resolved studies

Settore Scientifico Disciplinare FIS/03

Supervisore: Professor Giorgio ROSSI

Co-supervisore: Dottor Giancarlo PANACCIONE

Coordinatore: Professor Matteo PARIS

Tesi di Dottorato di:
Alessandro De Vita

Anno Accademico 2021-2022

Commission of the final examination:

External Referees:
Prof. Mirko Cinchetti & Prof. Em. Danilo Pescia

External Members:
Prof. Giacomo Ghiringhelli & Prof. Francesco Offi

Internal Member:
Prof. Giorgio Rossi

Final examination:

2nd December 2022

Università degli Studi di Milano, Dipartimento di Fisica, Milano, Italy

To the curiosity and the joy of discovery:
"The final frontier... To boldly go where no man has gone before!"

Cover illustration:
M. C. Escher, *Reptiles*
Internal illustrations:
A. De Vita
Design:
A.D. Copia, Copiae

MIUR subject:
FIS/03

PACS:
73.20.At, 75.25.+z, 75.50.-y, 75.70.-y, 78.47.+p

Contents

Abstract

This thesis completes my work as doctoral student of the Scuola di Dottorato in Fisica, Astrofisica e Fisica Applicata at the Università degli Studi di Milano, that has been carried out since November 2019 at the Istituto Officina dei Materiali of the Consiglio Nazionale delle Ricerche (IOM-CNR) in the premises of the Elettra - Sincrotrone Trieste and FERMI@Elettra infrastructures and in the framework of the NFFA facility.

My experimental activity employed complementary spectroscopy and polarimetry techniques oriented to address the characterisation of electronic and spin properties of systems with decreasing dimensionality. This programme has been conducted by exploiting state-of-the-art infrastructures to generate visible, UV and EUV ultrashort pulses (tabletop lasers and HHG at NFFA-SPRINT laboratory) and soft X-ray synchrotron light (at Elettra, Diamond and ESRF synchrotron light sources).

I used photoemission as the main tool in my investigation, supplementing my results with absorption spectroscopy. I focused on three materials, Fe(001)-p(1x1)O/MgO , $EuSn_2P_2$ and VI_3, of high interest in modern and next-generation magnetic devices.

In the three systems I studied the electronic band structure to identify key features hinting at the bound electrons behaviour. I investigated the properties of the magnetically ordered phases and found evidence of the reduced dimensionality in the emergence of atypical spin ordering and the increasingly manifest electron correlation phenomena. The information retained by band electrons is critical to access the spin polarisation of the bands and to give insight into the effects of spatial confinement on the spin degree of freedom.

Introduction

I am large, I contain multitudes.

Walt Whitman, *Song of Myself*

Magnetism and magnetic materials have been known to mankind since millennia. The first record of a compass is attested in a text written in China between the 5th and the 3rd century BC, as a divination tool: "The magnetic stone attracts and pulls the iron" (Shu-hua, 1954).

The deep comprehension of the true nature of magnetic phenomena requires a piercing insight into the physics and thermodynamics of solid state matter; indeed, our knowledge is far from complete. Yet, the pervasive technological applications of magnetism have contributed by large to shape the modern and interconnected world where we live.

In 1898, Valdemar Poulsen patented the *telegraphone*, the first working sound recorder: a magnetiseable medium moves past a recording head, where it is magnetised by a coil fed by the current from a microphone. The recording of the voice of Emperor Franz Joseph of Austria at the 1900 World's Fair in Paris is the oldest surviving testament of the inauguration of magnetic data storage.

Magnetic materials are perfectly suited for the purposes of storing information: the orientation of the magnetisation "up" or "down" along a direction, determined by an external magnetic field, easily corresponds to the "1" or "0" boolean states in the binary system: a magnetised domain can store a binary digit, or, in its portmanteau form, a *bit*. A measure of the performance of magnetic-based storage devices is the reading/storing speed, *i.e.* the speed at which the bit is manipulated.

The laws of electrodynamics define the speed of switching the magnetisation in a magnetic domain as a consequence of Larmor precession: if a magnetic moment is aligned along the x direction, an external magnetic field along z would force the magnetic moment to precess in the xy plane with frequency $|\gamma \mathrm{H}|/2\pi = 28\,\mathrm{GHz\,T^{-1}}$. When the magnetisation is switched the field is turned off: the time for switching depends entirely on the magnitude of the magnetic field and the reference benchmark in this case is 18 ps for a 1 T field.

This picture holds true for a single electron, but a solid contains $\sim 10^{23}$ electrons per cubic centimetre. The mutual interactions between electrons give rise to completely different timescales for magnetisation switching, described by the Landau-Lifshitz-Gilbert equation. In principle, the limit set by traditional MRAMs can be therefore overcome

and a new generation of devices overtaking the standard of thermodynamic magnetism may rise. But what need is driving the research on this field?

In 2020 the Global DataSphere - the summation of all data created, captured or replicated - amounted to 64.2 ZB, defying the systemic decline stirred by the COVID-19 pandemic. The forecasts for 2025 are constantly adjusted upwards, from 163 ZB (Reinsel, Gantz and Rydning, 2017) to 175 ZB (Reinsel, Gantz and Rydning, 2018) to 181 ZB (Reinsel, Rydning and Gantz, 2021).

The total electricity consumption by Google in 2020 amounted to 15.1 TW h,[1] the vast majority of which is required to power data centres; 2×10^{12} Google searches were carried out globally in 2020; the energy required to compute 300 Google searches equals the energy required to heat 1 l of water up to the boiling point. Global restrictions adopted as countermeasure to the pandemic reshaped the social, economical and digital landscapes, further accelerating the need for efficient and sustainable data processing.

For this reason, the last years have seen a dramatic progress of high-end technology for magnetic data storage. Different paradigms for the realisation of magnetic devices have been applied.

Spin-transfer torque (STT) induces a switch of the electron magnetic moments by means of a spin-polarised current; magnetic tunnel junction-based STT-MRAM came to reality in the late 2010s (K. Lee et al., 2019) and made its way into the industry as a 1000 times faster, 400 times more energy-efficient than its Flash counterparts.

The discovery of magnetisation switching by spin-orbit torque (SOT) by applying an in-plane current through a heavy metal with high spin-orbit coupling was met with great excitement. The next generation of devices based on SOT-MRAM architecture or hybrid SOT+SST, faster than STT-only solutions, may be ready to emerge in the next years (Guo et al., 2021).

In addition, novel spintronic low-power logic components such as magnetoelectric spin-orbit (MESO) devices, where bidirectional spin-charge conversion emerges through magnetoelectric switching and spin-orbit detection of state, could represent a prospective beyond-CMOS solution by drastically reducing the energy consumption to < 10 aJ per bit (Manipatruni et al., 2019).

The last frontier for innovative design lies on the structural engineering of quantum materials. Tailoring the coexistence of topological phases and magnetic order, heterostructuring van der Waals ultrathin films and manipulating crystals at the atomic-scale via strain (A. S. Disa, Nova and Cavalleri, 2021) represent some of the leading archetypes paving the way for next-generation efficient devices, scaled down to unimaginable miniaturisation.

As such, behind the exciting world of novel technology based on the electron and spin degrees of freedom lies the complex universe of magnetism in low dimensions. Magnetism in its very essence is already a pure expression of the quantum character of nature;[2] quantum effects are exacerbated in a spatially confined world, and what we observe in three dimensions (3D) may not necessarily be true for a two-dimensional (2D) material.

When investigating the expressions of magnetism in systems with different dimensionality, the set of fundamental interactions prompting ordered states may be strongly affected by the spatial confinement, due to the competition between order parameters

[1] Google's 2021 Environmental Report.

[2] Despite this, we should never forget the reprimand by Amikam Aharoni, who in the beautiful first pages of his book dedicated to the theory of ferromagnetism writes that "[the Born-van Leeuwen theorem] is very general, and its proof is rigorous. However, it does *not* eliminate all possibility of using classical physics. All it eliminates is the use of *pure* classical physics, which nobody is doing anyway nowadays."

established by thermodynamics. There is no hope for progress in technology without mastery in the understanding of these fundamental interactions; at this point, it should come to no surprise that the scientific quest for exploring their nature and physics is no more a concern, but a necessity.

Thesis overview

In this thesis I employ a combination of spectroscopic techniques to address different systems and how their spatial and electronic configuration deeply affects the onset of long-range magnetic ordering.

This work focuses on the electronic and magnetic properties of three systems. First I measured Fe(001)-p(1x1)O/MgO , a prototypical *3d* ferromagnet. *3d* ferromagnets are widely used in spin-to-charge conversion devices; any application-driven approach should take into consideration the studies on the behaviour of near-Fermi electrons, *i.e.* those that contribute the most to the magnetic character.

Secondly, I worked on the characterisation of $EuSn_2P_2$, a "quantum material by design": this crystal has been specifically engineered to be a candidate axion insulator, where peculiar properties of charge transport and magnetic ordering are supposed to coexist and mutually influence each other. The presence of a strong spin-orbit coupling, long-range ferromagnetism and non-trivial topology is a prerequisite for novel design of low-consumption devices with complex fabrication, whose paradigm would change from "one material - one functionality" to "all-in-one".

In third instance, I approached two van der Waals crystals - materials structured in atomically thin layers with low interplanar interactions - exhibiting the much sought-after ferromagnetic ordering in 2D. The defiance of the Mermin-Wagner theorem for strongly anisotropic materials has paved the way to new possibilities in device engineering.

The thesis sets off with an introductory section dedicated to a more generic background, which I included to guide the reader should he be unfamiliar with some of the more technical aspects of this work.

In Chapter 1 I describe the framework of the experimental techniques employed herein. This part progressively tackles photoemission spectroscopy and spin polarimetry, absorption spectroscopy and time-resolved photoemission spectroscopy. Theory is taken into consideration within the limits of an explanation of experiments, not to discourage readers with less theoretical inclinations.

In Chapter 2 I present the beamlines where measurements have been carried out, together with additional details on how the work has been divided between in-house research and beamtimes. This section contains more technical details about instrumentation, in order to understand strenghts and limitations of each setup.

In **Part I** (Chapters 3-4) I employ ARPES and spin polarimetry to study a Fe(001) monocrystal with p(1x1)O surface reconstruction, measuring the electronic and spin degrees of freedom of the topmost valence band. In Chapter 3, after a brief introduction on the topic, I present Fe(001)-p(1x1)O/MgO and discuss its band structure and the spin character of the bound electrons of lower binding energies. Data acquired by ARPES suggests a well-ordered sample with clear band dispersion and help in identifying the key electronic features. Threshold photoemission polarimetry suggests that the spin polarisation of the topmost band at the $\bar{\Gamma}$ point is of majority character; I prove that threshold photoemission is a bulk-sensitive technique and I interpret the value of spin polarisation at threshold as the sum of the contributions of inelastic and primary

electrons photoemitted from a specific region in the Brillouin zone. I also characterise multiphoton photoemission and space charge effects from visible and UV laser pulses.

In Chapter 4, I extend the investigation of Fe(001)-p(1x1)O/MgO to the time domain. I introduce the motivations for probing the dynamics of *3d* transition metals and line out the main results in previous experiments. Later, I address the ultrafast relaxation of electronic and spin excitations as a function of several parametres. I find that light polarisation and pump energy result in little effect on the temporal shape of time-resolved data, suggesting that the ultrafast dynamics is not dominated by carriers redistribution. Non-thermal electrons are measured at high incidence angles, where intense band structure features extend above the Fermi level, and I ascertain that their temporal footprint is extremely fast.

The independent measurements of electronic temperature (via Fermi level broadening) and spin temperature (via spin polarisation imbalance) by means of different probe photons are described with phenomenological models, allowing to emphasise the dissimilarities in their characteristic time constants and to exclude electronic occupation as the leading drive for ultrafast demagnetisation. I employ a microscopic three-temperature model to interpret my data and conclude that the phenomenology of ultrafast dynamics of the spin polarisation is completely explainable by Elliott-Yafet type spin-flip scattering. I relate my findings to other results in literature, obtaining good consistency.

In **Part II** (Chapter 5) I move on to the study of a layered system where magnetism and topology coexist and cooperate. A concise overview of topological insulators and the problem of magnetism in topological systems is followed by the characterisation of the antiferromagnetic topological insulator $EuSn_2P_2$ by ARPES and XPS. I unveil a variation of the band structure and of the phosphorus *2p* core level lineshape depending on the surface termination; indeed, additional warped P-derived bands, which are predicted by calculations to show topological character, are revealed in case of a P-terminated surface. XAS measurements disclose a pure Eu^{2+} valence state in stable surfaces; I performed XMCD on Eu $M_{4,5}$ edges and Spin-ARPES on Eu *4f* localised states and verified the presence of in-plane long-range magnetic order at low temperatures, disappearing above the Néel temperature. I confirm the presence of a non-trivial topology by measuring spin-momentum locking on the P-derived bands by Spin-ARPES, below and above the Néel temperature. The coexistence of magnetic order and topological states in $EuSn_2P_2$ suggest that the rise of axion physics in a solid is possible with stoichiometric compounds.

In **Part III** (Chapter 6) I describe experiments on the van der Waals magnetic semiconductors VI_3 and CrI_3. By comparing ARPES data with first-principles DFT calculations, I am able to ascertain the role of the transition metal in determining the electronic occupation and the level splitting of the two compounds; I note a different symmetry between transition metal and iodine electronic states, which I attribute to short-range correlations. ResPES on both crystals allows to identify the orbital character of features in the band structure, and photon energy-dependent measurements assess the quasi-two-dimensional nature of electronic states. Finally, XMCD on the $L_{2,3}$ edges of VI_3 as a function of temperature pinpoints a critical behaviour pertinent of systems with n = 2 universality class. These information portray a picture of weak interlayer interactions in VI_3 dictating a confinement of electrons in the two-dimensional space of a single layer.

The leitmotiv I followed throughout this thesis is the the study of magnetic properties of materials with different dimensionality. The variegated phenomenology that I explore in the three parts is also linked to the different conditions of spatial confinement that electrons are subject to: this approach, albeit not a systematic study on a single sys-

tem as a function of the dimensionality, is extremely relevant in modern physics due to the fundamental questions that arise with this type of inquiry, and also because of the technological repercussions that low-dimensional systems are foretold to trigger.

The thesis is organised without a clear-cut distinction between the exposition and the discussion of experimental results; this is intended, as I opted for a gradual exposition that allows for the understanding of each segment before moving on to the next one - and sometimes it is compulsory to do so, because of some intrinsic interdependencies in comprehension. In general, within the three parts there is no referral to applications and "real-world validation", which instead have been confined to the introduction and the conclusions of the thesis. In any case, the purpose of this work is not directly applicative anyway, but is rather focused on basic research with the prospective (and, hopefully, the aim) of vast practical importance.

CHAPTER 1

Experimental techniques

If you chase two rabbits, you will lose them both.

Native American proverb

Spectroscopy and polarimetry techniques are an essential and incredibly powerful tools in the investigation of electrons in solids and surfaces. For this reason, understanding the details of both the physical processes and the instrumentation behind every specific measurement becomes mandatory before approaching any experimental result, which otherwise effectively comes out of a "black box" and whose interpretation holds thus little meaning.

A brief introduction to technical aspects of the experimental techniques used in this thesis is given in this section. The presentation includes photoemission spectroscopy, photoemission spin polarimetry and absorption spectroscopy, in no order of importance. Lastly, a description of time-resolved experiments and the pump probe method is provided.

1.1 Photoemission Spectroscopy

Probably, the first experimental evidence of the photoelectric effect is the one described by Heinrich Hertz (Hertz, 1887). In 1887, Hertz was performing experiments to directly observe the electromagnetic waves predicted by Maxwell: his apparatus, consisting of a transmitter and a spark-gap antenna, was able to produce and detect electromagnetic radiation. When placing the receiver antenna in a darkened box behind a glass panel to better observe the spark, he noticed that the spark length was reduced: the UV-absorbing glass was preventing part of the light from reaching the antenna and exciting electrons.

As with many physical phenomena, theory initially struggled to find an explanation for Hertz's discovery. Other experiments further expanded the knowledge on this topic until an accurate theoretical description of the photoelectric effect was famously provided by Albert Einstein (Einstein, 1905), who went on to win the 1921 Nobel Prize in Physics "for his services to Theoretical Physics, and especially for his discovery of the law of the photoelectric effect".[1]

Within the framework of the *quantum theory* (which later became known as *quantum mechanics*), Einstein theorised that the energy of a quantum of light was expressed by $h\nu$, the frequency of the electromagnetic wave multiplied by the Planck constant. If the energy is above a certain threshold, it may be absorbed by a bound electron which is then extracted from the solid to vacuum. The ejected electron is called *photoelectron* and

[1] https://www.nobelprize.org/prizes/physics/1921/summary/.

is said to be *photoemitted* (or *photoexcited*) from the material; its kinetic energy is related to the energy of the quantum of light (the *photon*) and the binding energy of the electron itself:

$$E_K = h\nu - |E_B| - \Phi_s. \tag{1.1}$$

E_B is the binding energy of the electron and Φ is the *work function* of the sample, the potential barrier at the surface (in the order of $\sim 5\,eV$) the electron has to overcome in order to escape into a free state.

A cartoon representation of the photoelectric effect in a solid is shown in fig. 1.1.

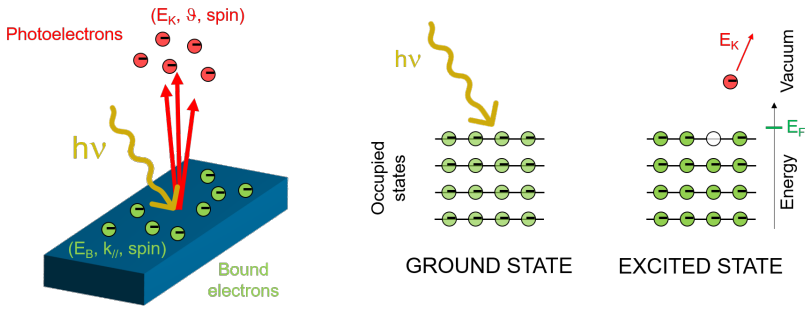

Figure 1.1: Schematic representation of the photoemission process. The sample is left in an excited state due to the ionisation. The most relevant quantum numbers for bound electrons and photoelectrons are highlighted in the parentheses.

The full characterisation of the photoelectron final state is achieved by measuring the set of quantum numbers indicated in fig. 1.1: kinetic energy E_K, angle of emission θ and spin. The ensemble of "photon-in electron-out" techniques exploiting the photoelectric effect is generally called *photoemission spectroscopy* in case of energy measurements, or *spin polarimetry* in case of spin measurements. The two may overlap if a measurement resolves more than one of these quantities, as discussed later.

1.1.1 Classes of photoemission

There is a huge variety of instrumentation able to detect and measure the photoexcited electrons. In general, photoelectrons within a certain solid angle aperture are collected within a series of electrostatic lenses. The analysis performed on photoelectrons depends on the specific type of measurement that is being carried out.

- **Quantum Yield (QY)**: data are acquired by an electron multiplier collecting the ejected electrons or by measuring the neutralisation drain current. In this case there is no energy analysis, but the photon dependence of the QY explores the matrix elements of the material.
- **Photoemission Spectroscopy (PES)**: data can be acquired by scanning the kinetic energy of the electron final state; in case of an X-ray light source, the technique is named **X-ray Photoemission Spectroscopy (XPS)**.
- **Angle-Resolved Photoemission Spectroscopy (ARPES)**: the analyser measures both energy and emission angle of the photoelectron, resulting in energy- and momentum-resolved spectra.

- **Spin-polarised Angle-Resolved Photoemission Spectroscopy (Spin-ARPES)**: ARPES measurements are complemented by spin resolution of the initial state, thanks to the $\Delta S = 0$ dipole selection rule.
- **Spin polarimetry of QY**: spin-resolved measurements are performed on the QY from the sample, without energy or angular resolution.

1.1.2 Photoemission spectroscopy measurements

In PES, an electron hemispherical analyser collecting photoelectrons continuously changes the electric field in order to select a specific kinetic energy at a time: this way, an *energy-dispersive curve* (EDC) is collected.

The energy distribution of the photoelectrons is related to the electronic density of states of the material; the maximum kinetic energy is $E_k^{max} = h\nu - \Phi_s$. In the low-energy region, a broad feature is caused by secondary electrons down to the minimum kinetic energy $E_K^{min} = 0\,eV$. The detector has itself a work function Φ_a; since sample and detector are both grounded, their Fermi level is aligned and a contact potential $\Phi_s - \Phi_a$ between sample and analyser arises, with $\Phi_s > \Phi_a$. When photoelectrons impinge on the detector inside on the analyser, they are effectively accelerated by the difference in work function and their kinetic energy changes following the relation below:

$$E_K = h\nu - E_B - \Phi_s + (\Phi_s - \Phi_a) = h\nu - E_B - \Phi_a. \tag{1.2}$$

The EDC as measured by the analyser thus carries no information on the work function of the sample.

In this case, the new minimum kinetic energy is $E_K^{min} = \Phi_s - \Phi_a$. However, the analyser cannot reliably measure below a certain kinetic energy unless specific electronics are implemented. If an accelerating potential V_0 is applied to the sample, the minimum kinetic energy becomes $E_K^{min} = \Phi_s - \Phi_a + V_0$; the work function of the sample can thus be measured as $\Phi_s = E_K^{min} + \Phi_a - V_0$.

ARPES and Spin-ARPES are effectively performed in the same way: in both cases the electron analyser acquires EDCs, with the difference that in ARPES an EDC is measured for each angle within the analyser angular opening, and in Spin-ARPES two EDCs - one for each spin channel - are separately scanned.

1.1.3 Three-step model

A rigorous description of photoemission would consider the excitation, the transport to the surface and the escape into the vacuum of the photoelectron as a whole, by means of a single quantum-mechanically coherent process (Hopkinson, Pendry and Titterington, 1980; Minár et al., 2011; Pendry, 1976). For our purposes, it is useful to describe a simpler model, the *three-step model*, in order to catch a glimpse of some important concerns in photoemission experiments.

The three-step model, introduced by (Berglund and Spicer, 1964) is a phenomenological approach to photoemission employing the intuitive schematic picture of three independent processes.

- A bound electron in an initial Bloch state of the solid, identified by binding energy E_B, initial momentum $\boldsymbol{k_i}$ and spin S, absorbs a photon with energy $h\nu$. For suitable photon energies, the electron is excited into a Bloch final state: the energy and spin are conserved, and (if the photon momentum is negligible[2]) $\boldsymbol{k}$ is conserved modulo the reciprocal lattice vector $\mathbf{G}$.

- Afterwards, the excited electron travels towards the surface. Depending on its energy, it may undergo one or several inelastic scattering events; if so, the information on its initial state is lost and its contribution is added to the background.
- If the kinetic energy is high enough, the photoelectron overcomes the surface potential barrier Φ and escapes the solid into a vacuum state with kinetic energy , final momentum $\boldsymbol{k_f}$ and spin S.

The aim of the first step is to quantify the probability of excitation from the initial to the final state. This is done by means of the Fermi golden rule (Alford, Feldman and Mayer, 2007): in presence of an electromagnetic perturbation $\mathbf{A}$, the transition rate of an electron from an initial Bloch state $\langle\psi_i|$ to a final Bloch state $|\psi_f\rangle$ is given by

$$W_{if} = \frac{2\pi}{\hbar}\frac{e}{m_e c}|\langle\psi_f|\,\mathbf{A}\cdot\mathbf{p}\,|\psi_i\rangle|^2\delta(E_f - E_i + h\nu). \tag{1.3}$$

This single-particle approach does not take into account electron-electron correlations, which would require a many-body approach, and is one of the intrinsic limitations of the three-step model.

The Dirac delta expresses the energy conservation; the final wavevector $\mathbf{k}_f$ determining the propagation direction in the solid is given by the conservation law

$$\mathbf{k}_f = \mathbf{k}_i + \mathbf{G}. \tag{1.4}$$

The second step describes the probability of suffering inelastic scattering while travelling to the surface. The travel of the photoelectron within the material is a key point in determining the amount of electrons that reach the surface without losing energy: we refer to these as *primary electrons*. Their probability of inelastic scattering depends on the inelastic mean free path λ_{IMFP}, which quantifies how far a primary electron propagates.

The estimation of λ_{IMFP} is thus the main hint towards the depth sensitivity of a photoemission experiment. The inelastic mean free path is an energy- and momentum-dependent quantity; for normal emission, the wavevector dependence can be ignored and a "universal" curve can be plotted, as in fig. 1.2.

The "universal" curve is a good first-order approximation, to give a rough estimation of λ_{IMFP}; however, it is often inaccurate: it strongly depends whether the material is insulating, semiconducting or metallic, and especially in the low-energy range often depends on the material itself (Colón Santana, 2015). Overall, one must surrender to the fact that determining λ_{IMFP} in a general, unambiguous way is extremely complex.

The third step illustrates the probability of transmitting the electron into a free vacuum state. At this point, conservation laws have to be reexamined.

As already mentioned, the kinetic energy E_k of the photoelectron in the vacuum can be univocally related to the binding energy of the initial state E_B by means of eq. (1.1), with the addition of the work function given by the surface potential.

Conversely, retrieving the initial electron momentum $\mathbf{k}_i$ is not as straightforward. The conservation law in eq. (1.4) holds within the solid, but as soon as the lattice symmetry is broken at the surface only the parallel component $k_{||}$ of the wavevector is conserved; the perpendicular component $k_\perp$ instead is not conserved.

$k_{||,i}$ can be thus retrieved as follows:

[2] In all photoemission experiments considered in the present work, the photon momentum can be neglected. Photon energies above 120 eV would explicitly require an additional term accounting for the photon contribution (Damascelli, Hussain and Z.-X. Shen, 2003).

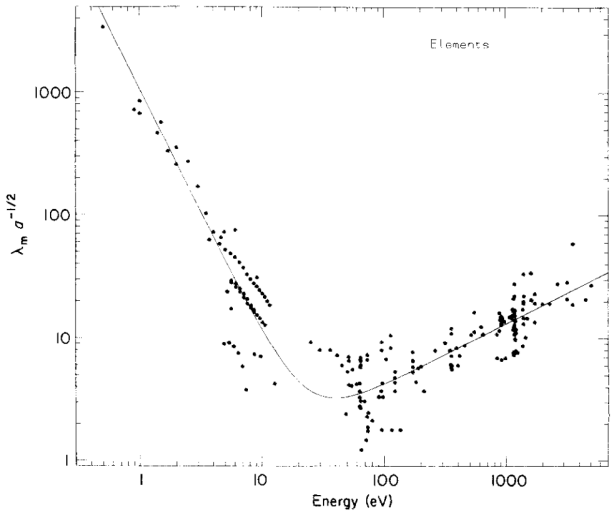

Figure 1.2: Inelastic mean free path of electrons as a function of electron energy, compiled for elements. Adapted from (Seah and Dench, 1979).

$$k_{\parallel,i} = k_{\parallel,f} = \frac{\sqrt{2m_e E_K}}{\hbar} \sin\theta, \tag{1.5}$$

where θ is the emission angle of the photoelectron in vacuum with kinetic energy E_K, measured from the surface normal. To relate $k_{\perp,i}$ to measurable quantities, one has to assume that the ejected electron is refracted at the surface following the law

$$k_{\perp,i} = \frac{\sqrt{2m_e E_K \cos\theta^2 + V_0}}{\hbar}, \tag{1.6}$$

where V_0 is the *inner potential*, a material-dependent parameter governing the $k_\perp$ refraction, usually in the range from 10 eV to 18 eV.

1.1.4 One-step model

The three-step model is an intuitive and useful tool to understand the photoemission process, but is ridden with approximations: prominently, the failure in accounting for the remaining N-1 electrons system after the excitation, and the description of initial and final states as Bloch wavefunctions with infinite lifetime.

Indeed, the framework of the more rigorous *one-step model* account also for all possible deexcitation channels in the ionised solid after excitation. A key point in this description is the *sudden approximation*: the electron emission takes place on a timescale much shorter than the relaxation time of the ionised material. If this condition is fulfilled, the system is divided into two subsets, the single photoexcited electron and the N-1 bound electrons, and the problem is treated by means of a Green function formalism. The electron is no more considered as a free particle, since a quasiparticle description is required: the Green function describes the behaviour of a quasiparticle, which is "dressed" by all possible correlations (including with itself). Their influence on the whole system is expressed by introducing the *self-energy* Σ: the self-energy appears in the expression of the *spectral function* A(**k**,E), constituting the probability of adding or

removing an electron from the ground state of a many-body system. The two are represented in eq. (1.7): the real part of Σ renormalises the energy with respect to a non-interacting system, characterised by an energy E_0, while the imaginary part of Σ evaluates the quasiparticle lifetime.

$$\Sigma = \Re(\Sigma) + \Im(\Sigma) \tag{1.7}$$

$$A(\mathbf{k}, E) = \frac{1}{\pi} \frac{\Im(\Sigma)}{(E - E_0 - \Re(\Sigma))^2 + |\Im(\Sigma)|^2} \tag{1.8}$$

The spectral function replaces the Dirac delta in eq. (1.3); the total photocurrent will be then represented by a sum over the dipole-allowed transitions between the initial and final states $\langle\psi_i|$ and $|\psi_f\rangle$, weighted by the spectral density and the density of states of the solid.

The factor $\langle\psi_f| \mathbf{A} \cdot \mathbf{p} |\psi_i\rangle$ appearing in the expression contains the dependence on extrinsic factors: photon energy, light polarisation, experimental geometry. The modulation of the photoemitted intensity on the basis of the value of the braket above is called *matrix element effect*.

Ab initio calculations may compute A(**k**,E), but the quantitative determination of matrix elements is a much more challenging task. However, some symmetry rules based on light polarisation and electronic orbitals allow to discern some matrix elements relatively easily.

As a matter of fact, the electron final state must have even spatial distribution to be detected; the final state $\langle\psi_f|$ is always even, therefore $\mathbf{A} \cdot \mathbf{p} |\psi_i\rangle$ must be even too. If linearly polarised light is employed, the symmetry of the probed electronic orbitals can be directly measured.

As an example, we can consider the d_{xy} orbital in fig. 1.3. With respect to the two orthogonal mirror planes yz and xz, the orbital has always odd reflection symmetry. The symmetry of the incident light depends on the polarisation vector: linear horizontal (LH) light is even (odd) upon reflection about the yz (xz) plane; the reverse is true for linear vertical (LV) light.

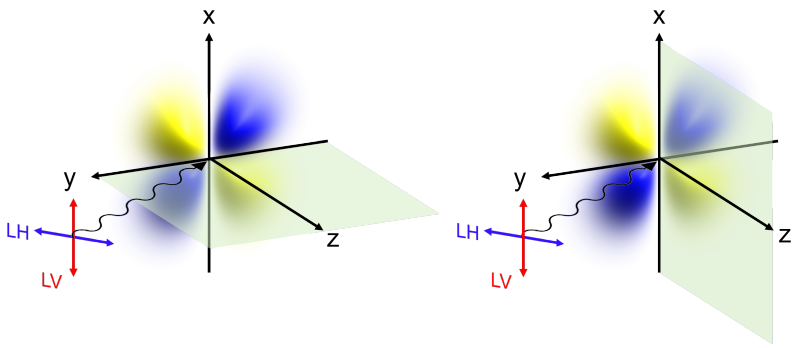

Figure 1.3: Cartoon representation for symmetry selection rules of a d_{xy} orbital, for linearly polarised light.

This means that LH light results in a matrix element equal to zero for the yz plane (even **A**, odd $|\psi_i\rangle$, so the scalar product is zero) and no photoemitted intensity is detec-

ted; on the other hand, on the xz plane LH light has even and odd components, so a non-zero intensity can be measured.

1.1.5 Resonant Photoemission Spectroscopy

In photoemission spectroscopy measurements, at very specific photon energies there may be a secondary process overlapping to the direct photoemission process sketched in fig. 1.1. If the photon energy is tuned at an absorption edge of one of the elements constituing the material under exam, core level excitations may take place, where core electrons jump to the conduction band. Since a core hole together with a conduction electron is a highly perturbed system, the excited electron has a high probability of filling the hole and either emitting a photon or transferring the excess energy to a valence electron, which is in turn photoemitted in an Auger process. The process is sketched in fig. 1.4.

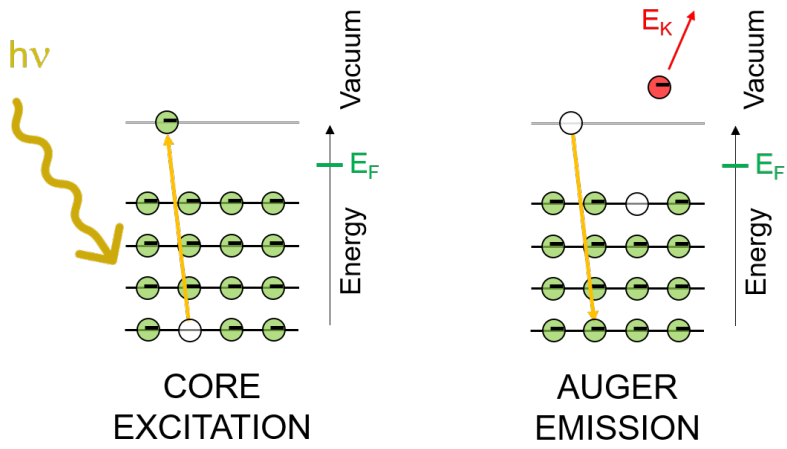

Figure 1.4: Cartoon representation of the two steps characterising resonant photoemission spectroscopy: the absorption of a photon by a core electron (*left*) and the relaxation with emission of an Auger photoelectron (*right*).

Even if this picture is somewhat simplified with respect to the one-step model discussed above, it is clear that in the case of Auger photoemission $\langle\psi_i|$ and $|\psi_f\rangle$ are the same as conventional photoemission in fig. 1.1. For this reason, the two processes interfere and result in a strong enhancement of the photoemission yield from the valence state in question. Moreover, the dipole selection rules allow this enhancement only for those band structure regions originating from orbitals belonging to the element involved in the absorption.

This process is called Resonant Photoemission Spectroscopy (ResPES) (Hippert et al., 2006): the technique is able to probe a specific chemical species via the choice of the absorption edge, as well as assessing the orbital character of the bands.

1.1.6 Spin polarimetry and Spin-ARPES measurements

As discussed above, the photoemitted electrons can be analysed according to their energy and their momentum. In addition, they can also be analysed according to their spin

polarisation. Of an electron ensemble, as represented by the photoelectron beam, one can measure its spin polarisation vector, defined as the expectation value of the Pauli matrices over the state representing the electron ensemble:

$$P_{x,y,z} = < \sigma_{x,y,z} >_{\text{ensemble}} . \tag{1.9}$$

For instance,

$$P_z = \frac{N\uparrow - N_\downarrow}{N\uparrow + N_\downarrow}, \tag{1.10}$$

$N\uparrow$ and $N\downarrow$ being respectively the number of electrons with spin oriented parallel or antiparallel to the z axis. The measurement of the spin polarisation vector requires a special detector that is sensitive to the spin of the photoemitted electrons. Within this thesis, we will use two types of detectors, both based on scattering the photoemitted beam at a suitable target. One uses energies in the 10 – –100 keV order of magnitude (Mott scattering). The second uses the so called exchange scattering, occurring, with high spin sensitivity, at low energies (few tens of electronvolts).

Mott scattering

In Mott scattering, the electron beam to be spin-analysed is directed towards a target and the number of electrons appearing at some scattering angle $\pm\theta$ within a given scattering plane (parallel to **n**) is recorded (Gay and Dunning, 1992), as shown in fig. 1.5.

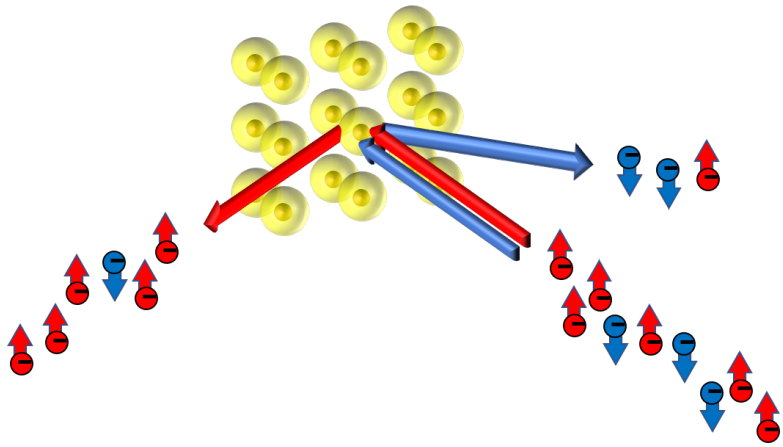

Figure 1.5: Cartoon representation of the Mott spin-selective process: yellow spheres stand for Au target atoms, red and blue circles represent electrons with spin up or down, coloured arrows indicate the scattering directions of the corresponding spins.

In virtue of the spin-orbit coupling interaction between the incoming electrons and the target atoms, an asymmetry A_{Mott} of the count rate I at the angles $\pm\theta$ is produced. The asymmetry is proportional to the component of the spin polarisation vector perpendicular to the scattering plane:

$$A_{\text{Mott}} = \frac{I_{+\theta} - I_{-\theta}}{I_{+\theta} + I_{-\theta}} = S_{\text{Mott}}(E,\theta)\mathbf{P}\cdot\mathbf{n} \tag{1.11}$$

The proportionality constant $S_{Mott}(E, \theta)$ is the so-called Sherman function and depends on the scattering energy and scattering angle, and on the target material. The many important aspects relating to $S_{Mott}(E, \theta)$ are discussed *e.g.* in (Pincelli, Grasselli et al., 2017).

Compact Mott detectors

The Mott spin polarimeter used in this thesis belongs to the class of instruments called *compact Mott detectors*, operating at lower primary electron energy compared to "standard-issue" Mott detectors (40 keV vs 100 keV). We use a 80 nm-thick polycrystalline Au foil as target. Au targets maximise the Sherman function, minimise contamination issues and simplify maintenance. By employing four detectors mounted in an orthogonal configuration, we are able to detect two components of the spin polarization vector simoultaneously.

Instead of channeltron or MCP electron counters, Passivated Implanted Planar Silicon (PIPS) detectors are implemented. These are p-n junctions with a strong reversed potential and therefore a large depletion region: the incoming electrons lose all their energy by electron-hole pairs creation, since the depletion region is larger than the stopping length of the particles in the material. Electrons and holes are then separated by the field and a preamplifier is able to convert the charge pulse into an analogic voltage signal.

This system is optimised for multi-hit detection. As a matter of fact, the temporal length of a laser pulse ($\sim$ 200 fs) is short compared to the drift and collection of electrons and holes at the two extremities of the junction: if more than one photoelectron is emitted by the laser pulse and impinges on a detector, the electronics is programmed to integrate the deposited charge over a set time window and thus discern the number of electrons from the voltage signal, avoiding saturation problem.

Exchange scattering

In order to operate at low energies, a spin detector is based on exchange scattering with a target consisting of ferromagnetic material. In this situation, the scattering asymmetry is due to the exchange interaction between the spin of the incoming electrons and the magnetic moment **m** of the target atoms.

The simplest way of employing exchange scattering for spin detection is measuring the (00) beam, *i.e.* the beam specularly reflected after the photoemitted beam, adjusted to have an energy in the range from 5 eV to 15 eV, has impinged on the magnetic target; this requires the implementation of an off-normal geometry with respect to the target. The reflected beam is then collected by a channeltron. Two quantities are measured: one is the intensity of the reflected beam for **m** along a given direction (I_{+m}). The second is the intensity of the reflected beam for reversed **m** (I_{-m}). The recorded quantity along a direction **n** is then

$$A_{exchange} = \frac{I_{+m} - I_{-m}}{I_{+m} + I_{-m}} = S_{exchange}(E, \theta, \mathbf{m})\mathbf{P} \cdot \mathbf{n}. \tag{1.12}$$

A geometry where **n** is parallel to **m** maximizes $S_{exchange}(E, \theta, \vec{m})$.

A drawback of the exchange scattering spin detector is the requirement of a magnetised target, which has to be kept clean and free from contaminants. However, (R. Bertacco et al., 2002) realised that a Fe(100) target covered with a passivating monolayer

of oxygen reconstructed in a p(1x1) fashion is much less vulnerable to contaminations and shows no reduction (rather an enhancement) of $S_{exchange}(E, \theta, \mathbf{m})$.

Notice that, typically, the figure of merit[3] is much larger in exchange scattering that in Mott scattering. However, the energy of the impinging electrons in low-energy spin detectors must be well-defined to a higher degree, as the exchange asymmetry averages to zero over some energy range. Low-energy spin detectors find therefore their natural use in energy-resolved experiments.

1.2 X-ray Absorption Spectroscopy

As we saw previously, bound electrons after the absorption of a photon may be photo-excited into the vacuum; photoemission focuses on the photoelectrons emitted from a material to study its electronic properties.

However, the absorption of a photon by core electrons is a physical phenomenon that can be studied by itself, and indeed the scientific development in the late 19^{th} century showed that the study of the photoelectric effect and X-ray absorption proceded in parallel. The first evidence of X-ray absorption comes from the discoverer of X-rays himself, Wilhelm Röntgen, who in 1895 famously took the first radiograph of a human body part, the hand of his wife, Bertha Maria. Since then, the exploitation of X-rays to excite core electrons of elements to extract information on the constituents of the material under exam has grown out of proportion.

If the absorption process itself is made the focal point of a measurement, instead of the study of the photoelectrons emitted *after* they absorb a photon - and in particular when using X-rays - then we deal with the experimental technique of X-ray Absorption Spectroscopy (XAS).

1.2.1 The absorption process

As we already know, the transition rate upon photon absorption in the dipole approximation is given by eq. (1.3). In this case, we are not interested in a free final state as in photoemission, but rather in the promotion of the core electron to an empty state in the conduction band. Dipole selection rules govern these transitions, so only some of all possible excitations actually take place. The highly unstable core hole is then quickly refilled by the decay of the excited electron; at this stage, the excess energy can either be emitted as fluorescence, or transferred to an electron in the valence band, which is photoemitted as an Auger electron. The whole process is summed up in fig. 1.6.

Differently from photoemission, XAS measurements do not collect and analyse photoemitted electrons. In other fields of application of X-rays, the simplest solution is to measure the X-ray intensity before and after the sample; in solid state science, though, this is not easy (especially in the soft X-rays range) because it would require an extremely thin sample (in the order of micrometres). For this reason, the decay channels are used for detection.

As we mentioned before, one decay channel after the filling of the core hole is the emission of photons, which can be collected in a photodiode: this is the *fluorescence yield* (FY) operation mode. The absorption length of photons is generally around $\sim$100 nm,

[3] The figure of merit for spin detection is defined as

$$\frac{I_{\text{scattered or reflected}}}{I_{\text{incoming}}} \cdot S^2_{\text{Mott or exchange}}.$$

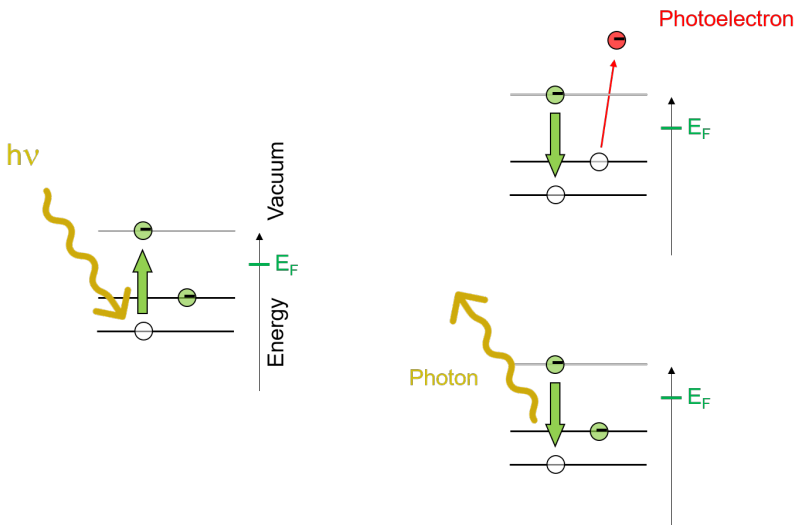

Figure 1.6: Cartoon representation in the independent particle approximation of the XAS process (*left*) and the decay channels via Auger emission (*top right*) or fluorescence (*bottom right*).

therefore a FY measurement can be considered bulk sensitive; in any case, photons can be reabsorbed, scattered or refracted at surfaces or interfaces, and this is a relevant source of distortion of XAS spectra.

The other decay channel is Auger photoelectron emission: the charge depletion at the surface resulting from photoemission has to be compensated by a corresponding charge from from the ground, and measuring this current with a picoamperometre is the basis of the total electron yield (TEY) operation mode. While photons travel unscathed through hundreds of nanometres of matter, electrons interact much more strongly: for this reason, only electrons close to the surface can escape the solid and contribute to the TEY signal. TEY measurements are thus much more "surface"-sensitive than FY measurements, even if in surface science applications a probing depth from 5 nm to 10 nm (typical values for TEY) can be considered rather bulk-sensitive as well.

There is no best way to measure absorption spectra: the choice between FY and TEY depends on the purposes of the experiment. One point that has to be carefully considered is the relative cross section of the two decay processes: measuring K edges in the hard X-ray range in FY is generally more convenient, whereas across L edges in the soft X-ray range the Auger decay is dominant and TEY measurements are more efficient.

1.2.2 Theoretical description

In the simplistic non-interacting picture decribed in the previous section, the absorption intensity is given by the convolution between the core hole level lines and the empty density of states. In reality, the overlap between the core hole wavefunction and the valence states strongly affects the final state, especially for L edges like those presented in this work.

To treat more realistically the transitions, usually two steps can be employed. First, an atomistic picture starts from the Schrödinger equation to solve the electronic problem: the electronic states are described by means of term symbols in the form $^{2S+1}L_J$, where

the spin S, the orbital L and total J angular momentum are good quantum numbers[4]. The electron-electron interaction is described by direct and exchange integrals, the *Slater-Condon* parameters, and the energy levels are given by a combination of these parameters. The second step is considering that neighbouring atoms play a role in determining the energy of the system: the interaction between them is given by the *crystal field* parameters. The Slater-Condon and the crystal field parameters are a measure of the relative strength of the two effects they represent.

Electronic hybridisation between ligands is the source of another effect, the *charge transfer*. A partial charge transfer between two atoms modifies the ground state and the interactions; a localised charge transfer occurring after the creation of the core hole influences also the final state. This is usually modelled by adding additional parameters such as the *hybridisation strength* and the *charge transfer energy*.

All in all, we saw that a relatively straightforward description (the absorption of a photon by a core electron, the excitation in the conduction band, the core hole filling and the emission of either UV light or an Auger electron) helps in intuitively understanding the process, but in order to accurately treat it several parameters have to be considered.

1.2.3 X-ray magnetic circular dichroism

XAS is a powerful technique not only because it probes orbitals in an element-specific fashion, but also for the possibility of exploiting dichroic effects, i.e. modulations in the absorption due to changes in the light polarisation, to assess magnetic properties in materials: this effect is called X-ray Magnetic Circular Dichroism (XMCD).

The same reasoning we followed for photoemission can be applied for absorption: the transition rate of eq. (1.3) contains matrix elements determined also by the X-ray polarisation. The relation to magnetism can be understood even in an independent particle framework (Joachim Stöhr and Siegmann, 2006), for example in the case of transition from *2p* to *3d* orbitals ($L_{2,3}$ edges), in case of reversal of the photon helicity from left- to right-circular polarisation.

We assume the case of a strong ferromagnet, with the $\downarrow$ spin channel completely filled and the $\uparrow$ spin channel partially filled. Dipole transition selection rules require $\Delta m_l = \pm 1$, $\Delta m_s = 0$. Excitations take place from spin-orbit and exchange-split p core states $|j, m_j\rangle$ to $\uparrow$ spin d valence orbitals $|m_s = +1/2\rangle$; this is the origin of the dichroic effect. For negative ($q = -1$) and positive ($q = +1$) photon angular momentum,[5] one can calculate the matrix elements by writing d states as linear combinations of basis functions $|l = 2, m_l, s, m_s\rangle$: the result is that at the L_3 edge X-rays with $q = +1$ excite more $\uparrow$ electrons compared to $q = -1$, while at the L_2 edge the opposite is found. A graphical representation is shown below in fig. 1.7.

It is worth mentioning that the quantisation axis is determined by the direction of the **q** vector: only a parallel or antiparallel alignment of the magnetic moment can be detected. If the magnetisation is perpendicular, no intensity difference is recorded. This also implies that reversing the photon helicity is equivalent to reversing the magnetisation of the sample; in experiments, the former is generally more time-consuming, whereas the latter is the go-to choice.

XMCD spectra can be often quantitatively connected to physical quantities by means of the so-called *sum rules*: an analysis on XMCD may be able to retrieve the number of

[4] We have to specify that often the core hole spin-orbit coupling is not a small perturbation term, so the eigenstates of the system are not simply the terms $^{2S+1}L_J$.

[5] In units of $\hbar$.

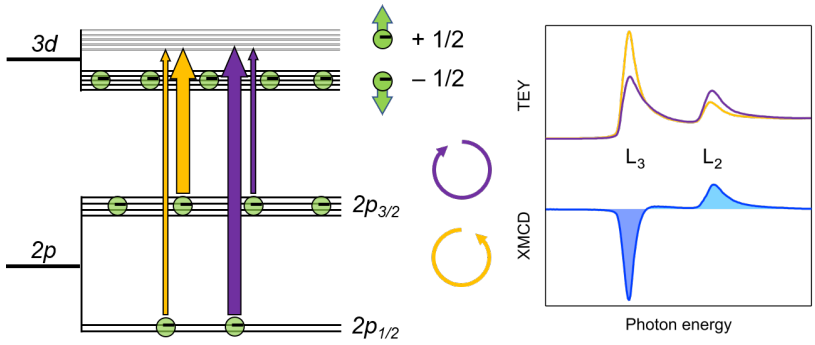

Figure 1.7: Cartoon representation in the independent particle approximation of the XMCD process (*left*) and example of two XAS spectra with opposite light polarisation and resulting XMCD (*right*).

holes in the valence state n_h, the average orbital angular momentum L_z and the effective spin angular momentum S_z^{eff}.

1. The integral of the isotropic XAS spectrum, *i.e.* the average between spectra with opposite helicity, is proportional to n_h.
2. The integral of the XMCD signal is related to L_z.
3. The combination of the integrals of L_2 and L_3 edges is related to S_z^{eff}.

XMCD thus combines the element sensitivity of XAS with a direct measurement of the average magnetic moment on specific atoms, making it a powerful tool for magnetic analysis of complex materials.

1.3 Time resolution

The determination of the ground state within a set of boundary conditions is governed by the order parameters characterising the distinct ensembles in a solid. The coexistence and competition between these many degrees of freedom gives a set of elementary excitations defined by precise energy scales, which in turn thanks to the energy-time uncertainty may be read in terms of timescales.

The relaxation of a system towards a minimum of the free energy thus takes place in a timescale depending on the interaction driving the excitation. Irrespectively of the details and the proximity in energy of competing phenomena, accessing the timescale of the deexcitation allows to disentangle the contributions to the establishment of an equilibrium.

Figure 1.8 exemplifies interacting degrees of freedom and excitations with their characteristic time and energy scale. It is clear that appropriate instrumentation and light sources are required to probe extremely short time durations. Continuous light sources are not suited for sampling the temporal evolution of a physical system, and pulsed light becomes a necessity; since a relaxation process lasting less than the duration of the pulse cannot be resolved, the resolution of a time-resolved measurement is therefore limited by the time length of the pulse.

The true technological breakthrough in the generation of ultrashort photon pulses from lasers came with the technique of chirped pulse amplification (CPA), developed in

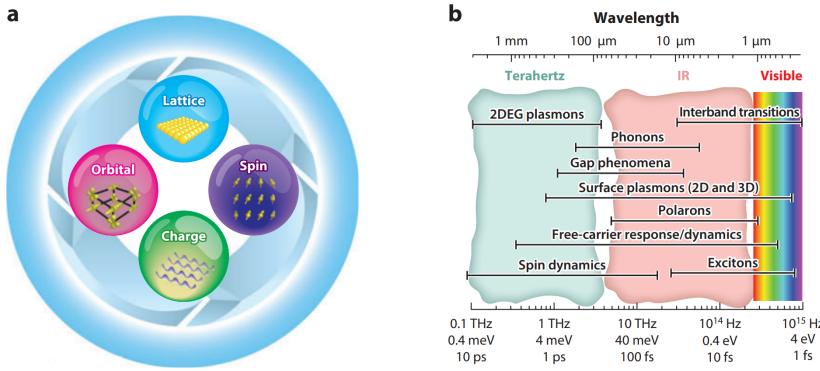

Figure 1.8: Cartoon representation of (a) the thermal reservoirs interacting upon excitation and (b) the characteristic energy and timescales of fundamental excitations in solids. Adapted from (J. Zhang and Averitt, 2014).

the 1980s by Donna Strickland and Gérard Mourou (who were awarded the Nobel Prize in 2018[6]): the following development of regenerative amplifiers based on this principle pushed the boundaries of tabletop laser light sources well into the unprecedented timescale of below-picosecond pulse duration.

This allows to address many of the fundamental excitations in fig. 1.8b, via the study of the rate of excitation transfer among different (model) energy reservoirs describing the energetics of solid matter. The burgeoning field of time-resolved experiments makes use of a host of different experimental techniques, among which we will focus on the one employed in this thesis: the *pump-probe*.

1.3.1 The pump-probe method

What follows hereinafter is a general overview of the application of the pump-probe method to time-resolved photoemission spectroscopy (TR-PES). This section does not aspire to review the field with in-depth explanations of the more theoretical and technical aspects of the technique, but will rather focus on the general concepts of TR-PES applied to the study of solids by means of tabletop laser sources. One should also consider that he use of other equipment such as free-electron lasers (FEL) as high brilliance pulsed light sources (Allaria et al., 2013; L.-P. Oloff et al., 2016; Tono et al., 2013) allows the realisation of a number of different strategies, but we will not expand the topic beyond the boundaries defined above; the interested reader is referred to the works of (Spesyvtsev, Underwood and Fielding, 2014; Stolow, Bragg and Neumark, 2004; T. Suzuki, 2012).

In the context of TR-PES, experiments are carried out following the pump-probe method. This is a stroboscopic technique making use of two separate laser pulses, one delayed in time with respect to the other: the *pump* stirs the material out of equilibrium with an intense pulse, typically exciting low-energy quasiparticles (*e.g.* phonons), and the *probe* photoexcites electrons to free electron-like final states in order to retrieve spectroscopic information.

[6] "for groundbreaking inventions in the field of laser physics", and in particular "for their method of generating high-intensity, ultra-short optical pulses"; https://www.nobelprize.org/prizes/physics/2018/press-release/.

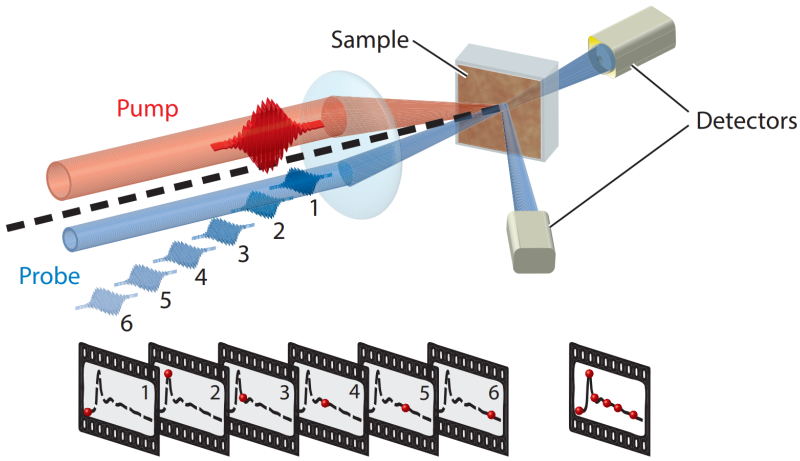

Figure 1.9: Cartoon representation of the pump probe process. Adapted from (J. Zhang and Averitt, 2014).

The energy and power density of the pump is a crucial parameter: since the purpose is driving the system far out of equilibrium, often the pump energy is in the infrared range, in order to create low-energy excitations, and depending on the experiment it may be required to induce a specific pumped state with longer pulses or to drive a far-from-equilibrium state with shorter, more intense pulses.

Conversely, the probe pulse does not require extreme peak power densities - actually they should be avoided - and is required to follow the relaxation dynamics in the spectroscopy limit, *i.e.* interpretable within perturbation theory. This means that the time delay between pump and probe pulses should be measurable and variable during data acquisition: generally this is implemented by mobile optical elements changing the length of the optical path of one of the two beams. A displacement of 10 μm is well within the capabilities of state-of-the-art equipment: this corresponds to $\sim$ 30 fs, and can easily be extended to lower time ranges, allowing the study of ultrafast phenomena in the femtosecond timescale.

A typical pump-probe measurement thus employs two separate optical paths for pump and probe beams; for each pump-probe pulse pair at a fixed time delay an acquisition is performed, and the process is repeated until the desired time delay range is covered, as illustrated in fig. 1.9. At negative time delays, the probe impinges on the sample before the pump: the resulting signal bears no effect of the excitation and can be considered as representative of an unperturbed state. When the time delay approaches zero, the overlap between pump and probe triggers the appearance of a signal given by the convolution of the two pulses. The time delay when pump and probe pulses are overlapped is called t_0 (*time zero*). At positive time delays, the gradual relaxation of the system is mapped by the increased delay of the probe with respect to the pump.

Extreme care should be exerted upon the fact that the pump-probe method requires a *full recovery* of the initial state in-between two acquisitions: then, and only then, the excited state can be prepared in the exact same conditions by the pump pulse. The ground state recovery depends on the sample and the parametres of the pump, but generally spans the ranges of picoseconds or nanoseconds. The time interval between two subsequent pump pulses is given by the repetition rate of the light source, which may reach

up to hundreds of kilohertz: two pulses are thus quite far apart in time, so generally the system relaxes to equilibrium without any problem. Beam damage and chemical modifications upon pumping are other common concerns, especially with vulnerable samples (*e.g.* organic molecules).

1.3.2 TR-PES measurements

In pump-probe photoemission spectroscopy, photoelectrons are collected and analysed as a function of time delay. TR-PES experiments are delicate and time-consuming in terms of their fine setup and data statistics. The typical result of a TR-PES measurement is an E vs time delay map, displayed in fig. 1.10a. EDCs at different time delays are aligned to form a 2D map; a cut along the vertical direction represents an EDC at a specific delay (fig. 1.10b), a cut along the horizontal direction is a time delay curve, explicating the behaviour of the photoemitted yield at a specific energy as a function of the time delay (fig. 1.10c).

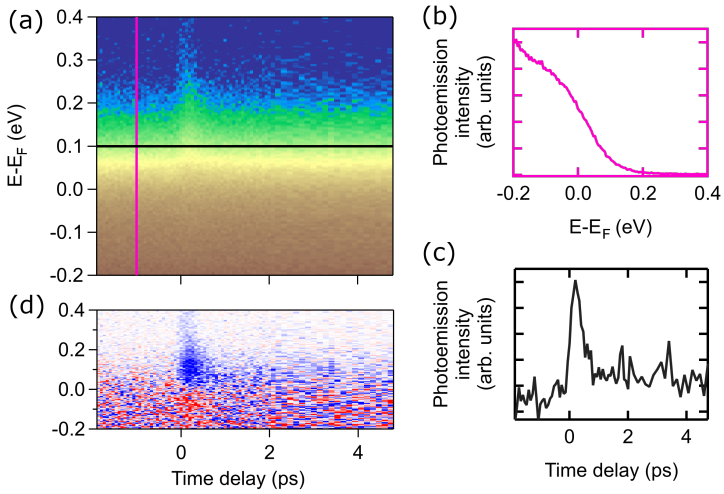

Figure 1.10: (a) E vs time delay map; the pink and black lines highlight the cuts illustrated in (b) and (c), EDCs and time delay curves respectively. (d) Differential E vs time delay map of the same data.

As mentioned before, data acquired before t_0 describe the material in its unperturbed state. If an EDC before t_0 is subtracted from the whole time delay map, the result is a differential time delay map. In this case, zero intensity represents no change from the ground state: the perturbation from the pump pulse is given by a positive signal (increased photoemission yield) or negative signal (decreased photoemission yield). An example in fig. 1.10d shows positive signal in blue, negative signal in red and zero signal in white.

CHAPTER 2

Beamlines and facilities

> How far your eyes may pierce I can not tell:
> Striving to better, oft we mar what's well.
>
> Duke of Albany, *King Lear*

2.1 Methods

Magnetic phenomena in solids, whether more straightforward descriptions like Stoner magnetism or more exotic properties like axion insulating states, are mostly determined by the behaviour of band electrons near the Fermi surface. Setting the goal of giving a quantitative insight into the magnetic degrees of freedom, as well as their relationship with dimensionality, thus requires measuring electronic properties in the near-Fermi region. To do this, spectroscopy techniques performed in state-of-the-art beamlines, where light sources such as third-generation medium and high-energy synchrotron radiation facilities or cutting-edge ultrashort pulsed lasers are employed, and where versatile endstations allow for complex experiments with *e.g.* variable photon energy, light polarisation or depth sensitivity, *in situ* growth and complementary characterisation of atomic order at surface.

The sections below are an introduction to the beamlines highlighting the aspects that are relevant for the experimental part, and as such provide neither a historical perspective of the development of synchrotron radiation facilities, nor the insight into the technological progress. The interested reader is referred to (Mobilio, Boscherini and Meneghini, 2015), where the topic is treated with much greater detail.

2.2 I09 Beamline

I09 (T.-L. Lee and Duncan, 2018) is the first beamline in the world relying on two independent sources and optics that are capable of delivering soft X-rays and hard X-rays to the same spot, to perform photoemission and absorption experiments with different photons in the same experimental conditions. This beamline is located in Diamond Light Source, at the end of one of the four 8 m straight sections in the storage ring. Photons are provided by two undulators in a zigzag configuration that feed three endstations.

The first 2 m undulator with a magnetic period of 27 mm and a minimum gap of 5.2 mm delivers hard X-rays in the range of 2 keV to 18 keV to the I branch. A Si(111) double-crystal monochromator, cryocooled because of the large heat load it has to sustain, achieves an energy resolution of $\Delta E/E \sim 1 \times 10^{-4}$ at 6000 eV, which is not enough for a high-resolution HAXPES beamline; therefore, a channel-cut monochromator can

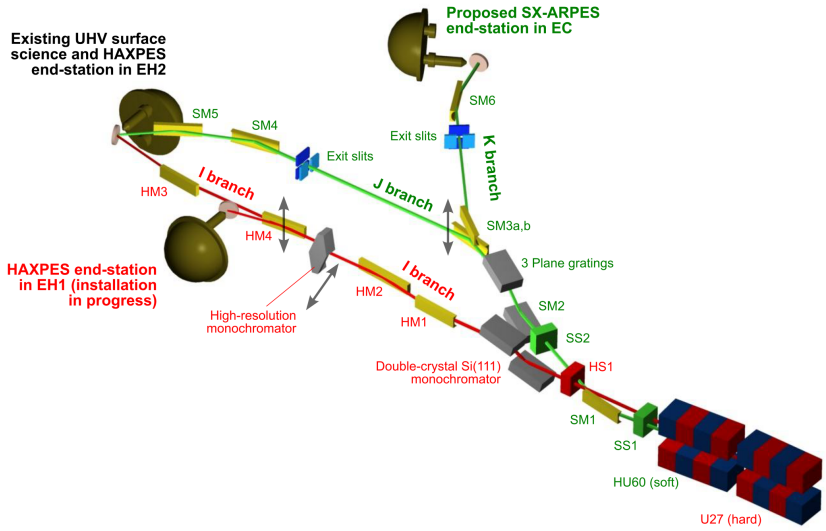

Figure 2.1: Schematics of the I09 beamline. From (T.-L. Lee and Duncan, 2018).

be inserted in the optical path to improve the energy resolution without hindering too much the beam stability and flux. A set of mirrors collimate and focus the beam to a $15 \times 30\,\mu m^2$ spot size in the EH1 hard X-ray endstation.

The second undulator, a modified APPLE-II with a 60 mm magnetic period, is canted 1.3 mrad with respect to the first one and feeds the K branch; the energy range of 200 eV to 2000 eV is covered by a monochromator featuring three gratings ($300\,l\,mm^{-1}$, $400\,l\,mm^{-1}$ and $800\,l\,mm^{-1}$) with a hundred millielectronvolts energy resolution in the whole range. The final spot size in the EC soft X-ray endstation can be focused ($15 \times 30\,\mu m^2$) or defocused ($300 \times 300\,\mu m^2$) depending on the experimental needs.

Other than the two branches I and K, there is a third endstation, EH2, where both soft and hard X-rays can be directed; since the X-ray optics for the two beams need to be different, an additional branch, *branch J*, dedicated to the propagation of soft X-rays and alternative to branch K, is mounted. This endstation features a VG Scienta EW4000 electron energy analyser with nominal resolution below 100 meV at 10 keV. The manipulator allows for x, y, z, θ, ω (polar and azimuthal angles) movements and can be cryocooled down to 15 K.

2.3 ID32 Beamline

The phase I ESRF upgrade from 2009 to 2015 resulted in the construction of 19 new beamlines, and among those was the ID32 beamline (Brookes et al., 2018), dedicated to high-energy resolution soft X-ray Resonant Inelastic X-ray Scattering (RIXS) and soft X-ray dichroism (XMCD/XMLD).

ID32 design needed to meet specific high-end requirements: XMCD applications require tuneable polarisation (linear vertical/horizontal and circular), and RIXS experiments are extremely photon-hungry. For these reasons, three APPLE-II undulators with a 88 mm period have been equipped as insertion devices. After a water-cooled double mirror to focus and collimate the beam in the horizontal plane, a plane grating mono-

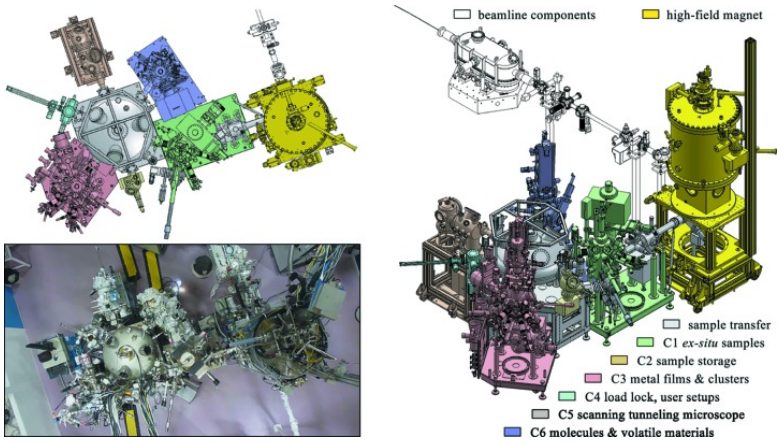

Figure 2.2: Schematics and picture of the ID32 XMCD branch endstation. Other than the high-field magnet chamber, a series of auxiliary chambers for growth and complementary characterisation are available *in situ*. From (Kummer et al., 2016).

chromator (PGM) with four plane gratings (two for each branch - one for high flux and one for high resolution) selects the desired photon energy. The beam follows the same optical path up to this point, but the different purpose of the XMCD and the RIXS endstations call for separate solutions; from now on we will describe only the setup of the XMCD branch, whose endstation is pictured in fig. 2.2 and where measurements in Part III have been performed.

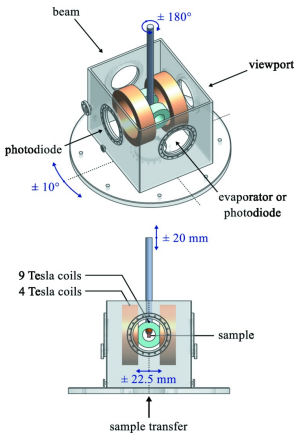

Figure 2.3: Schematics of the measurement chamber and the high-field cryocooled magnet. From (Kummer et al., 2016).

Absorption measurements are performed by continuously scanning the photon energy over an absorption edge; moreover, the working energy range of the beamline needs to be easily changed when moving to a different absorption edge. To maximise working speed only the grating is rotated, and the pre-mirror angle is fixed in a position that optimises the focus on the grating over the whole 400 eV to 1600 eV energy range of the beamline. On top of this, the undulator gap is scanned simultaneously with the monochromator in order to output an approximately constant flux during the scan. The two gratings of $300\,\mathrm{l\,mm^{-1}}$ and $900\,\mathrm{l\,mm^{-1}}$ achieve respectively a resolving power of >5000 and >10 000, and an efficiency of >28 % and 15 %. A cylindrical deflecting mirror ensures the propagation of the monochromatised beam towards the XMCD exit slit and refocusing optics onto the sample position, where a beam size from $\sim 100 \times 10\,\mu\mathrm{m}^2$ to $2000 \times 800\,\mu\mathrm{m}^2$ can be produced.

The endstation (Kummer et al., 2016) is equipped with two split-pairs of superconducting coils which can generate up to 9 T along the beam and up to 4 T orthogonal to the beam (fig. 2.3). The coils are embedded in a bath of liquid Helium at 4.2 K for operation well below the superconductive critical temperature, that doubles as a reservoir for a He^4 continuous-flow cryostat;

the lowest possible temperature on the sample is 5 K. During a measurement, both the total electron yield (TEY) and the total fluorescence yield (TFY) are acquired, by means of measuring the drain current or using a IRD photodiode, respectively.

2.4 APE Beamline

The main idea behind the APE beamline (Giancarlo Panaccione et al., 2009) is twofold: on the one hand, the strive for balance between the specialised nature of a beamline and the more flexible, general-purpose approach of an off-beam laboratory; on the other hand, the purpose of achieving a high level of control in sample preparation, transfer and characterization, depending on the specific requirements of the experiment.

The APE beamline, located at the Elettra storage ring, employs two distinct insertion devices as x-ray sources for a double branch scheme. The two non-collinear helical undulators, of the APPLE-II type, deliver photons of chosen polarisation (linear horizontal, linear vertical, elliptical) at 2 mrad angle in the horizontal propagation plane.

One insertion device, EU12.5, emits in the 10 eV to 100 eV energy range and feeds the far-VUV branch, APE-LE (Low Energy). The undulator is a modified APPLE-II model, where a few horizontally magnetized blocks have been selectively removed and the field amplitude, rather than the period of the permanent magnets, is modulated along the device; this causes a flux reduction, but the quasi-periodicity results in a a strong suppression of high-order contributions, thus providing high spectral purity of the propagating beam after the monochromator stage. The second insertion device, EU6.0, is a standard APPLE-II undulator emitting in the 100 eV to 2000 eV energy range and feeds the soft X-ray branch, APE-HE (High Energy).

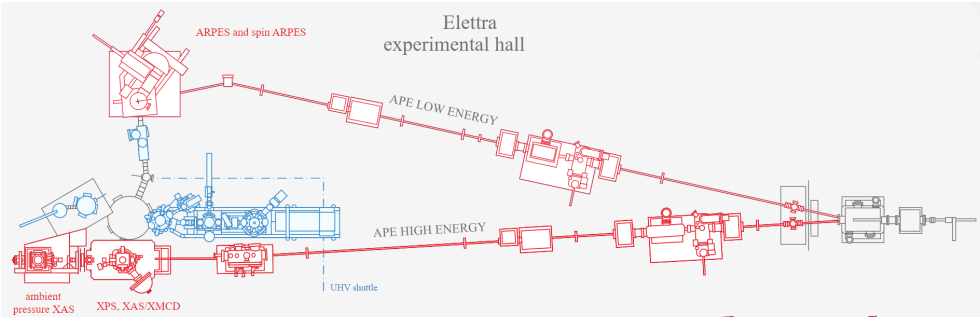

Figure 2.4: Schematics of the APE endstation showing the APE-LE and APE-HE branches. The auxiliary chambers and the glovebox for growth, preparation and complementary characterisation available *in situ* thanks to the UHV shuttle system are not shown here. Adapted from NFFA-Trieste website.

The two beams are about 48 mm distant when they reach the Switching Mirror Chamber, where they are deflected into their respective branches by a pair of silicon spherical mirrors, LEM1 and HEM1. The mirrors sustain a significant heat load (up to 300 W @2.4 GeV, 200 mA ring current). A specifically designed cryocooler system has been designed: a copper block with microcavities is in direct thermal contact with each mirror and keeps the temperature below 100 K, where the silicon thermal expansion/thermal conductivity ratio is much lower than room temperature, even at full radiation power,

while also preventing Helium circulation inside the UHV system and carrying away excess heat.

2.4.1 LE Branch

The LE monochromator is based on twin plane grating - spherical mirror (PGM-SM) assemblies: it features a system of three plane gratings of 700 l mm^{-1}, 1200 l mm^{-1} and 1600 l mm^{-1} to cover the 9 eV to 25 eV, 25 eV to 40 eV and 40 eV to 100 eV energy range, respectively, followed up by a spherical refocusing mirror. The energy resolution is $E/\Delta E$ = 16 000 at 47 eV and $E/\Delta E$ = 13 000 at 63 eV, regardless of light polarisation. A further toroidal mirror then refocuses the beam into a $50 \times 100\,\mu m^2$ spot in the endstation.

The LE branch is mainly dedicated to high-resolution ARPES and Spin-ARPES. The endstation hosts an Omicron-Scienta DA30-L electron energy analyser operating in deflection mode, with a $\pm 14°$ angular range and $<0.2°$ angular resolution. The analyser is complemented with the spin polarimeter VESPA (Very Efficient Spin Polarisation Analysis) (Bigi et al., 2017): two VLEED-based scattering chambers allow the determination of the three-dimensional spin vector while operating the DA30 at the same time, with an angular resolution of $\sim 0.38°$, *i.e.* ~ 0.018 Å^{-1} at 30 eV photon energy, and an overall energy resolution of $\sim$ 70 meV. The manually operated manipulator, with x, y, z, θ, ϕ (polar and tilt angles) degrees of freedom, can be cryocooled down to 15 K on the sample surface. The base pressure in the experimental chamber is always better than 5×10^{-10} mbar. A portion of the experimental work presented in Part II and Part III has been performed in the APE-LE branch.

2.4.2 HE Branch

As with LE branch design, the APPLE-II undulator is followed by a PGM-SM system, whose three gratings (900 l mm^{-1}, 1400 l mm^{-1} and 1800 l mm^{-1}) cover the 140 eV to 1500 eV energy range. In this case, the beam can be horizontally adjusted in size by means of a removable dove tail assembly and focused by a toroidal mirror down to $75 \times 150\,\mu m^2$. The energy resolution is $E/\Delta E > 8000$ at 400 eV and $E/\Delta E \approx 3000$ at >900 eV.

The HE branch is mainly tailored for ambient pressure physics and magnetic circular and linear dichroism experiments. While the former configuration was not employed in our case, and the interested reader should refer to (Castán-Guerrero et al., 2018), the latter contributed to data presented in Part II and Part III. The μ-metal experimental chamber hosts a manipulator with four degrees of freedom, x, y, z and θ (polar angle) and a liquid-flow cryostat allowing to reach 50 K on the sample surface. An UHV-compatible electromagnet provides a (pulsed) magnetic field up to 0.1 T parallel to the in-plane horizontal direction of the sample. XPS measurements are performed using a Scienta R-3000 electron analyser, whereas XAS data are acquired in TEY mode by measuring the drain current.

2.5 SPRINT Beamline

Beamlines such as APE-LE and I09 have developed a solid expertise in realising photoemission spectroscopy experiments under equilibrium conditions, using synchrotrons as a quasi-continuous source (since 500 MHz repetition rate is far above the response time

of any available measurement system). At the same time, the ever-growing field of exploring the physics of non-equilibrium phenomena has prompted the development of ultrafast pulsed light sources. However, if such a task is attempted in a Free Electron Laser (FEL), a machine that allows for a high peak brilliance, but very low repetition rates, and concentrates peak fluxes in extremely short times resulting in spurious effects such as vacuum space charge, the feasibility of any photoemission experiment is radically limited.

Thus, a valid alternative is using tabletop Yb:KGW lasers, ultrafast regeneratively amplified sources with high stability and tunability of the repetition rate, to seed nonlinear phenomena and provide both pump and probe with unparalleled flexibility. The Spin Polarised Research Instrument in the Nanoscale and Time domain (SPRINT) beamline (Cucini et al., 2020) follows this paradigm by resorting to high harmonic generation (HHG) to provide a state-of-the-art bright and stable (in terms of energy, polarisation and intensity) extreme ultraviolet (EUV) pulsed source in the 10 fs to 100 fs timescale with variable repetition rate exceeding 200 kHz, as well as exploiting sum-frequency generation (SFG) to supply low-energy photons for threshold PES. In parallel, optical parametric amplifiers (OPA) are used to deliver ultrashort pump pulses of tunable energy. The adaptability of the SPRINT beamline to different experimental needs makes it by design a high-value facility open to users in the framework of the NFFA-Trieste project.

The SPRINT beamline, located in the FERMI@Elettra hall, employs two Yb:KGW-based integrated femtosecond laser systems (PHAROS, Light Conversion) designed for turn-key operation, producing 300 fs pulses at 1030 nm and variable repetition rate. The cavity reaches maximum peak power (20 W) at 50 kHz and delivers 400 μJ pulses; any increase of the repetition rate, up to the maximum 1 MHz, linearly reduces the energy per pulse: this contributes to the reduction of the peak flux, and thus space charge effects are strongly suppressed at high repetition rates. The repetition rate can also be reduced below 50 kHz by means of a set of Pockel cells; pulse-picking the laser output is useful to optimise non-linear optical processes by reducing the thermal load, since the average power decreases but the same peak power is available. The two lasers work in a "master-slave" configuration: the oscillator in the master laser feeds also the slave laser, in order to achieve pulse synchronisation.

The laser sources can feed three different setups: (i) the OPAs, (ii) the SFG setup and (iii) the HHG setup. First of all, three OPAs provided by Light Conversion, the ORPHEUS-HP, ORPHEUS-ONE-HP and ORPHEUS-F, respectively cover the range of 210 nm to 3230 nm, 1300 nm to 16 000 nm and 640 nm to 2550 nm almost continuously with more than 10 % efficiency. The latter is also equipped with a compressor, resulting in 30 fs to 50 fs pulse length. Secondly, a SFG setup has been tuned for third- and fourth-harmonic generation (3.6 eV and 4.8 eV respectively). Both of the above configurations are built in air and provide a source that enters the UHV system via a viewport in the refocusing chamber, where a silver square mirror directs the beam on the sample. Furthermore, the SFG beams can be employed as pump or probe depending on the experimental requirements, and as such their optical path can be redirected on a delay line.

Concerning the HHG setup, the laser is directly driven into a generation chamber, designed to work in the tight-focusing regime driving the HHG process. A 70 μm glass nozzle applies a pressure in the range from 3 bar to 6 bar; the beam is then focused to a 10(2) μm spot on the gas plume and generates a number of odd harmonics of the seed photon energy. The HHG can be performed both with the base laser photon energy, or with the second harmonic at 515 nm, obtained with a 2 mm thick Beta Barium Borate

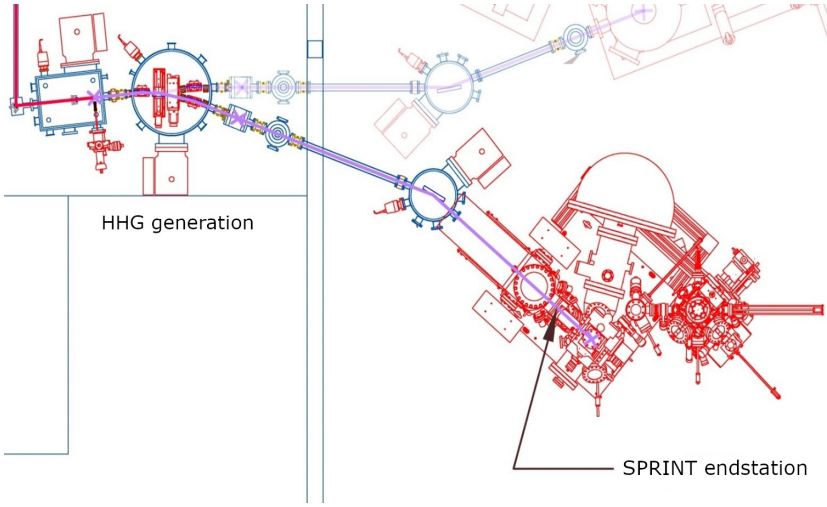

Figure 2.5: Schematics of the SPRINT beamline. On the left, the laser-seeded HHG generation and monochromatisation chambers; on the right, the endstation with the Scienta electron analyser and the vectorial Mott detectors. Adapted from NFFA-Trieste website.

(BBO) crystal with 50 % efficiency. An in-depth explanation of the theoretical description of the HHG process is beyond the scope of this work; without referring to more complex descriptions, the interested reader may find a simple yet exhaustive picture in (Popmintchev et al., 2010).

A cone-shaped beam stopper at the exit of the generation chamber guarantees the transmission of the generated harmonics to the monochromator chamber while dumping $\approx$ 99 % of the input laser radiation power. In the monochromator chamber, a toroidal gold-coated mirror collimates the beam on one out of three off-plane-mount (OPM) plane grating monochromators (200 l mm^{-1}, 400 l mm^{-1} and 1200 l mm^{-1}), performing the spectral selection of single harmonics over the range of 8 eV to 100 eV. Compared to standard grating grooves perpendicular to the incident plane, the off-plane configuration reduces the temporal broadening of the monochromatised pulses, which has been estimated in the range of 50 fs to 100 fs. A second toroidal mirror refocuses the chosen harmonic onto the exit slit towards the refocusing chamber, where a third toroidal mirror images the beam spot at the slits position onto the sample in the experimental chamber. The energy resolution is 22(2) eV and the temporal resolution is 105(45) fs at 16.9 eV photon energy (7$^{\text{th}}$ harmonic), meaning that the setup is close to the transform-limit condition.

The SPRINT endstation is equipped with a Scienta SES 2002 electron energy analyser with a $\pm 7°$ angular range, and a Vectorial Twin Mott detector setup for the measurement of the spin polarisation of the full or partial quantum yield from the sample. The manipulator enables control of four independent degrees of freedom, x, y, z and θ (polar angle) and a cryostat reaching 40 K on the sample surface. The experiments in Part I, apart from some specific ARPES spectra in the first chapter, have been performed entirely at the SPRINT beamline.

2.6 Beamtimes

User facilities such as those presented above dedicate some of their machine time to in-house research or maintenance, but a relevant portion of the year is reserved for external users. Experimental runs performed during the time allocated by beamlines are named *beamtimes*.

While in-house research on a beamline is subject to the decision of beamline scientists only, beamtimes are assigned on the basis of competitive proposal applications. Whoever wants to apply for an experiment submits a proposal describing the scientific background, the detailed experimental plan and the impact of the outcome. A scientific review committee grades the submitted proposals and those at the top of the final ranking are accepted.

The time of an experiment is measured in *beamtime shifts*: each shift is 8 hours of access to the beamline. Generally an experiment is expected to last from 9 to 21 shifts, corresponding to 3 and 7 full days respectively, but in some cases, especially in beamlines performing time-resolved measurements, it is possible to ask for more because an experimental run may require high statistics over several samples.

2.6.1 Experiments

Apart from in-house research, the work included in this thesis is the result of several beamtimes. Application for beamtimes at Elettra, ESRF and Diamond Light Source has been characterised by an 80 % degree of success in proposal approval by committees. Below, the ripartition of the experimental work for each of the topics covered in the thesis is reported.

Part I

Measurements in Part I belong exclusively to in-house research on the SPRINT beamline. The experimental shifts have been spread rather uniformly across all three years of PhD and a precise quantification of the machine time is hard, also because overlaps between actual measurements and stages of development and testing of the instrumentation were not infrequent.

Part II

Measurements in Part II were performed in:

- one beamtime at I09, during the first year of PhD, for a total of 9 shifts;
- one beamtime at APE-LE, during the second year of PhD, for a total of 21 shifts;
- two in-house periods at APE-LE, during the second year of PhD, for a total of 36 shifts;
- one in-house period at APE-HE, during the second year of PhD, for a total of 9 shifts.

Part III

Measurements in Part II were performed in:

- one beamtime at ID32, during the second year of PhD, for a total of 18 shifts;

- one in-house period at APE-LE, during the second year of PhD, for a total of 15 shifts;
- one joint beamtime at APE-LE and APE-HE, during the third year of PhD, for a total of 18 shifts (15 on APE-LE and 3 on APE-HE).

Part I

Fe(001): a model for 3D magnetism

CHAPTER 3

Near-Fermi electronic and spin structure in Fe(001)

> If I die, I have to go before him, and he will ask me, "What is the riddle of steel?" If I don't know it, he will cast me out of Valhalla and laugh at me.
>
> Conan the Cimmerian, *The Tower of the Elephant*

3.1 Overview

The study of magnetism in matter has reached a historical high in terms of variety and complexity of physical phenomena under scrutiny by the scientific community. From topological band states generating quasiparticles that emulate the behaviour of high-energy equivalents to the generation and control of spin waves, the direction of the research has always been pursuing, or straight up engineering, more and more exotic states and samples.

In the quest after understanding the underlying laws governing magnetism, often it is not necessary to look for an out-of-the-ordinary system. Indeed, the populated world of materials exhibiting magnetic properties provides a vast choice in terms of phenomenology and degree of intricacy: some of the more "conventional" ones have been somewhat laid aside in favour of new and exciting oddities, perhaps undeservedly so. The novelty of a topic does not necessarily have to do with its relative importance regarding the physics we can investigate and learn.

In this regard, *3d* transition metals are still the ideal playground for the aim of exploring the fundamentals of magnetic interactions in solids. Fe, Co and Ni are the only elemental *3d* ferromagnets at the solid state, and have been studied with all available methods over the years, providing stringent limits to the development of theories grasping the very fundamental nature of ferromagnetism, and of the related phenomena. They constitute the most evident example of ferromagnetic ordering as a purely quantum effect, with electron spins in a bulk ordering spontaneously to determine macroscopic magnetisation; in a certain sense, they are the epitome of a 3D ferromagnet at ambient conditions.

The competition between bulk and surface properties has also defined a line of research in *3d* ferromagnetic transition metals, leading for example to the to the characterization of truly surface or low-dimensional magnetism. Spin waves at surfaces, anisotropic exchange and surface-atom magnetic moments have been measured by exploiting surface-sensitive electron spectroscopy and electron spin polarimetry as well as optical higher order effects.

In this thesis we address the relaxation from out of equilibrium of iron surfaces, as *e.g.* consequent to sudden excitation of the electronic system by a 50-300 fs pulse of IR radiation. Probing the electron bands with angular resolved photoemission spectroscopy and the spin polarisation of states in the Fermi level region with threshold photoemission spin polarimetry can be accomplished with UV and EUV pulses from 150 fs to 300 fs at variable time delays with respect to the pump excitation.

The rationale of these experiments is to probe the path towards the ferromagnetic ground state of iron surfaces whose electronic and spin structure is temporarily brought well out of the thermodynamic equilibrium. The explored time scale is expected to allow disentangling the various phenomena that collectively represent the heat capacity of the ferromagnet, possibly leading to some new understanding of electron, spin, magnon, phonon correlations.

We set off with a thorough characterisation of the electron states of an Fe bcc at equilibrium at room temperature. On the one hand, ARPES, as a key tool in assessing the surface properties and crystalline order, can be employed to identify key features in the band structure and assess the electronic configuration; on the other hand, exploiting photoemission of very low energy primary electrons by means of threshold photons ($h\nu = 4.8\,eV$) may give access to the spin polarisation of electrons very close to the Fermi level, *i.e.* those who contribute the most to the energy transfer processes.

3.2 Sample growth and preparation

Commercially available MgO(001) one-side polished single crystals have been selected as the substrate of choice for Fe(001) thin films: bcc Fe fits on fcc MgO with a 3.5 % lattice mismatch and epitaxial relation Fe(001)[011]/MgO(001)[110] (Lawler et al., 1997).

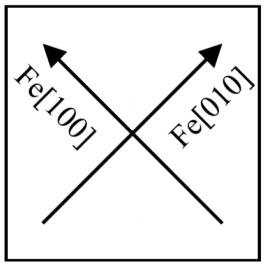

Figure 3.1: Crystalline directions of bcc Fe (slanted arrows) grown on top of fcc MgO (square outline). Adapted from (Zhan et al., 2009).

Since on a MgO(001) surface the Fe [100] and [010] axes are oriented at 45° with respect to the substrate surface plane axes, as illustrated in fig. 3.1, the MgO substrate was mounted at 45° with respect to the sample holder: this way, the Fe crystalline directions are in the plane of rotation of the manipulator.

MgO crystals are mounted on sample holders by means of spot-welded Ta stripes and transferred in the UHV sample preparation chamber (base pressure $< 2 \times 10^{-10}$ mbar), where they are annealed at 800 K for 24 hours. Fe is grown epitaxially by an electron beam evaporator at a rate of ∼3.5 Å per minute, as monitored by means of a quartz microbalance; the thickness of the resulting film is typically ∼40 nm.

When films are thicker than a couple of nanometres, non-uniformities due to the formation of terrace-like structures or islands are quite unlikely. In any case, the sample is annealed at 800 K for 30 min to improve crystalline order at the surface. Low energy electron diffraction (LEED) is performed *in situ* after all steps of substrate and thin film sample preparation.

Finally, the sample is heated up to 450 K and undergoes a O_2 exposure, at 1×10^{-6} mbar for 2 min, equivalent to 90 L (langmuir); the oxygen dosing is followed by flash annealing for 30 s at 900 K to desorb excess oxygen and stabilise the p(1x1) reconstruction.

The p(1x1)O capping layer has the purpose of avoiding surface contamination as much as possible. Atomically clean Fe surfaces are quite reactive to residual gas species like oxygen so that, even in UHV conditions, after some hours the surface properties and spectroscopic signals would be affected by surface pollution. The passivation effect of the p(1x1)O surface determines the long term stability of such samples, under UHV conditions, that maintain their physical properties for several weeks. A LEED image acquired at 90 eV, where bright spots are proofs that the 1x1 reconstruction is well-ordered.

Figure 3.2: LEED picture at 55 eV.

3.3 Results

Measurements presented in this chapter have the purpose of characterising the topmost states of the valence band in a Fe(001)-p(1x1)O/MgO sample by means of ARPES and spin polarimetry.

To this purpose, we used two different setups available at the SPRINT beamline. For ARPES measurements, the photons generated by HHG ($h\nu$ = 21.7 eV) are used; for spin polarimetry, the light comes either from the HHG itself, or from the setup for SHG, emitting 4.8 eV photons.

In addition, we performed measurements with the 1.55 eV beam alone, in order to assess its effects in view of the discussion in the next chapter.

3.4 ARPES and detector calibration

As mentioned in section 2.5, the SPRINT beamline has access to a hemispheric electron analyser with a $\pm 7°$ degree aperture about the average analysis direction. For this reason, to acquire the band dispersion of the whole Brillouin zone the sample normal must be reoriented in steps with respect to the analyser axis by manually rotating the manipulator. Since this was the first angle-resolved measurement with this setup, a precise calibration of the angle-pixels conversion factor is necessary to properly acquire and analyse ARPES data.

For this reason, the purpose of acquiring ARPES data on Fe(001)-p(1x1)O/MgO is twofold: (i) to check the surface quality and oxygen reconstruction, and (ii) to provide a reference on which a calibration of the angular window of the analyser is possible.

An ARPES E vs k map of Fe(001)-p(1x1)O/MgO acquired with $h\nu$ = 21.7 eV photons from HHG is shown in fig. 3.3a. The band structure prominently shows a dispersive feature between 4 eV and 6 eV binding energy: this band is well-known in literature both from calculations and photoemission experiments (Chubb and Pickett, 1987; Clarke et al., 1990; Fink et al., 1992; H. Huang and Hermanson, 1985; Panzner, D. R. Mueller and Rhodin, 1985) and is attributed to the in-plane component p_y of the $2p$ oxygen orbitals.

EDC cuts across the probed angles, seen in fig. 3.3b, allowed us to retrieve the angular positions of the O p_y peak. The conversion from angle to k-vector, given by eq. (1.5), is performed as follows. Since the $\bar{X}$ symmetry point in bcc Fe lies at 1.11 $Å^{-1}$, an opportune rescaling of the x axis - when in angular scale - would yield the correct angular width of the analyser window: this factor has been used to calibrate the analyser.

In the first Brillouin zone, between the $\bar{\Gamma}$ point and the $\bar{X}$ point, we can see a faint photoemission dispersive signal above 1 eV up to $\sim$ 0.2 eV binding energy; part of this

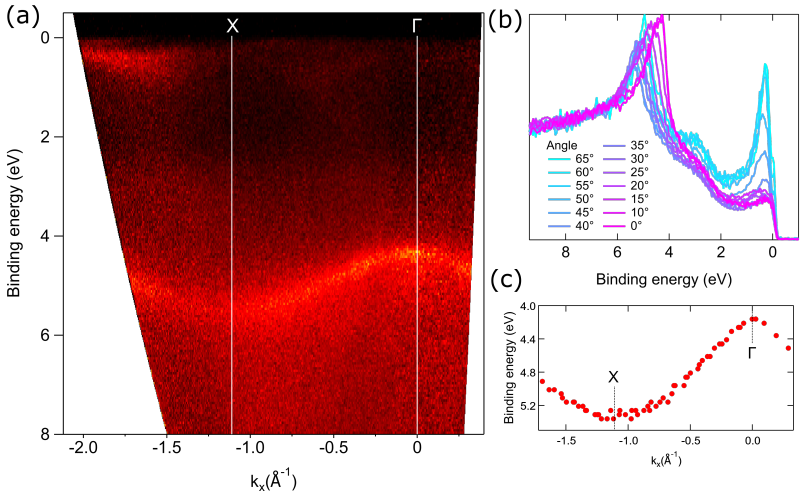

Figure 3.3: (a) E vs k map acquired at hν = 21.7 eV on Fe(001)-p(1x1)O/MgO . (b) EDCs at emission angles between 0° and 65°; the dispersion of the O-derived peak is clearly visible. (c) Dispersion of the O p_y peak as rescaled in terms of k, used to calibrate the analyser angular window.

band is replicated with much higher intensity in the second Brillouin zone. This is most likely a bulk Fe band, the $d_{(x+y)z}$, which is spin-split: the bright signal in the second Brillouin zone can be attributed to the $d_{\downarrow(x+y)z}$ component, which is closer to $\bar{\Gamma}$ and displays hole-like dispersion, whereas the feature closer to $\bar{X}$ is the $d_{\uparrow(x+y)z}$. In the second Brillouin zone a tiny signal appears also above $\sim$ 0.2 eV at around 1.8 Å^{-1}, while it is undetected in the first Brillouin zone. The reason for the large difference in photoemitted intensity between the first and the second Brillouin zone can probably be traced in matrix elements effects.

The spectrum in fig. 3.3 allows to confirm that the p(1x1)O reconstruction is well-ordered on the Fe surface; however, band structure information, especially in the near-Fermi region, are difficult to interpret. For this reason, we can refer to ARPES and Spin-ARPES measurements performed on an analogous Fe(001)-p(1x1)O/MgO sample in the APE-LE beamline (section 2.4).

In fig. 3.4 the Fermi $k_x - k_y$ isoenergetic surface map and the band dispersion of Fe(001)-p(1x1)O/MgO are displayed. The Fe(001)-p(1x1)O/MgO Fermi surface is characterised by several features, marked with Greek letters. In particular, the region near $\bar{\Gamma}$ is dominated by a ring-shaped (α) and a diamond-shaped (β) state; they are attributed by DFT calculations to oxygen-induced surface states.

The angular dispersion along $\bar{\Gamma} - \bar{X}$ via E vs k maps gives additional information to uncover the details of the band structure. We notice in fig. 3.4b-c that α and β bands show electron-like character and can be related to the tiny feature above 0.2 eV in the second Brillouin zone in fig. 3.3a.

By performing Spin-ARPES on α and β bands, as well as on the entirety of the Fermi surface in fig. 3.4a, it has been shown that the two oxygen-derived states have minority character, while the rest of the Fermi surface is dominated by majority character (Fujii, in preparation).

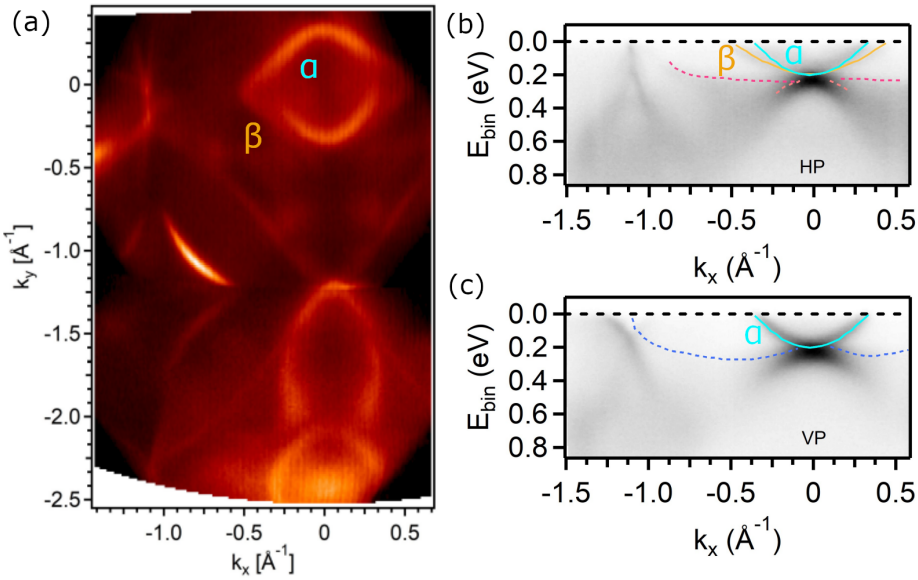

Figure 3.4: (a) Fermi $k_x - k_y$ isoenergetic surface map acquired at $h\nu$ = 50 eV on Fe(001)-p(1x1)O/MgO . (b-c) E vs *k* maps of the band dispersion of Fe(001)-p(1x1)O/MgO along $\bar{\Gamma} - \bar{X}$, acquired at $h\nu$ = 50 eV with horizontal (b) and vertical (c) linearly polarised radiation (HP and VP). Teal and ochra lines highlight α and β bands, respectively; dotted lines denote other surface states. Adapted from (Finardi, 2020).

3.5 The dilemma of threshold magnetic measurements

The measurement of the spin polarisation of low-energy secondary electrons from magnetic crystals has a long history, starting from the pioneering work by (Kisker, Gudat and Schröder, 1982) on Fe and Co; soon, other results from Ni (Hopster et al., 1983; Landolt and Mauri, 1982) and $Fe_{81.5}B_{14.5}Si_4$ (Unguris et al., 1982) confirmed the trend noticed earlier. At low electron energies the spin polarisation progressively increases, reaching a maximum value at the lowest kinetic energy. The explanation of this phenomenon generally follows spin-filtering arguments, as the electrons have a spin-dependent scattering probability related to the availability of spin polarised empty states (Penn, Apell and Girvin, 1985).

Photoemission at threshold energy (*i.e.* as excited by photons of energy just exceeding the sample work function) also generates very low energy photoelectrons. However, in this case, the ejected electrons are elastic, i.e. not affected by scattering to lower energy states. Very low-energy electrons have lower probability of inelastic scattering (Farnsworth, 1926): the electron mean free path is correspondingly quite long, of the magnitude of $\sim$ 10 nm (Marx et al., 2003; Seah and Dench, 1979).

This means that the photoelectron yield at threshold is dominated by primary "elastic" photoelectron originating from states lying on the Fermi surface or at slightly higher binding energies. This fact has been exploited in various instances, as in X-ray photoemission from Fe *2p* by (Offi et al., 2007).

The spin polarisation of secondary electrons, *i.e.* photoelectrons that have suffered multiple inelastic scattering events before being ejected with very low residual kinetic

energy, is known to be proportional to the average magnetisation of the solid, and can therefore be used as a relative magnetometry. Primary electrons, on the other hand, carry information about the in-band initial state spin polarisation. In our case the threshold photoemission regime does select a narrow range of photoelectron energies, corresponding to the difference between photon energy and average work function of the sample surface. The narrow energy range of photoexcitation reduces considerably the likelihood of ejecting scattered photoelectrons, so that the signal has no "secondary tail". Furthermore the low kinetic energy of the photoemitted signal does correspond to a large mean free path and the data are therefore less surface-sensitive than at higher photoexcitation energies.

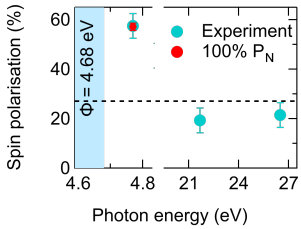

Figure 3.5: Comparison between measurements of spin polarisation at threshold ($h\nu$ = 4.79 eV) and at HHG ($h\nu$ = 21.7 eV, 26.5 eV) energies. The horizontal dotted line marks the expected value of n_B/n = 27.5 % for the average spin polarisation of the whole Fe *d* band. The expected value of the in-band spin polarisation (in red) is discussed in-text.

Figure 3.5 substantiates the claim that a measurement at threshold yields different results from the same procedure performed at higher energy photons. The value of the spin polarisation at threshold is indeed much higher compared to the values at 21.7 eV and 26.5 eV photon energy, which are closer to the expected average band polarisation marked by the dashed line.

In order to assess which electronic bands do effectively contribute to the threshold photoemission signal, we refer back to ARPES measurements of the band structure of Fe(001)-p(1x1)O/MgO ; in particular, a zoomed-in region of the band dispersion in fig. 3.4b-c can be seen in fig. 3.6 at two different photon energies: the α and β bands are evident up to 0.2 eV binding energy at $\bar{\Gamma}$, as well as the bulk B state at higher binding energies.

In our setup, an extraction field (V = 100 V) is applied between the sample and the Mott detector electrostatic lenses, thus the emission angle is averaged and there is no momentum selection. In any case, a threshold photoemission experiment performed with 4.8 eV does not give access to occupied states in the whole Brillouin zone, because the maximum accessible $k_{\parallel}$ is linked to the kinetic energy of the photoelectrons and to the emission angle (eq. (1.5)). For this reason, we are able to probe a reduced portion of the band structure compared to EUV photons, as highlighted in fig. 3.6.

From this consideration it is clear that photoelectrons excited from threshold photons in our experiments cannot originate from the oxygen-derived α and β states, neither from the B bulk state. This is consistent with our spin-resolved measurement at threshold, because all the aforementioned bands have minority character. Measuring minority electrons would result in a high value of the spin polarisation, but with *opposite sign* compared to the signal of secondary electrons; fig. 3.5 instead shows that both spin polarisations have the same sign.

From a closer inspection of fig. 3.6a, an electron pocket at $\bar{\Gamma}$ lying inside the boundary of threshold photoemission is visible in the ARPES E vs *k* map at 21 eV photon energy. Probably, matrix elements effects prevent this state to be revealed at 25 eV photon energy.

The electron pocket is not a surface state, nor does it belong to oxygen-derived states. We may hypothesise that this state is a bulk Fe state. On the basis of the spin texture of the Fermi surface of Fe(001)-p(1x1)O/MgO samples, which indicates that α and β are minority bands whereas the Fe-derived states at the Fermi surface are dominated by

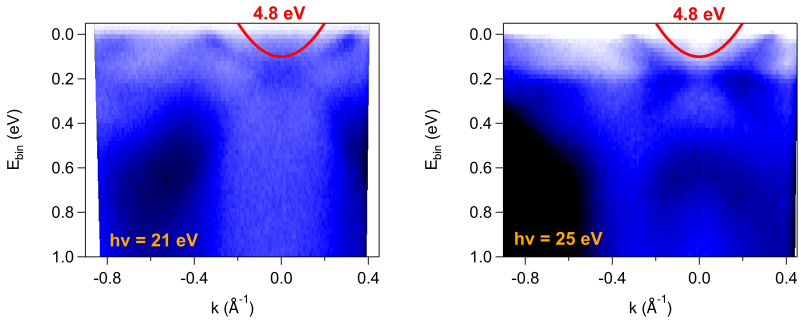

Figure 3.6: E vs k maps of the band dispersion of Fe(001)-p(1x1)O/MgO along $\bar{\Gamma} - \bar{X}$, acquired at (a) hν = 21 eV and (b) hν = 25 eV. The red solid line indicates the portion of the band structure probed by 4.8 eV threshold photons.

majority electrons (Fujii, in preparation), we can expect the character of this state to be of majority spin, which is consistent with the high spin polarisation measured at threshold.

Since we concluded that the measured value of the spin polarisation is a measure of the initial spin polarisation from Fe bulk states accessible with threshold photons, it can be compared to the values presented by (Mazin, 1999). A spin polarimetry measurement on Fe is generally defined by the difference in density of electronic states between the ↑ and ↓ spin population, which is essentially given by d electrons; this is called the "N" definition of the spin polarisation. Transport measurements instead are *not* defined by the DOS alone, and make use of the "Nv^2" definition, which takes into account the Fermi velocity of the bound electrons (high for light s electrons, low for heavy d electrons). This difference (which can be extremely relevant, as for example in Ni) is only quantitatively different in Fe (fig. 3.7), and has no influence on spin polarimetry measurements, so we can safely use the N definition.

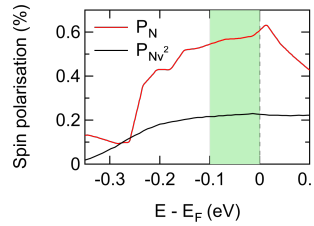

Figure 3.7: Calculated Fe spin polarisation as a function of binding energy, following "N" and "Nv^2" definitions. The shaded green area represents the binding energy region probed by 4.8 eV photons. Adapted from (Mazin, 1999).

If we consider the value of spin polarisation (P_N) integrated over the binding energy range reached by threshold photoemission, we obtain a spin polarisation of 57(2) %, as indicated by the red mark in fig. 3.5, which is compatible with the value we measured.

In principle, the spin polarisation of threshold photoemission should refer to the initial state properties of the occupied electron band we identified in the energy neighbourhood of the Fermi surface. However, in reality a measurement mixes both surface and bulk contributions and a minor, but hard to quantify, contribution of scattered electrons. Moreover, surface defects can modulate the effective work-function; in addition, the presence of magnetic domains not fully aligned at remanence may reduce the magnetisation and consequently the effective spin polarisation, that is given by the vectorial sum of all contributions falling within the photoexcitation light spot.

We note that in order to evaluate the fraction of secondary electrons contributing to the signal at threshold, we cannot actually compare the spin polarisation measured at

photoemission threshold and the spin polarisation resulting from the secondary electrons cascade when the photoexcitation is due to EUV photon energies in fig. 3.5: as mentioned earlier, the spin polarisation of secondary electrons is highly dependent on their energy, with a sharp increase at low kinetic energies (Kisker, Gudat and Schröder, 1982; Paul et al., 1991). For this reason, an exact quantification of the contribution of secondary electrons towards the threshold spin polarisation signal is extremely hard to perform.

One should also consider that (Riccardo Bertacco and Ciccacci, 1999) demonstrated an enhancement of spin polarisation in connection with the p(1x1)O surface reconstruction and attributed it to a surface relaxation causing a larger Fe-Fe distance at the interface with oxygen. In order to estimate the possible contribution of the oxygen adlayer to the high value of spin polarisation measured in threshold photoemission, we need to assess the surface sensitivity of our data.

3.6 Surface ageing and spin polarisation evolution

E vs k maps prove that the Fe surface is uniformly passivated with oxygen and that the reconstruction is well-ordered. Not having access to band dispersion in threshold photoemission we periodically monitored the spin polarisation signal and the EUV-photoexcited EDCs, to probe possible degradation in time. As we will see, this procedure yields an additional information.

If contaminants hamper the signal from the sample surface, an EDC instantly recovers this information: in fig. 3.8 the red curve shows both the feature close to the Fermi level and the O band at $\sim$5.5 eV, whereas the black curve is the result of an exposure to a pressure of 10^{-8} mbar (*i.e.* exposure to gas with the same composition as the residual UHV pressure, but increased by a factor 100) showing a loss of spectroscopic features due to sample surface contamination.

Conversely, spin polarisation data shows a different phenomenology. If photoemission is measured by 4.8 eV photons, selecting only electrons close to the Fermi level, a sizeable spin polarisation appears in both cases. This is a consequence of the large mean free path of low-energy photoelectrons that correspond to a reduced surface sensitivity of the measurements. On the other hand, EDCs as excited with 21.7 eV photons reflect band states in the final state spectra in the range from 10 eV to 17 eV kinetic energy, that is close to the minimum of the universal curve of escape depth with values < 1 nm. The inset in fig. 3.8 highlights the energy region of the spectrum that a 4.8 eV photon is able to excite, together with the measured spin polarisation.

This result confirm that threshold photoelectrons are less sensitive to surface composition, *i.e.* are more bulk-sensitive compared to the UV-EUV photoemission spectra: our spin polarisation measurements thus reflect bulk properties of the sample material.

In conclusion, our threshold photoemission data yield a high value of spin polarisation that reflect the bulk states near Γ that are mosty of majority spin character. The limited integration across the Brillouin zone cannot reflect the absolute value of spin polarisation of the occupied states near the Fermi level, but it is a good indicator. The role of surface-enhanced magnetic moment of Fe(100) or of the surface modified contribution by the p(1x1) oxide layer are non prominent due to the relatively long escape depth of the measurement at threshold conditions.

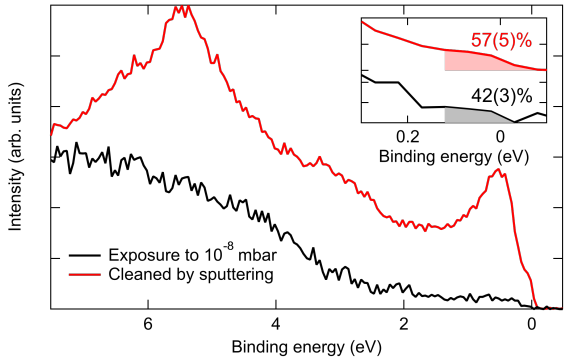

Figure 3.8: EDCs of Fe(001)-p(1x1)O/MgO , measured at hν = 21.7 eV: the black curve is measured after the exposure to 10^{-8} mbar of residual pressure in the UHV system, the red curve is measured after the same sample has been cleaned by sputtering+annealing. The inset shows a magnification of both curves near the Fermi level, where the black and red shaded areas represent the electron yield of the spectrum whose spin polarisation has been probed by 4.8 eV photons; the measured spin polarisation and its error is written in the corresponding colour.

3.7 Probe characterisation: fluence dependence and space charge effects

The 4.8 eV beam, used in the next chapter as a probe, is generated by SHG sequentially by means of two BBO crystals; since the non-linear process is more efficient than gas-generated HHG, the pulses retain a relevant portion of the intensity of the seed laser.

By using pulsed lasers and their harmonics as source for spectroscopy, one is faced with intense photon pulses concentrated in few-fs interval. This can readily determine the so-called space charge effect, that blurs the ejected electron spectra, acting as an electrostatic lens in front of the photoexcited surface. On top of this, at high laser pulse power multiphoton photoemission may also take place. These effects do hamper the spin polarisation measurement, at least in view of its interpretation as Fermi surface property.

EDCs acquired at hν = 4.8 eV in fig. 3.9 show how an increased laser fluence progressively broadens and distorts the spectrum due to the space charge. Additionally, a second photoemission peak gradually appears above 10 eV kinetic energy. The proper conditions for spectroscopy are therefore those that generate the thicker purple curve with markers: the photoemitted yield is completely dominated by single-photon photoemission, is represented by the thicker purple curve with markers, therefore we adopted these laser parameters as the upper limit in our experiments. In any case, the contribution of two-photon photoemission is clearly visible only in logarithmic scale.

The measurement geometry, *i.e.* the angle of light incidence on the sample surface, is another experimental parameter that determines the effective beam fluence on the sample surface (due to the changes in photon density given by the spread of the laser spot over the sample surface). The total electron yield in fig. 3.10, acquired by measuring with a picoamperometer the sample neutralisation (drain) current, shows a square root dependence on the laser power (fit parameters in table 3.1), which we attribute to space

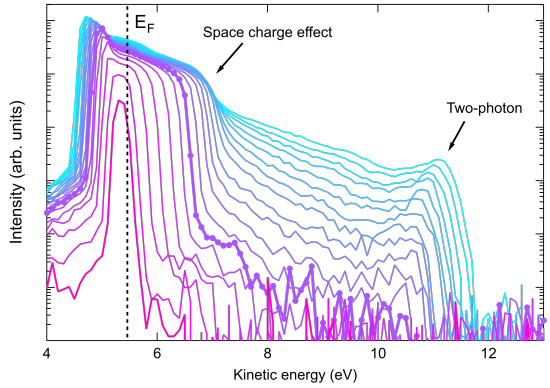

Figure 3.9: EDCs acquired at $h\nu = 4.8\,eV$ as a function of laser power. The sample was biased with –5 V. As the fluence increases, the space charge effect artificially shifts electrons near the Fermi level to higher kinetic energies, and a second peak due to two-photon photoemission appears above 10 eV kinetic energies. The thicker purple line with marker represents the maximum power we used in our experiments.

charge effects. This conclusion is consistent with the fact that at normal incidence ($\theta_i = 0°$) the light spot is concentrated into a smaller surface: this implies a higher fluence, but yields a lower photoemission intensity due to the denser space charge cloud that limits the photoemission current.

Parameters	y_0 (pA)	A (pA mW^{-1})	B (arb. units)
Normal incidence	–58(13)	31(4)	0.48(2)
Grazing incidence	–147(26)	75(10)	0.43(2)

Table 3.1: Fit parameters for photoemission from the probe at 4.8 eV photons.

Our observations are further supported by the detailed study in (L.-P. Oloff et al., 2016). In particular, the authors evaluate the contribution of the incidence angle to space charge phenomena affecting HAXPES measurements; even if the photon energy is wildly different from our setup, we can trace qualitative similarities based on general trends. In fig. 3.11 the dependence on the incidence angle of the photoemission signal and of the kinetic energy shift induced by the space charge are plotted.

Intuitively, an increased photoemission yield at grazing incidence, and consequently a stronger space charge effect, would be expected, for two reasons: (i) at grazing incidence, a reduced photon penetration depth excites more electrons closer to the surface, with a λ_{IMFP} greater than their escape depth, and (ii) the maximum electron emission condition for our geometry is reached at grazing incidence and normal emission, due to the orientation of the light polarisation vector (4.8 eV photons are p-polarised).

Conversely, data in fig. 3.11 show the opposite behaviour, in accord with our measurements. As the incident angle increases, the effects of space charge on photoemission spectra reduce the photoemission intensity as well as increasing the energy shift of the photoelectrons towards higher kinetic energies.

A grazing angle configuration means that electrons are photoexcited from a larger

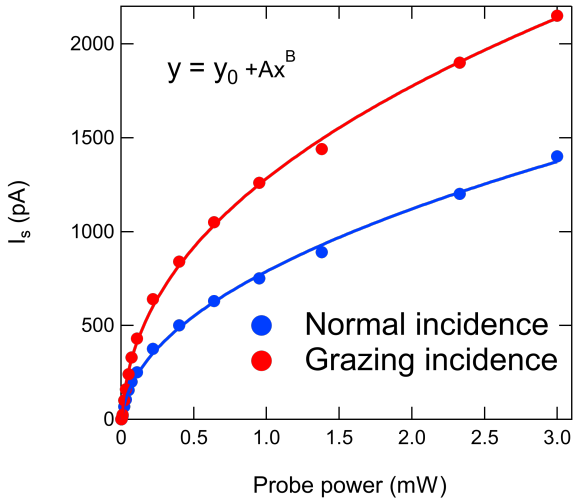

Figure 3.10: Sample current, equivalent to total electron yield, from 4.8 eV photons as a function of the laser power, at normal incidence ($\theta_i = 0°$) and grazing incidence ($\theta_i = 50°$).

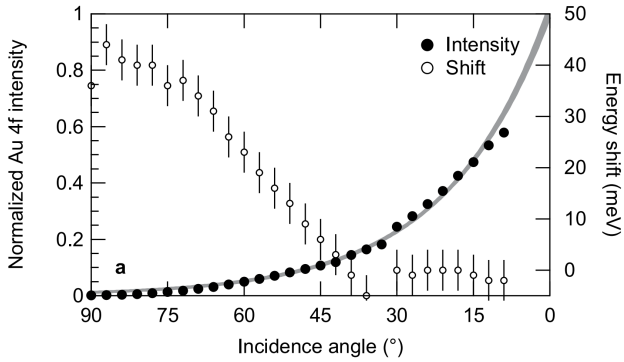

Figure 3.11: Normalised photoemission signal from Au *4f* core level spectra and corresponding space charge-induced shift ($h\nu = 600$ eV) as a function of incidence angle with respect to the sample plane. Adapted from (L.-P. Oloff et al., 2016).

area, because of the spread of the beam on the sample surface, therefore photoelectrons interact less with each other. In other terms, the elongation of the beam spot changes the spot eccentricity $\epsilon = \sqrt{1 - a^2/b^2}$: a higher ϵ, *i.e.* a more elongated beam, has been noted to have a large impact in the reduction of space charge due to the above effect. This is fully consistent with our observations: we also note an increase of the gap between the two photoemission yields with the increase of the laser power, corresponding to an incremented space charge effect.

3.8 Pump characterisation: multiphoton photoemission and surface quality

The IR pump pulses at 800 nm ($h\nu$ = 1.55 eV) were provided by the ORPHEUS-F OPA, whose pulse duration ranges from 30 fs to 50 fs.

Photoemission from pump pulses can occur only when simultaneously absorbing multiple photons, in order to overcome the threshold in vacuum photoionisation. In order to run well-controlled experiments, the pump contribution to the photocurrent must be measured and procedures to minimise it shall be found and adopted.

Figure 3.12a showcases the dependence of the total yield on the pump power. Just like the equivalent measurement we already saw for the probe beam, power laws whose fit parameters are given in table 3.2 seem to be adequate in describing the trend of the curve. Differently from the probe, however, the fit exponents are greater than 1 for both normal and grazing incidence (3.9(2) and 3.2(1), respectively).

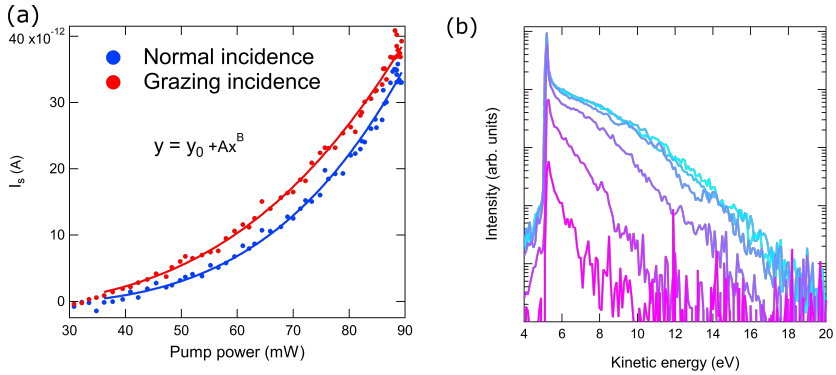

Figure 3.12: (a) Sample current as a function of the pump laser power. (b) EDCs acquired at 800 nm ($h\nu$ = 1.55 eV) as a function of laser power. The sample was biased with –5 V. The laser power ranges from 12 mW to 65 mW (fuchsia and teal curves respectively) and was not increased further to avoid detector saturation issues.

Parameters	y_0 (pA)	A (nA mW^{-1})	B (arb. units)
Normal incidence	–0.6(5)	430(160)	3.9(2)
Grazing incidence	–0.8(6)	80(21)	3.2(1)

Table 3.2: Fit parameters for only pump photoemission at 800 nm ($h\nu$ = 1.55 eV).

Higher-order dependence of the photoemission yield on the laser power is generally agreed upon to be a signature of multiphoton photoemission (Pasmans et al., 2016; Reutzel, A. Li and Petek, 2020): the yield scales with a power-law coefficient that approximates the photoemission order. At normal incidence the laser fluence is higher, thus a higher power-scaling law associated with 4-photon photoemission (B_4 = 3.9(2)) takes precedence compared to grazing incidence, while the signal from the lower order given by 3-photon photoemission (B_3 = 3.2(1)) fades out.

In any case, we can be sure that other phenomena are contributing to this process. By looking at EDCs acquired with 800 nm photons as a function of fluence in fig. 3.12b, it is clear that space charge effects are deforming the photoemission tail at kinetic energies above the secondary peak. Such broad high kinetic energy tail has to be understood.

We have mapped the photoyield across the sample surface at fixed pump power, as seen in the 2D current intensity diagram in fig. 3.13. The current turns out to be quite inhomogeneous across the surface: some spots are much brighter than the rest. A combination of local variations of work function and surface defects (roughness) determining local-specific space charge clouds may describe the observation of such "photoemission hotspots".

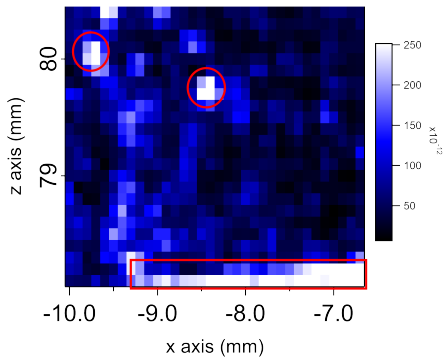

Figure 3.13: 2D total yield (drain current) map acquired at 800 nm (hν = 1.55 eV). Red lines highlights regions of the sample where photoemission is greatly enhanced.

Indeed, edges with a low curvature radius display greater surface charge density and a strong local electric field: highly nonlinear phenomena may result from such a strong field photoemission, as if locally the sample behaves like a sharp metal tip (Bormann et al., 2010; M. Krüger et al., 2012; Schenk, Michael Krüger and Hommelhoff, 2010), with the result of affecting the kinetic energy of photoelectrons and broadening the spectra seen in fig. 3.12b.

We can see how the pump photoemission can be used also to assess the surface quality and find the best suited region where to carry out measurements. This is a similar case to that of (Aeschlimann, Schmuttenmaer et al., 1995) on Cu(110) and Cu(100) and (Rhie, Dürr and Eberhardt, 2003) on Ni/W(110), where the sample position was also optimised on the basis of this effect.

As a consequence, minimising the pump photoemission is not only a matter of decreasing the pump fluence, but involves also the choice of a good spot on the sample - for this reason, we always performed experimental runs away from hotspots to suppress spurious pump signals.

3.9 Closing remarks

In this chapter, we characterised the Fe(001)-p(1x1)O/MgO sample by ARPES and spin polarimetry, as well as decribing the phenomenology of space charge and multiphoton photoemission (and how to avoid or minimise both) due to low-energy photons that will be combined as pump and probe beams for the experiments presented in the next chapter.

We were able to confirm that the surface is well-ordered and reproduces the correct oxygen reconstruction. The measured spin polarisation at threshold represents a value, averaged in energy around the Fermi level with broadly integrated *k*-values, that coincides with the P_N estimate of in-band spin polarisation. Moreover, we ascertained that the probing depth of threshold photoemission is much higher compared to EUV photoemission, thanks to the high mean free path of low-energy electrons. This last point will prove critical in the analysis of time-resolved data and the determination of the relative importance of competing phenomena.

CHAPTER 4

Ultrafast dynamics of electronic and spin excitations in Fe(001)

> Why do you always try to invalidate all of your own results?
> From now on, every time you tell me something you measured may be wrong and we have to do another year-long run of measurements, I will just ask "Why? Why should it be the other way around? Now prove to me the opposite is true instead!".
>
> Giancarlo Panaccione, 2022

4.1 Overview

The pioneering work of (E. Beaurepaire et al., 1996) on a Ni film has sparked a widespread interest in the ultrafast dynamics of the magnetisation in thin films of *3d* transition metals. The direct observation, by means of a Magneto-Optical Kerr Effect (MOKE) setup, of a high signal sensitivity on the subpicosecond time scale has prompted an interpretation in terms of quenching of the material magnetic moment in the timescale of hundreds of femtoseconds, *i.e.* thousand times faster compared to what had been known until then on Gd (Vaterlaus, Beutler and Meier, 1991).

Since then, a variety of techniques were applied to a number of different systems in order to ascertain if this behaviour is common to all *3d* transition metals. Many studies agree upon the fact that a rapid demagnetisation takes place in hundreds of femtoseconds, followed by a partial recovery within 1 ps, and then converging to the initial value in a time range extending to up to the nanosecond. The experimental effort to address ultrafast demagnetisation/remagnetisation in transition metal ferromagnets include mostly MOKE (Bigot, Vomir and Eric Beaurepaire, 2009; Carpene, Mancini et al., 2008; Dalla Longa et al., 2007; Güdde et al., 1999; Koopmans, Kampen et al., 2000), low-energy electrons spin-resolved photoemission (Aeschlimann, Bauer et al., 1997; Cinchetti et al., 2006; Weber et al., 2011), M-edge resonant Kerr spectroscopy (La-O-Vorakiat et al., 2009) and spin-resolved photoemission of secondary electrons measured with X-rays (Fognini et al., 2014).

It is ascertained that photons emitted by a femtosecond laser are absorbed by electrons close to the Fermi level, whose distribution is driven out of equilibrium and relaxes by means of electron-electron and electron-phonon scattering. The addition of the sensitivity to the magnetic order in ferromagnetic materials results in an ultrafast change

of the spin polarisation upon absorption of laser pulses in the optical wavelength range. The new physical timescale addressed with ultrashort light pulses (laser, HHG, FEL) implies a novel understanding of the employed spectroscopies, typically performed in the linear regime (first-order perturbation theory) corresponding to single local photoexcitation of a thermodynamic ground state. When the pulse intensity is high in a short time the signals may reflect a perturbed ground state and new correlations may be reflected in the signals.

On the physics of the material side we need to identify the mechanisms that could lead to ultrafast magnetic phenomena, challenging the somewhat "fundamental" reference timing of the precession of the electron $\tau_L = 1/\omega_L = \hbar/(2\mu_B H)$ which amounts of 36 ps in a field of 1 T, but can be shortened to 10 fs in an exchange field of 3×10^3 T.

The phenomenological model proposed by (E. Beaurepaire et al., 1996), known as the *three-temperature model* due to extending the modelisation of the two-temperature model (Anisimov, Kapeliovich and Perel'Man, 1974) to magnetic materials, provides a concise description together with an understanding of the quantities at play. The ground state of the system is described by three interacting energy reservoirs: the conduction band electrons with an electronic temperature T_e, the ionic lattice with a phononic temperature T_p and the electronic spins with a spin temperature T_s. The thermodynamic equilibrium is reached when the three reservoirs become in mutual equilibrium through interaction mechanisms described by cross sections and time constants.

In a pump-probe experiment, an ultrashort pump photon pulse excites the electron bath, whose temperature suddenly increases;[1] the excess energy gained is then transferred to the other subsystems depending on the specific coupling constants. In fig. 4.1 a cartoon representing the energy transfer between reservoirs, as well as experimental data compared to calculations found in (E. Beaurepaire et al., 1996), are displayed.

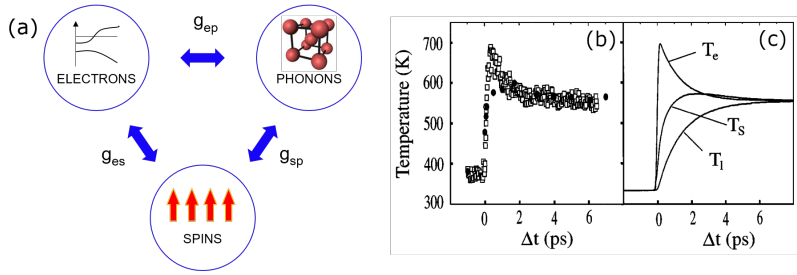

Figure 4.1: (a) Schematic representation of the three-temperature model illustrating the interaction between the electronic, phononic and spin reservoirs. (b) Experimental electronic temperature T_e and spin temperature T_s as a function of the time delay; (c) calculated electronic temperature T_e, lattice temperature T_l and spin temperature T_s as a function of the time delay. (b-c) are adapted from (E. Beaurepaire et al., 1996).

The description of the demagnetisation is thus essentially formulated as the transfer of angular momentum from electrons or phonons to the spins. Nevertheless, it is not straightforward at all to identify the channels and the effects of this angular momentum transfer.

[1] In the first few femtoseconds of the excitation, when the electronic system is driven far out of equilibrium, there is little meaning in a parameter like T_e, because the temperature is obviously ill-defined. However, if the band structure is not modified too much by the excitation, the subsequent relaxation towards a thermal distribution allows for the definition of a temperature. We will deal with this matter in the discussion of results.

To the purpose of unveiling the processes governing the ultrafast demagnetisation, a great deal of interest has been focusing on the role of band energy shifts and collective spin excitations. The thorough energy, spin and time-resolved work of (Eich et al., 2017) on Co demonstrated that the Stoner collapse of the spin splitting is not supported, and the fundamental contribution to the magnetisation quenching is provided by rapid band mirroring. At the same time, the role of spin-flip excitations in the magnetisation decrease has been questioned: the authors argue that in their sample the dynamics near the Fermi level is dominated by carriers redistribution, whereas at higher binding energies superdiffusive spin currents are responsible for the band mirroring.

It is challenging to formulate a uniform picture and find the boundaries where one effect stops being predominant over the others. In particular, some questions remain unanswered. How does the use of low-energy photons - besides the obvious concern of Brillouin zone sensitivity - influence the measurement of the spin polarisation? Do complementary measurements of electronic temperature and spin polarisation contribute to the identification of the microscopic mechanisms governing ultrafast magnetic moments quenching? And is it possible to combine the information derived from both of them in one uniform and coherent picture?

The above questions are the inspiration for the concerns that we are going to address hereinafter. As a ferromagnet belonging to the *3d* transition metals group, Fe is a good candidate for this study; we will rely on the the Fe(001)-p(1x1)O/MgO system we characterised in the previous chapter.

4.2 Space charge effects in pump-probe

In the previous chapter, we exemplified the expedients we may take when reducing the space charge induced by the pump pulse. Even if we strived for the minimisation of space charge effects, we note that they still do affect time-resolved measurements in some way. The pump-probe dataset displayed in fig. 4.2 is an example where we can clearly see these effects at play. EDCs are acquired for each delay time and merged into one 2D colour scale picture, a delay map (fig. 4.2a). As we already mentioned, the secondary electrons peak dominates the overall intensity spectrum; however, a zoom of the delay map (fig. 4.2b) showcases the small intensity variations due to the electron dynamics near the Fermi level. Integrating the kinetic energy in different ranges and comparing the resulting delay curves (fig. 4.2c) highlights that the dynamics of the whole spectrum is both broad and slow. If a small region close to Fermi is integrated, we see that a much sharper and faster dynamics is superimposed to the slow background.

Indeed, the slow temporal evolution of the whole integrated spectrum, and in particular the presence of a slow dynamics at negative delay times that keeps on decreasing even before -4 ps, is coherent with the dynamics of the space charge. On the other hand, the fast peak encompasses just a few picoseconds, therefore its origin should not be related to space charge (cfr. also the first two curves from the bottom in fig. 4.2d, where at lower kinetic energies secondary electrons display a broad peak while electrons of higher kinetic energy are quite faster). This is a well-known behaviour, found in pump-probe measurements when the pump fluence is not too low and discussed in good detail by (Al-Obaidi et al., 2015; L. Oloff et al., 2016; Pelli Cresi et al., 2022; Verna et al., 2020).

The ultrafast dynamics in the neighbourhood of the Fermi level contains the information we are looking for, *i.e.* the response of valence electrons to an ultrafast optical excitation. At 4.8 eV photon energy, space charge effects are hardly completely erasable and render the retrieval of these information difficult: for this reason, using the much less intense HHG source as probe of the ultrafast electron dynamics is more suited for

the purpose due to the suppression of space charge effects: in following sections we carried out energy-resolved measurements only with EUV energies originated from HHG.

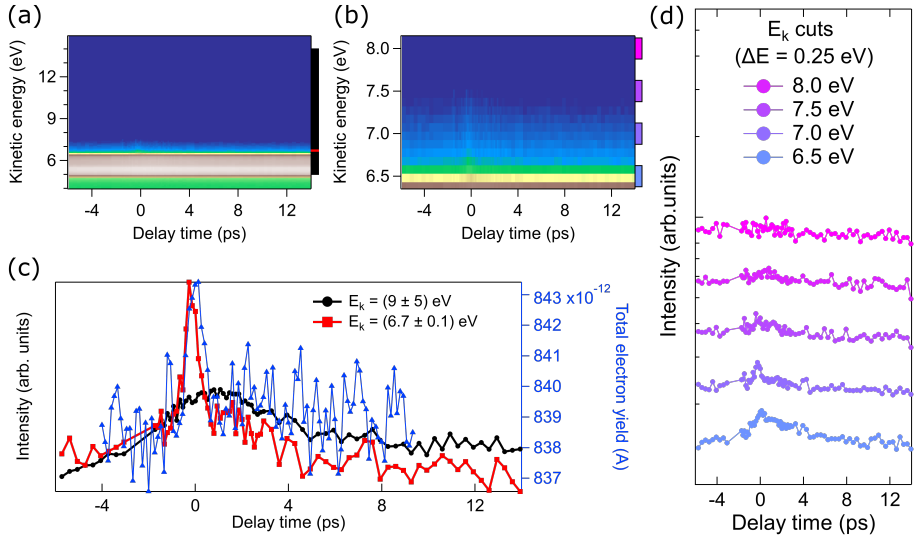

Figure 4.2: (a) Full-range delay line map and (b) zoomed-in delay line map on Fe(001)-p(1x1)O/MgO at 800 nm pump and 4.8 eV probe. (c) Delay line curves across the kinetic energy range indicated by the coloured labels in (a). (d) Delay line curves across the kinetic energy range indicated by the coloured labels in (b).

4.3 Light polarisation dependence

Physical phenomena at the electronic level can be concealed in photoemission by matrix element effects; one way in which they can manifest is by means of the incident light polarisation. The symmetry of the combination of electronic orbitals and mirror planes (which are fixed given a specific experimental geometry) and the polarisation of the probe beam may result in some transitions being allowed or forbidden.

For this reason, we performed measurements with linear vertical (LV) and linear horizontal (LH) HHG light as a probe, corresponding respectively to s-polarised and p-polarised light.

Data acquired with p-polarised probe are generally noisier, due to the fact that the change in polarisation takes place before the HHG process and in our setup the HHG intensity is roughly halved compared to an s-polarised light seeding.

In any case, we see that the temporal evolution of the two curves can be overlapped with a good degree of confidence, within the experimental sensitivity: we may therefore state that matrix elements effects are not significantly influencing the measurability of the electronic states that we are accessing.

4.4 Pump fluence assessment

Across all the pump fluences we measured, we are able to testify that single-photon excitation from the pump is still the dominant process.

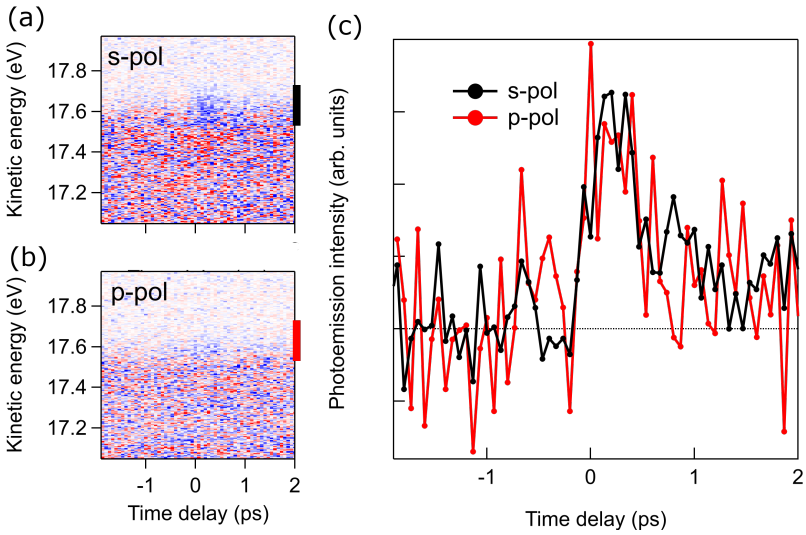

Figure 4.3: (a-b) Delay line maps acquired with LV and LH probe polarisations (corresponding to s-polarisation and p-polarisation respectively). (c) Delay line curves for s-polarised and p-polarised probe, integrated across the kinetic energy range indicated by the coloured labels in (a-b).

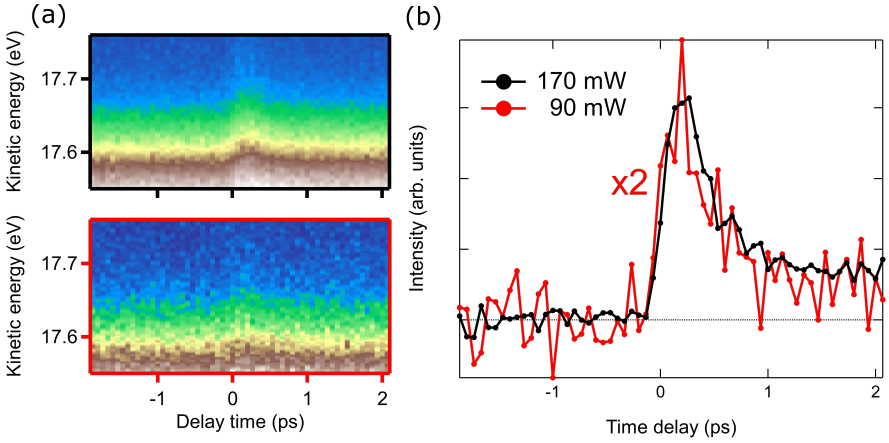

Figure 4.4: (a) Time delay maps on Fe(001)-p(1x1)O/MgO at 21.7 eV probe energy and 170 mW (*top*) or 90 mW (*bottom*) pump power. (b) Delay line curves integrated across the whole kinetic energy range of the maps in (a-b), indicated by the coloured borders.

As seen in fig. 4.4, within our experimental sensitivity halving the pump power results in half the photoemission intensity (provided that intensity vs delay curves are rescaled to their baseline). A build-up of some non-linear phenomenon would instead change this proportionality: in case of *e.g.* two-photon absorption dominating at higher fluences, a factor 4 would scale the intensity curve (Reutzel, A. Li and Petek, 2020).

In the case presented in fig. 4.4, the pump power is interchangeable with the fluence: the two measurements have been carried out in short order and without realigning the beamline. However, it is important to specify that the proportionality between laser power and fluence is hardly simple to assess. For example, the fluence depends on the dimension of the pump spot on the sample. In order to measure the spot shape and radius, we used a Ce-activated Yttrium Aluminum Garnet (YAG) crystal mounted just below the Fe(001)-p(1x1)O/MgO sample in the main chamber; by means of a non-invasive manipulator translation, our sample moves away from the beam path and is replaced by the YAG crystal.

YAG crystals are fast scintillators with excellent photoluminescence yields: if a photon is absorbed by the material, its energy is efficiently reemitted as visible radiation (peaking at 547 nm). In principle, we are thus able to estimate the shape and dimensions of the pump and probe beams and derive the fluence. Thanks to this method, we calculate that the fluence in our measurements spans the range from 0.5 mJ cm^{-2} to 1.5 mJ cm^{-2}.

However, there are two major factors hindering this procedure. (i), the YAG crystal does not have peak photoluminescence efficiency at the energy of the 800 nm pump. To verify that the image on YAG reproduces the true spot dimension and is not hindered by higher-order effects, we took camera pictures on both YAG and on Fe(001)-p(1x1)O/MgO , shown in fig. 4.5a-b. The spot of the pump on Fe is an effect of light diffusion from the irradiated surface, which is a linear effect: since the width of both peaks is compatible, we can be quite sure that the YAG crystal behaves linearly upon 800 nm pump irradiation. However, the shape of the spot is not uniform and displays photoemission hot-spots depending on the surface roughness: this makes the estimation of the FWHM, and consequently the calculation of the fluence, quite challenging. (ii) Across a long measurement with high statistics, small perturbations in the optical system due to *e.g.* heat load on some mirrors may move pump and/or probe beams one respect to the other, meaning that the spatial overlap is not optimal anymore: the area contributing to the signal is therefore just a portion of the pump spot.

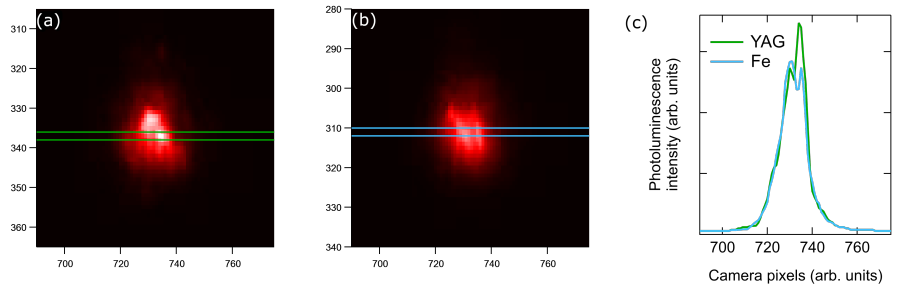

Figure 4.5: Camera pictures of the pump spot (a) on the YAG crystal and (b) on the Fe(001)-p(1x1)O/MgO sample. Coloured solid lines mark the stripes along which the images have been integrated; the horizontal cuts are shown in (c) with corresponding colours.

For these reasons, a fluence estimate of the pump signal based on the laser power

and the FWHM of the spot on the YAG would be misleading and would probably overestimate the actual fluence of the measurement. Using the laser power as a comparison between data is meaningful only when the experimental runs are relatively short and possibly not too far apart in time. Therefore, measurements like that in fig. 4.4 are well-grounded because the experimental conditions did not change much in the span of both measurements, whereas in general estimating the pump fluence is much less reliable.

We leave this question open for the moment, and we will deal with the matter in section 4.7 when discussing time-resolved measurements with the Mott detector, allowing us to indirectly assess this issue.

4.5 Pump energy dependence

The pump energy is another important parameter for the experiment. The pump has to be tuned to an energy high enough to excite electrons (typically in the optical range), but cannot be increased too much because conversely the threshold for pump photoemission decreases. The efficiency of the OPA in producing the required wavelength has to be taken into account as well.

Once spurious effects are excluded, the actual effect of changing the pump energy within the optical range should be to induce different transient states: the non-thermal electron distribution resulting from a laser pulse in the optical range could vary depending on the allowed or forbidden electronic transitions from the valence band to empty states.

In our experiment, we focused on two wavelengths, both in the visible range: 800 nm (1.55 eV) and 650 nm (1.92 eV).

4.5.1 Angular dependence

In case the final state of the electron excited by the pump pulse is a real state, the probability of the transition does not depend only on the energy of the initial state, but also on the momentum position, due to the k-dependence of electronic bands. In this case, some regions of the Brillouin zone above the Fermi level may be populated whereas others may not, depending on where in k-space the energy difference corresponds to the pump energy. Moreover, it is likely that non-thermal electrons thermalise to a thermal population with some angular dependency.

To verify this behaviour, we took angular-dependent delay line scans near and above the Fermi level and compared results between 650 nm and 800 nm.

With 650 nm pump energy measurements were acquired at normal emission and at 26° to compare two distinct Brillouin zone regions.

A slight dispersive feature may be found in the increased intensity at more positive angles in fig. 4.7f: we suppose that there are available states corresponding to that angular position.

On the other hand, the lack of any significant difference in the temporal shape of the curves at different angles, in both the energy regions we considered, leads us to believe that we are observing only the change of the electronic temperature resulting in a Fermi level broadening, i.e. we are measuring only thermal electrons.

With 800 nm pump energy, at normal emission the temporal behaviour near the Fermi level shows no angular dependence; furthermore, the lineshape of the delay curve shows a clear overlap with the measurement integrated in the same energy range at 650 nm (fig. 4.8). This means that the pump energy has negligible effect on the transient population of states above the Fermi level near the Γ point.

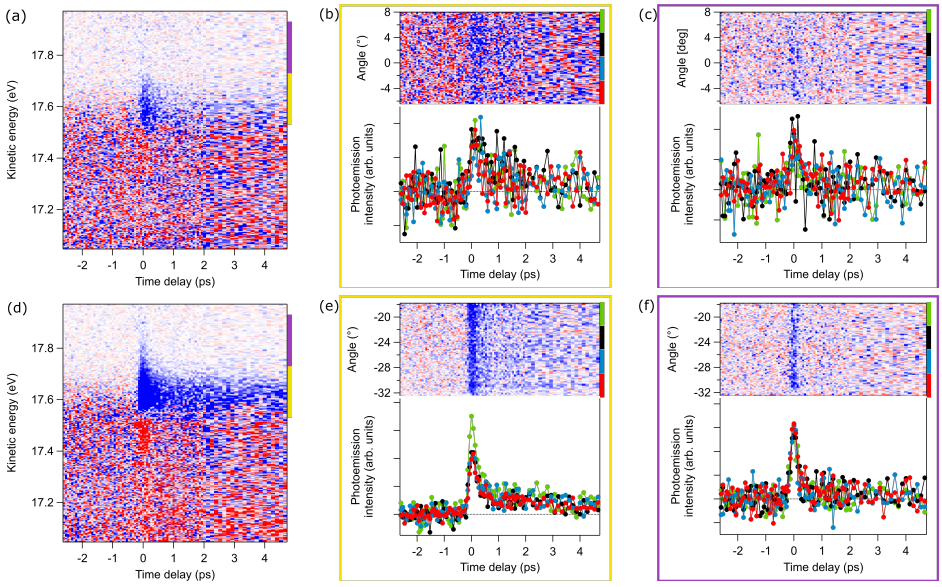

Figure 4.6: (a) Delay line maps acquired at 650 nm without angle resolution at normal emission. (b-c) Angle-resolved delay line maps integrated in the kinetic energy range from 17.55 eV to 17.75 eV (*yellow*) and from 17.75 eV to 17.95 eV (*purple*), as indicated by the coloured rectangles and the stripes in (a). (d-f) Same as (a-c), but at 26°.

On the other hand, the angular dependence is clearly visible at 26°. At 50°, the presence of an angular dispersion is even more evident; moreover, the rise time is different at different angles, as particularly evident in fig. 4.7i. The variation in the temporal shape may indeed be an indirect signature of non-thermal electrons scattering into the near-Fermi region, *i.e.* appearing at different delay times corresponding to different angles.

4.5.2 Non-thermal electrons

To get a further insight into this hypothesis, we probed a wider energy region above the Fermi level in order to evaluate the temporal behaviour as a function of the kinetic energy. As seen in fig. 4.9, the increase in photoemission intensity up to 18.4 eV kinetic energy cannot be explained by an increase in the electron temperature alone, as such a broadening of the Fermi step would result from a temperature increase of thousands of degrees. On the other hand, from the horizontal cuts in the bottom of fig. 4.9b we note that the higher the kinetic energy, the earlier the photoemission intensity rises as a consequence of the pump pulse. Furthermore, the lineshape of the peak is quasi-symmetric (approximable to a Gaussian) in case of the blue and black curves, whereas the red curve is more asymmetric and the green curve shows the typical slow time decay. We can thus infer that non-thermal electrons are excited to high kinetic energies, and then quickly decay into lower-lying, longer-living states.

The decay time from a non-thermal to a thermal population is generally agreed upon in literature to be in the timescale of a hundred of femtoseconds (Ferrini et al., 2009), which is lower than the temporal length of the laser pulse in our experimental setup. As a matter of fact, a Gaussian fit of the two cuts at highest kinetic energies (fig. 4.10) con-

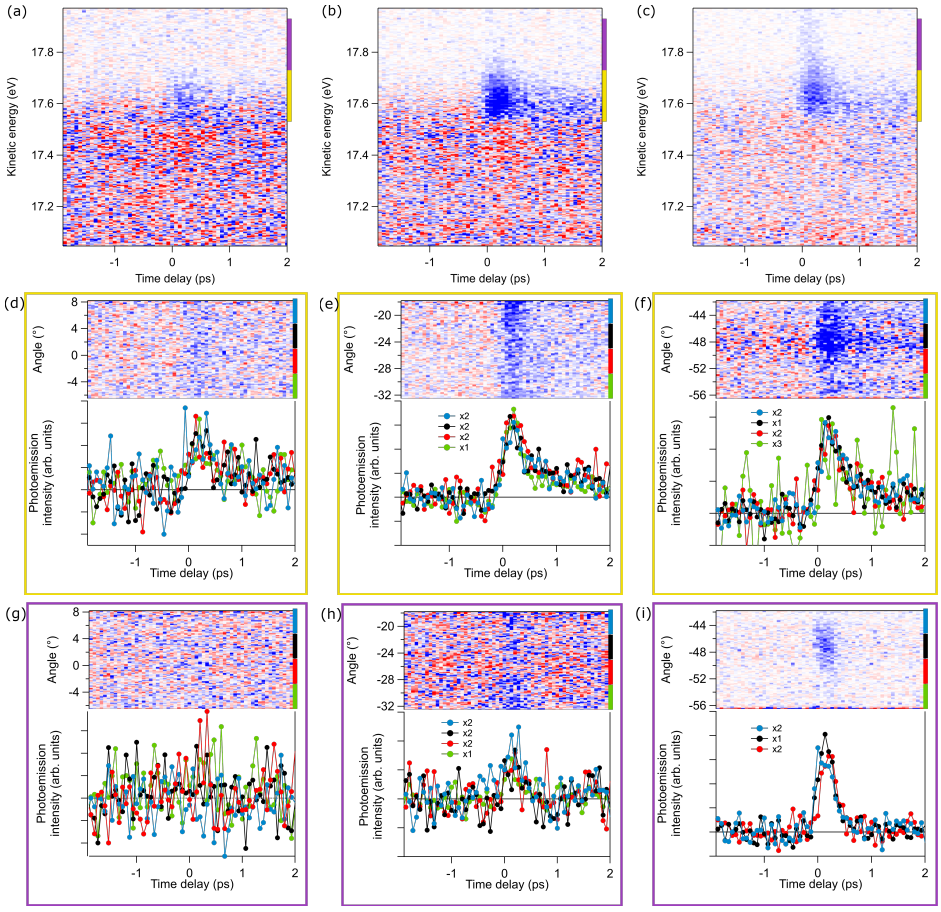

Figure 4.7: (a-c) Delay line maps acquired at 800 nm without angle resolution, at (a) normal emission, (b) 26° emission and (c) 50° emission. (d-i) Angle-resolved delay line maps integrated in the kinetic energy range from 17.55 eV to 17.75 eV (*yellow*) and from 17.75 eV to 17.95 eV (*purple*), as indicated by the coloured rectangles and the stripes in (a-c), at (d,g) normal emission, (e,h) 26° emission and (f,i) 50° emission.

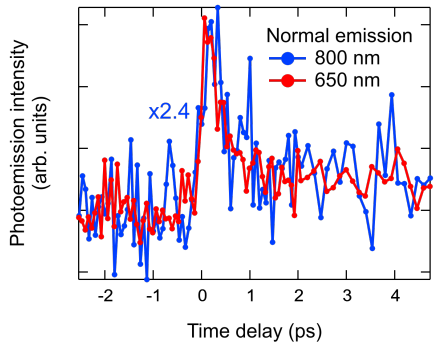

Figure 4.8: Delay line cuts, integrated in energy from 17.55 eV to 17.75 eV, acquired with 800 nm (1.55 eV) and 650 nm (1.92 eV) pump energy.

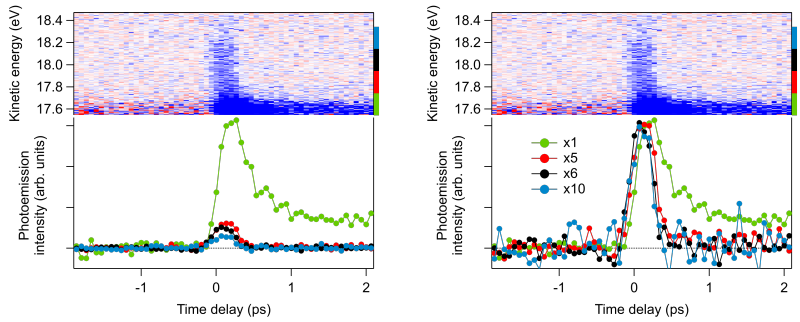

Figure 4.9: Delay line maps and corresponding spectra obtained by the integration of the energy regions labelled by the coloured stripes, (a) without any normalisation and (b) multiplied by an arbitrary factor to equalise the photoemission peaks.

firms that the curves are symmetric with a Gaussian width of ∼450 fs: this corresponds to a rise time of ∼200 fs, *i.e.* our temporal resolution.

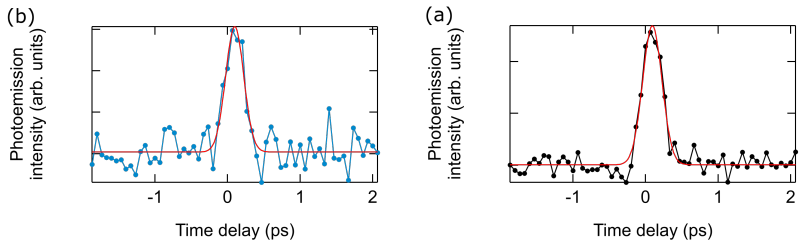

Figure 4.10: Delay line spectra corresponding to the (a) teal and (b) black energy integration regions in fig. 4.9a-b, fitted with a Gaussian.

This is also probably the reason why we do not see electrons beyond 18.3 eV binding energy: at these energies, electrons relax faster than what we can observe given our time resolution.

4.6 Ultrafast increase of the electronic temperature

We saw in the previous section that only specific angles reveal non-thermal electrons. On the other hand, thermal electron distributions can be described using Fermi-Dirac statistics: this is true for each pump-probe delay, *i.e.* the temporal evolution of the system can be modeled by a time-dependent Fermi-Dirac function.

This function can be retrieved by disentangling the thermal process from the spectral function of the band structure, as described by (Bühlmann et al., 2020): the authors perform the analysis for separate spin channels, but the principle is valid for the whole spin-integrated spectrum. The fitting procedure works as follows.

1. First we average the spectra at negative delays, to obtain an unperturbed spectrum at equilibrium. This spectrum is divided by the Fermi-Dirac distribution $f_{FD}(E; \mu_0, T_{e,0})$ with $T_{e,0} = 295\,K$, convoluted with a Gaussian to account for the pulse width. The result is the spectral function at equilibrium $A_0(E)$.

2. Secondly, we assume that the band structure and exchange splitting do not change following the pump excitation. This is reasonable, because our experiment is performed within the low fluence limit; even for Ni, whose Curie temperature is much lower compared to Fe, a fluence around $2.8\,mJ\,cm^{-2}$ is required for the exchange splitting to collapse (Tengdin et al., 2018) and ultrafast optical pulses affect collective excitations rather than the collapse in the the exchange splitting anyway (Carpene, Hedayat et al., 2015). If this is true, then the spectral function remains constant across all delays: $A(E, t) = A_0(E)$.

3. Upon the assumption in the previous point, we can divide our experimental spectra at any delay by the spectral function $A_0(E)$ and thus obtain the Fermi-Dirac distribution at that delay time.

4. Finally, the resulting data can be fitted so that band structure and spectral function do not play a role anymore.

The fitting function

$$f(E) = f_{FD}(E; \mu, T_e) \circledast \text{Gauss}(E, \mu) = \frac{1}{1 + e^{-(E-\mu)/k_B T_e}} \circledast \text{Gauss}(E, \mu) \tag{4.1}$$

leaves the chemical potential μ and the electronic temperature T_e as free parameters.

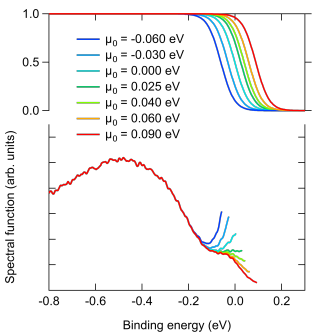

Figure 4.11: Fermi-Dirac steps (*top*) and spectral functions (*bottom*) at equilibrium as a function of the chemical potential choice.

The Fermi-Dirac distribution at equilibrium includes a 45 meV experimental energy resolution; however, the quantity with some degree of arbitrariety is the equilibrium chemical potential. As seen in fig. 4.11, the choice of the chemical potential influences the outcome of the spectral function calculation: unless we have specific expectations on the shape of $A_0(E)$ (or a simultaneous measurement of the Fermi edge on a gold polycrystalline film in the same experimental conditions) there is no obvious choice for μ_0.

We can give some *a posteriori* reasoning for the choice of a value of the chemical potential on the basis of the fit in eq. (4.1). In fig. 4.12 two fits, ran with $\mu_0 = 0$ meV and $\mu_0 = 0.090$ meV, have been highlighted; in the former case, most of the ultrafast effect can be explained as an increase of the electronic temperature, while in the latter the electronic temperature hardly shows any increase (more of a decrease, actually) and the chemical potential drastically changes.

In-between these two extreme cases there is a gradation of mixed effects, seen in fig. 4.12b. The fitting procedure is more reliable with lower $|\mu_0|$ values, as evident for example from the sizeable noise difference in fig. 4.12a. In general, fits follow experimental data more smoothly when a T_e increase is considered. However, we note that in case of a choice of μ_0 not too different from zero, *e.g.* the two green curves in fig. 4.12b, the chemical potential does display an ultrafast increase, and the electronic temperature behaviour is rather similar to the case with $\mu_0 = 0$ meV, so another choice of μ_0 in the range from 0 eV to 0.040 eV would not change significantly the estimation of the electronic temperature.

A minor change in the chemical potential would not be surprising anyway; it has been shown by (B. Y. Mueller et al., 2011) that a difference in chemical potential between up and down spin channels builds up after ultrafast excitation, and the following relaxation is driven by the equalisation of the two values in time. This study is beyond our scope in this section (as clearly we are interested in a spin-integrated quantity), but will come in handy in section 4.7.

In fig. 4.13 the result of the fitting procedure with $\mu_0 = 0$ meV, which agrees best with data, is displayed alone. The electronic temperature increases up to the range from 350 K to 360 K within 100 fs and then rapidly recovers to values similar to the initial ones. In this instance, the chemical potential shows a weak dependence on the delay time, but as we discussed in the previous paragraph this is not too worrying.

In the end, the relatively small change in the electronic temperature justifies the assumption we made above: no modifications in the band structure and in the exchange splitting take place.

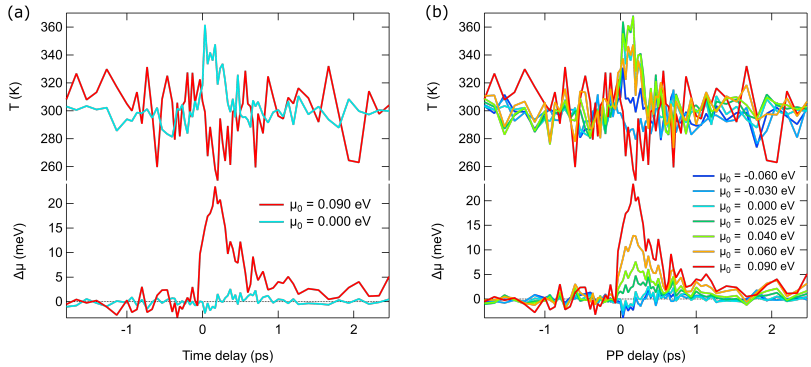

Figure 4.12: (a) Fit results for the calculation of the electronic temperature $T_e(t)$ and chemical potential $\mu(t)$ from time-resolved photoemission for two values of μ_0. (b) Same as (a), but for a wider range of μ_0 values.

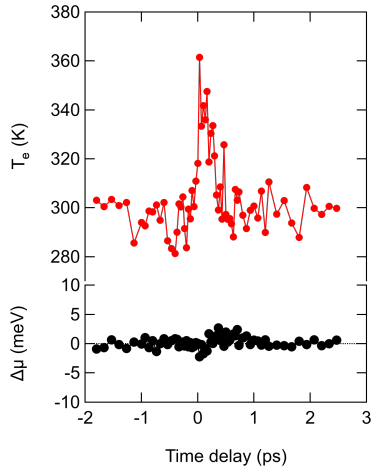

Figure 4.13: Fit results for the calculation of the electronic temperature $T_e(t)$ and chemical potential $\mu(t)$ from time-resolved photoemission for $\mu_0 = 0\,\text{eV}$.

4.7 Ultrafast magnetisation quenching

As anticipated in section 2.5, the SPRINT endstation is equipped with a double Mott detector for the measurement of the spin polarisation vector in all three spatial directions. The Mott detector works in total electron yield (TEY) mode and is optimised for multi-hit detection operation (Pincelli, Petrov et al., 2016): this is not quite as important when using continuous sources such as synchrotron light as it is for pulsed laser sources, photoemitting large numbers of electrons within hundreds of femtoseconds. When more than one electron per pulse reaches the Mott detector, a multi-hit operation mode is mandatory to correctly measure a spin polarisation signal.

In order to calculate the spin polarisation of the photoelectrons, the Mott detector acquires the total yield for each individual scattering channel (4 for each Mott detector setup); the sum of the count rates of the four detectors corresponds to the TEY. At the same time, the drain current from the sample can be measured: this constitutes an independent measurement of the TEY, to verify that the total yield condition is verified. Simultaneously measuring the TEY and the spin polarisation while performing a pump-probe experiment allows to monitor the behaviour of the electrons and their magnetic moment when subject to the pump pulse at the same time.

4.7.1 Effective fluence

We already saw in section 4.4 that the pump fluence estimate on the basis of the pump spot image is not representative of the actual fluence; we left the discussion pending, but we will show now that thanks to the simultaneous acquisition fo the TEY and the spin polarisation there is actually a way to estimate an "effective fluence".

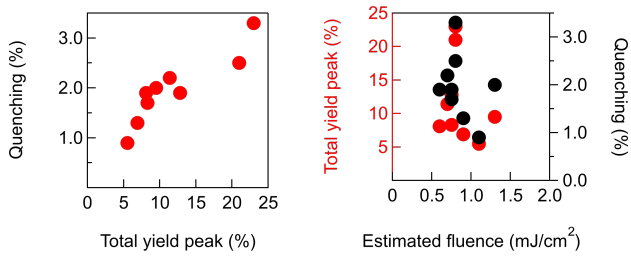

Figure 4.14: *Left*: quenching percentage as a function of TEY peak percentage increase across the whole dataset. *Right*: quenching percentage and TEY peak percentage as a function of the estimated pump laser fluence across the whole dataset.

Indeed, we know that the higher the fluence, the more electrons are pumped near the Fermi level and the more quenched the magnetisation becomes (Carpene, Mancini et al., 2008; Tengdin et al., 2018). If we consider different sets of measurements (so that several experimental conditions, *e.g.* the spatial overlap, the laser pointing or the heating of the optics, may be different), we estimate the fluence on the basis of the measurement of the pump spot dimension on the YAG, and we plot the maximum quenching of the spin polarisation and the TEY peak as a function of this estimated fluence (fig. 4.14a), we cannot see any trend. This result is predictable given the discussion in section 4.4. On the other hand, in fig. 4.14b we can see that the maximum quenching is monotonic with the TEY peak.

This observation again suggests that the calculated fluence is not a good parameter for the description of our measurements, whereas the TEY peak or the maximum quenching may represent an indirect estimation of the pump intensity, *i.e.* an effective fluence; this is not applicable in an absolute sense but it works when comparing two separate measurements.

In the following analysis of the ultrafast quenching of the spin polarisation, we will thus base our intensity rescaling on the TEY peak acquired together with that measurement.

4.7.2 Synchronous measurements of TEY and SP

The effect of the optical pumping is a transient decrease of the spin polarisation, which partly recovers within 1 ps but also shows a long-lasting tail. Figure 4.15 displays an example of the TEY and the spin polarisation curves, both shown as relative variations with respect to the unperturbed values, as a function of the time delay.

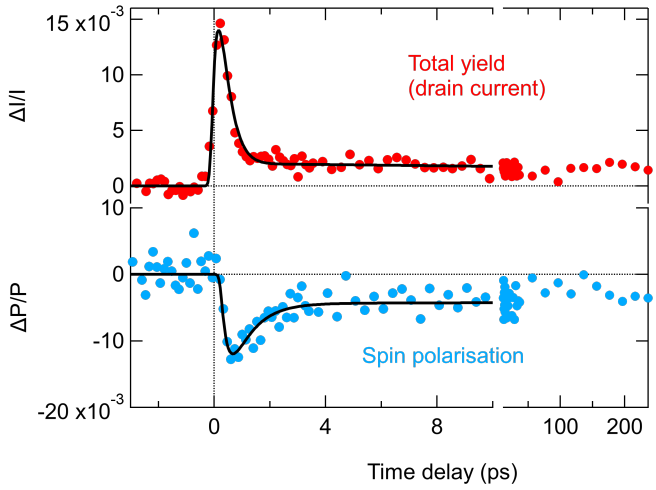

Figure 4.15: Example of TEY and spin polarisation curves as a function of the time delay, expressed as relative variation with respect to the unperturbed values (negative delays).

The two curves allow for a separate evaluation of the dynamics of the electronic and spin degrees of freedom after excitation, as we will see below. To this purpose, two phenomenological fitting routines have been used to describe the two systems in terms of their characteristic time constants. The fitting functions are based on the work of (Del Fatti et al., 2000), which garnered a good amount of success in this regard since several other works drew inspiration from it.

Electronic degree of freedom

In our fitting procedure, we described the electron dynamics found in the total yield as a product of two terms: the first contains an exponential rise with time constant τ_{therm}, to represent the thermalisation of electrons after the pump excitation, the second accounts

for the relaxation dynamics and is given by the sum of a fast (τ_{R1}) and a slow (τ_{R2}) exponential.

$$f_{TEY}(t, t_0) = \left\{ \left[N \left(1 - e^{-\frac{t-t_0}{\tau_{therm}}} \right) \left(e^{-\frac{t-t_0}{\tau_{R1}}} + N_{R2} e^{-\frac{t-t_0}{\tau_{R2}}} \right) \right] \Theta(t, t_0) \right\} \circledast G(t, t_0) \tag{4.2}$$

The presence of a peak in the TEY curve corresponding to the temporal overlap between pump and probe retrospectively affects the discussion in section 4.6. As a matter of fact, the TEY represents the photoemission quantum yield, and such an increase means that more electrons are being photoexcited as a consequence of the pump pulse. We may hypothesise that the chemical potential is indeed changing after the optical excitation, because the electronic temperature increase should in principle conserve the number of electrons near the Fermi level; the additional electrons revealed by the TEY would be therefore justified by a corresponding (tiny) ultrafast increase of μ.

One peculiarity we notice in this procedure is that, if the Gaussian width representing the laser pulse is fixed to the nominal value of $\sim$ 200 fs, the thermalisation time constant strongly increases with the effective fluence, as seen in fig. 4.16. The values for τ_{therm} range from 300 fs to 1500 fs; on the other hand, the fast relaxation time τ_{R1} is grouped in the range from 300 fs to 400 fs.

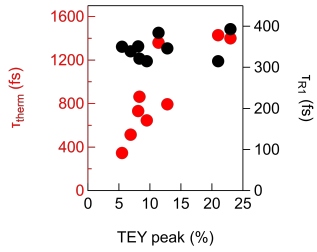

Figure 4.16: Calculated τ_{therm} and τ_{R1} as a function of the TEY peak percentage.

The latter result is fairly consistent, given also the small intensities and range of the employed laser power, whereas the former is a bit surprising: surely we would not expect a τ_{therm} higher than what has been found on Au or Ag, noble metals where a stronger screening due to bound electrons decreases the electron-electron scattering probability and thus the thermalisation of excited electrons takes longer (Del Fatti et al., 2000; Fann et al., 1992; Groeneveld, Sprik and Lagendijk, 1992; Sun et al., 1994). On the contrary, we may even argue for a *lower* thermalisation time constant ($\tau_{therm} < 500$ fs), for the exact same reason explained above.

We are still unsure of the reason why the thermalisation time changes so much: an instrumental issue seems the most likely explanation. It is challenging to argue for a truly physical significance of this result. However, one hypothesis we may be scrutinised is the fact that the probe photons are photoexciting extremely slow electrons, mostly in the range from 0.01 eV to 0.1 eV, well below the surface (in the order of magnitude of 10 nm): these electrons are in fact so slow that they may take a considerable amount of time to actually exit the sample after the pump excitation. A rough estimation yields a "travel time" throughout the solid in the order of $\sim$200 fs, or even more depending on the electron energy and on how many scattering events it may be subject to. Anyway, a more thorough study in this sense would require a systematic study on the electron escape depth with threshold photons, and is clearly beyond our scope at the moment.

Considering the trend of the TEY peak, one legitimate doubt would lead us to ask ourselves whether the TEY reflects a dynamics with the same behaviour of the electrons revealed with the hemispherical analyser, and if so, in which amount do the two correspond.

To this intent, we can compare time-resolved maps acquired with the hemispherical analyser at 4.8 eV at low fluence, in order to minimise space charge effects, with

TEY curves acquired with the Mott detector, as shown in fig. 4.17.[2] With proper intensity rescaling, the two curves perfectly overlap; this means that at low fluence the information provided by both measurement types is equivalent. Of course we need to keep in mind that at higher fluences the rise time τ_{therm} disproportionately increase in TEY measurements, and we cannot present a satisfactory explanation for this phenomenon, thus probably the best choice is considering data acquired at low fluence in the analysis in section 4.8.

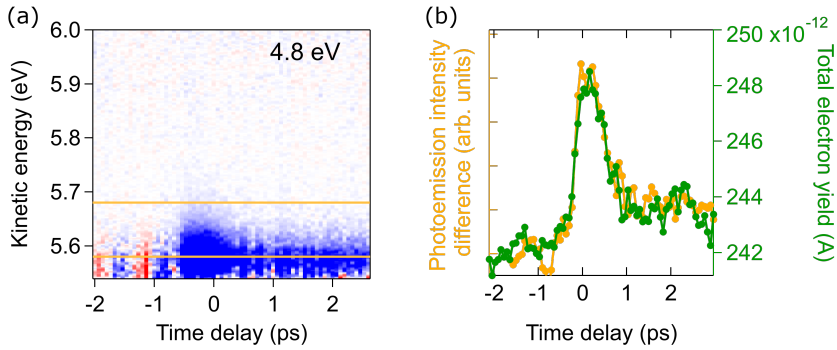

Figure 4.17: (a) Delay line map and on Fe(001)-p(1x1)O/MgO at 800 nm pump and 4.8 eV probe. (b) TEY curve (*green*) and delay line cut (*yellow*) across the kinetic energy range indicated by the yellow lines in (a).

Spin degree of freedom

Similarly to the previous section, we fitted experimental data with the phenomenological function

$$f_{SP}(t, t_0) = \left\{ \left[Q \left(1 - e^{-\frac{t-t_0}{\tau_Q}} \right) \left(e^{-\frac{t-t_0}{\tau'_{R1}}} + Q_{R2} e^{-\frac{t-t_0}{\tau'_{R2}}} \right) \right] \Theta(t, t_0) \right\} \circledast G(t, t_0), \tag{4.3}$$

where τ_Q is the magnetisation quenching time constant, τ'_{R1} is the "fast recovery" time constant and τ'_{R2} is the "slow recovery" time constant.

For the lowest effective fluence, τ_Q is comparable to our temporal resolution (τ_Q = 160 fs) and increases up to 600 fs; similarly, the fast recovery time ranges from 0.3 ps to 2.5 ps, increasing with the fluence. As already mentioned before, the magnitude of the quenching depends on the pump effective fluence as well. The long recovery time τ'_{R2} mirrors what happens for τ_{R2}: the partially demagnetised state survives for the whole investigated range (hundreds of picoseconds).

The trend of the ultrafast quenching, described by a sudden demagnetisation followed by a fast recovery and a much slower partially demagnetised state, agrees with previous works employing Magneto-Optical Kerr Effect (MOKE) on *3d* transition metals (E. Beaurepaire et al., 1996; Koopmans, Malinowski et al., 2010; Schellekens et al., 2013; Tengdin et al., 2018), and also specifically on Fe(001)/MgO(001) (Carpene, Mancini et al., 2008) or other substrates (Weber et al., 2011). In particular, authors of (Weber et al., 2011) find that in photoemission spectroscopy measurements both τ_Q and τ'_{R1} increase with the

[2] Keeping a low fluence is required because the electron analyser window saturates and runs the risk of damage if too many electrons impinge on the detector in a short amount of time.

relative quenching, which is the same phenomenon we notice in our data, exemplified in fig. 4.18.

We can note that τ'_{R1} is considerably longer than τ_{R1} as retrieved from the TEY curve, as well as following a considerably different trend as a function of the effective fluence. τ_{R1} is found in the range from 300 fs to 400 fs for all investigated fluences (fig. 4.16), whereas τ'_{R1} values are much more spread out. This may be a fingerprint that the two phenomena are uncorrelated, as we will discuss later.

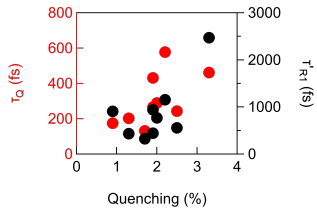

Figure 4.18: Calculated τ_Q and τ'_{R1} as a function of the quenching percentage.

In the framework of a phenomenological description of the sample under ultrafast excitation, first proposed by (E. Beaurepaire et al., 1996), we can estimate a "spin temperature", an analogous for the spin system to the electronic temperature we calculated in section 4.6. Given the relatively low fluences employed in our experiment, variations in the exchange interaction hardly take place; instead, we presume that the pump excitation induces thermal fluctuations in the spin degree of freedom after the heating of the electron system. On this hypothesis, the spin temperature T_s can be retrieved by exploiting the well-known dependence of the magnetic moment $m = m(t)$ on the temperature, in the mean field approximation - considering we are sufficiently far away from T_C, mean field theory should be applicable.

Since we are unable to measure the absolute value of m, we use the relative values with respect to the unperturbed magnetic moment m_0 (before pump excitation), of course assuming that the system relapses into the ground state inbetween two subsequent pulses. Hence we get

$$\frac{P(t)}{P_0} = \frac{m(t)}{m_0} = \left(\frac{T_C - T_s(t)}{T_C - T_{s,0}}\right)^{\frac{1}{2}}, \tag{4.4}$$

where P(t) is the transient spin polarisation measured in our experiment and P_0 is the static polarisation (at negative time delays). The inverse formula reads

$$T_s(t) = T_C - (T_C - T_{s,0})\left(\frac{P(t)}{P_0}\right)^2. \tag{4.5}$$

Using the values $T_{s,0} = 295\,K$ and $T_C = 1043\,K$, the Curie temperature of bulk Fe, the spin temperature trend is displayed in fig. 4.19.

4.7.3 Other influences on the magnetisation dynamics

In light of the results displayed in the previous sections, it is legitimate to ask whether the measured trend of the spin polarisation truly represents an ultrafast quenching of the magnetic moment, or other effects are in play. In general, the explanation that garnered the most widespread acclaim has been exposed by (E. Beaurepaire et al., 1996): in the timescale of picoseconds, the energy is transferred to other thermal baths, in particular to the spin system, resulting in an ultrafast quenching.

However, in our case a direct measurement of the electron spin polarisation, rather than a MOKE measurement as in (E. Beaurepaire et al., 1996), opens up other questions: the discussion on this matter has been dividing the scientific community for more than two decades by the time of this thesis. For this reason, we will review the more common

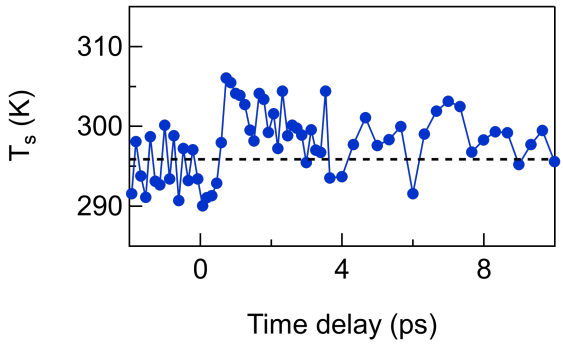

Figure 4.19: Spin temperature $T_s(t)$ as a function of the time delay.

effects (unrelated to the quenching of the magnetic moments) affecting spin polarisation measurements.

Polarised carriers redistribution

First of all, in a time, energy and spin-resolved photoemission study on Co/Cu(001) (Eich et al., 2017), authors attribute the ultrafast modification of the spin polarisation near the Fermi level to hot carriers redistribution within the photon energy of the pump, due to (spin-conserving) optical transitions into empty states. This result has been corroborated by the work of (Bühlmann et al., 2020) on a Fe/W(111) film.

However, we can safely assume that in our experiment this is not the case. The line of reasoning applied by (Eich et al., 2017) relies on the similarity in the trends of the hot electrons and the spin polarisation at low binding energies, as opposed to the trend of the spin polarisation at high binding energies. In our case, we know that the time constants describing the relaxation of the TEY (τ_{R1}) and the spin polarisation (τ'_{R1}) are completely different. As the TEY is related to the redistribution of electrons after the excitation, state-filling contributions to the spin polarisation are totally irrealistic: their effect would disappear with a characteristic time constant compatible with τ_{R1}.

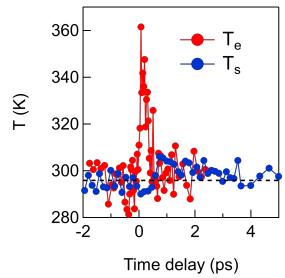

Figure 4.20: Electronic temperature T_e and spin temperature T_s as a function of the time delay. The black dashed line marks the equilibrium temperature T = 296 K.

On top of this, our phenomenological fits retrieved two quantities, the electronic temperature T_e and the spin temperature T_s. The two are independent, since they have been retrieved from measurements with HHG and 4.8 eV respectively, yet when we juxtapose two measurements at comparable effective fluence (fig. 4.20) we see that (i) there is a delay between the two excitations, and (ii) when the electron system relaxes, the spin temperature increases, before decaying at longer delays in the neighbourhood of the electronic temperature - seemingly reaching the long-lasting metastable state.[3]

[3]Since the two measurements are independent, it would be a legitimate question to ask how the time delay scale has been aligned. We determined the relative scale of the two measurements on the basis of the position of the zero of the time delay scale as retrieved from fitting the TEY peak, which directly relates to the spin

We may also find a proof by contradiction as follows. If we suppose that an ultrafast redistribution of electrons is driving the decrease of the spin polarisation we measure, it would mean that not only the electronic temperature, but also the chemical potential is changing as a result of the laser excitation: the increase in the chemical potential would be directly linked to the decrease in the spin polarisation. We would then refer to section 4.6 and change our evaluation of μ_0 with a value in line with this consideration: for instance, $\mu_0 = 0.025\,\text{meV}$.[4] If we overlap the calculated spin temperature $T_s = T_s(t)$ and the chemical potential $\Delta\mu = \Delta\mu(t)$, as done in fig. 4.21, we can see that (i) again we find a delay between the two excitations (fig. 4.21a), and (ii) the relaxation follows clearly different timescales (emphasised in fig. 4.21b).

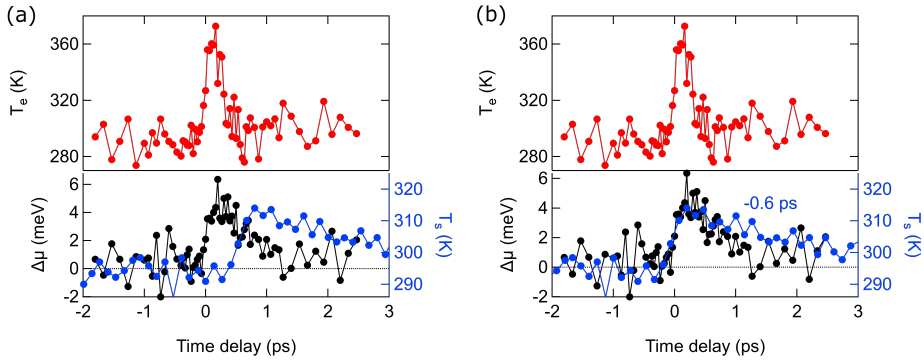

Figure 4.21: Electronic temperature $T_e(t)$, variation of chemical potential $\Delta\mu(t)$ and spin temperature $T_s(t)$ as a function of the time delay. T_s is correctly scaled with the delay in (a), and is artificially shifted by 0.6 ps in (b) to ease the comparison between temporal trends with $\Delta\mu(t)$.

Superdiffusive spin currents

Another issue that may influence the outcome of the spin polarisation is the presence of superdiffusive spin currents that may result in accumulation of a certain degree of polarisation at the surface. An alternative means of explaining ultrafast magnetisation dynamics data has been proposed by (Battiato, Carva and Oppeneer, 2010): superdiffusive spin currents generated by the pump pulse may result in an apparent decrease of the spin polarization measured by the probe pulse, due to majority electrons drifting away from the probed region more easily than minority electrons. Anyway, we argue that our experiment drastically decreases the chance that superdiffusive spin currents relevantly contribute to the ultrafast demagnetisation.

First of all, we already explained in the previous chapter that a threshold photon results in very low-energy primary photoelectrons, in the order of 0.1 eV, which have a large mean free path. The probing depth of our 4.8 eV photon threshold measurements can be estimated as several nanometres. For this reason, spin-dependent mean free paths, which heavily affect any measurement of spin polarisation of secondary electrons (Penn, Apell and Girvin, 1985; Sirotti, G. Panaccione and Rossi, 1994), only marginally affect our

polarisation because the two are measured simultaneously.

[4] The exact choice of μ_0 is not important for this proof, because the electronic temperature does not change much and *any* increase in the chemical potential we find by means of our fitting procedure follows the same temporal trend, and the relevant consideration is taking a μ_0 that shows a dependence with the delay time.

discussion: our signal is constituted mostly of primary photoelectrons and their inelastic mean free path is much longer compared to inelastic electrons, thus our depth sensitivity is high enough to photoemit both spins.

A superdiffusive spin current needs to propagate via a suitable medium. Indeed, several studies (Eich et al., 2017; Mathias et al., 2013; Wieczorek et al., 2015) showed that within the first 100 fs spin currents dominate over Elliott-Yafet-type spin scattering in *3d* transition metals grown on a spin-conducting substrate. Since our Fe(001)-p(1x1)O/MgO system is composed of an insulating substrate, we would not expect a relevant spin current through MgO (Turgut, La-o-vorakiat et al., 2013); the Ta stripes would then be the medium of propagation of the spin current. However, Ta is a strong spin scatterer (Turgut, La-o-vorakiat et al., 2013): when considering the pump-probe signal affecting the TEY as measured by the drain current, we would probably see a higher degree of quenching on the measured spin polarisation due to superdiffusive spin currents in Ta completely dominating any spin-flip phenomenon.

Lastly, the demagnetisation characteristic times we observe are all greater than 150 fs, which actually suggests spin-flip events driving the decrease in the magnetic moment, as argued by (Turgut, Zusin et al., 2016); spin currents would influence the signal on much shorter timescales.

Pump photons contributions

A concern that arose in the past has been the fact that possible non-thermal contributions to the demagnetisation process may originate from photons themselves, via angular momentum transfer or spin-flip enhancement. Although the number of photons in our experiment is too small to give rise to such effects (Koopmans, Kampen et al., 2000), in (G. P. Zhang and Hübner, 2000) an argument has been made to include the action of SOC and the interaction between spins and photons in ultrafast demagnetisation processes.

On this matter, we may firstly consider that our measurements did not involve circularly polarised light; in any case, we may be reasonably sure that direct angular momentum transfer from photons to electrons has been demonstrated to give negligible contribution to the demagnetisation in (Dalla Longa et al., 2007). Therefore, we would expect no effect on the dynamics of the spin polarisation due to the pump photon polarisation.

Longer delays

Even if in the discussion we focused on the first few picoseconds of the phenomenon, we tried acquiring data at much longer timescales. We were able to confirm that the "tail" lasts for hundreds of picoseconds both in the TEY and in the spin polarisation measurements. This long-lasting effect is generally attributed to a slow thermal relaxation rate, *i.e.* heat diffusion outside the irradiated spot: the behaviour is then dictated by the phonon dynamics, dominating at longer delays.

Low-energy phonons are surely important for demagnetisation because of the spin rate proportionality to the phonon energy ($\dot{S} \propto E_p^{-1}$), whereas higher-energy phonons contribute to the energy exchange between the electron and lattice systems ($g_{ep} \propto E_p$) (Koopmans, Malinowski et al., 2010). We do not have direct access to a measurement of the phonons, so we limit our discussion to the fast timescale of the picoseconds without delving into the long delays any further.

4.8 Three-temperature model and application

In section 4.6 we have seen that we can derive the evolution of the electronic temperature from the (thermal) Fermi-Dirac distribution, as extracted from valence band EDCs acquired with HHG photons; in section 4.7 we showed the ultrafast quenching of the spin polarisation, measured with threshold photons of $h\nu = 4.8\,eV$ by means of the energy-integrated Mott detector. These measurements exploit the same physical process (photoemission) but assess two completely different quantities (electronic temperature vs electron spin polarisation) by making use of different photons and setups: they are essentially independent measurements. Yet, their results can be related to a single microscopic model that we will showcase in this section: the *microscopic three-temperature model* (M3TM).

First introduced in (E. Beaurepaire et al., 1996), as we explained in the overview at the beginning of the chapter, the three-temperature model is expressed as a set of three coupled differential equations. Each of those separately treats electrons, lattice and spins as separate systems and describes the dynamics of the electronic temperature T_e, the phonon temperature T_p and the spin temperature T_s. This phenomenological model can be improved to include a microscopic description of the system: the major difference is the replacement of the spin temperature with the ultrafast magnetisation dynamics. As a matter of fact, to analyse our data we used the aforementioned M3TM proposed by (Koopmans, Malinowski et al., 2010), with some minor modifications. This procedure represents a further step in order to link our data and the phenomenological fits we performed previously to microscopic parameters representing true physical quantities.

$$\frac{dT_e}{dt} = \frac{P}{\gamma_e T_e}\frac{1}{\pi\sigma^2}e^{(t-t_0)^2/\sigma^2} - \frac{g_{ep}}{\gamma_e T_e}(T_e - T_p) \tag{4.6}$$

$$\frac{dT_p}{dt} = -\frac{g_{ep}}{C_p}(T_p - T_e) - \frac{k}{C_p}(T_p - T_{room}) \tag{4.7}$$

$$\frac{dm}{dt} = Rm\frac{T_p}{T_C}\left(1 - m\coth\frac{mT_C}{T_e}\right) \tag{4.8}$$

For simplicity, we modeled the laser pulse as an instantaneous heating term P, providing an amount of energy density with a Gaussian profile, centred around t_0, instead of considering a realistic heat diffusion in the material.

The lattice specific heat C_p is assumed to be independent of T; in any case, in our experiments the temperature variations are quite small and the specific heat does not change appreciably in this temperature range (White and Minges, 1997). We approximate the electronic specific heat C_e as proportional to the electronic temperature: $C_e = \gamma_e T_e$. By constraining the electronic specific heat at 300 K to be equal to its literature value, we used $\gamma_e = 0.7079\,mJ/cm^3K^2$ (Blackburn, Kaufman and Cohen, 1965; Hofmann et al., 1956; Kaufman, Clougherty and Weiss, 1963).

The thermal leak is taken care of by considering our system in contact with a heat sink, in the limit of infinite heat capacity, thus adding a heat loss parameter to the differential equation 4.7.

Lastly, according to (Koopmans, Malinowski et al., 2010), the magnetisation scaling factor R is equal to

$$R = \frac{8a_{sf}g_{ep}k_B T_C^2 V_{at}}{(\mu_{at}/\mu_B)E_D^2}, \tag{4.9}$$

where V_{at} is the atomic volume, k_B the Boltzmann constant and E_D the Debye energy.

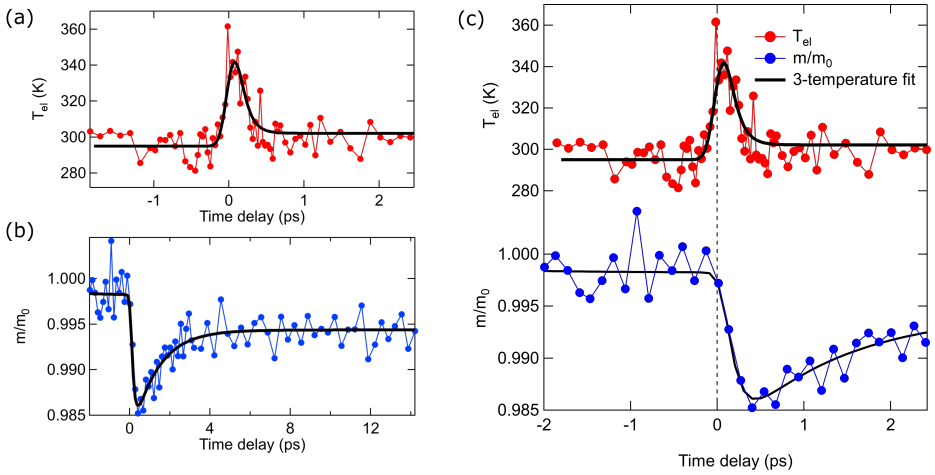

Figure 4.22: Examples of three-temperature model-based fits of different sets of experimental data: (a) electronic temperature T_e and (b) spin polarisation. (c) Both curves displayed in the same graph, with the time zero overlap t_0 highlighted by the dashed line.

It is clear now that the measurements of electronic temperature in section 4.6 and of spin polarisation in section 4.7 can be related to equations 4.6 and 4.8, respectively. Fitting our data would yield an evaluation of the electron-phonon coupling g_{ep} and of the magnetisation scaling factor R, ultimately leading to the estimation of the spin-flip probability a_{sf}.

An example of the curves resulting from the fitting procedure of both datasets can be found in fig. 4.22.

Parameters	g_{ep} (EJ(sm^{3}K)$^{-1}$)	R (ps^{-1})	a_{sf} (arb. units)
	1.8(2)	2.7(4)	0.103(16)

Table 4.1: Electron-phonon coupling constant g_{ep} and magnetisation scaling factor R resulting from the M3TM fitting procedure. The last column is the extracted spin-flip probability according to eq. (4.9).

Fitting values of g_{ep} and R are shown in table 4.1, as well as the spin-flip probability a_{sf} derived from eq. (4.9), averaged over different pump fluences. The fit yields a spin-flip probability of $a_{sf} = 0.103(16)$. This value may seem high at first glance, because it means that roughly one in ten scattering events leads to a spin-flip; nevertheless, it is in line with the values extracted in (Koopmans, Malinowski et al., 2010) for Ni and Co ($a_{sf,Ni} = 0.185(15)$, $a_{sf,Co} = 0.150(15)$), and it is closer to Co than it is to Ni as we would expect. Indeed, the authors argue that, although a_{sf} scales with Z^4 and a value of ~ 0.001 has been found for Cu, another *3d* metal (Beuneu and Monod, 1978), an enhanced spin mixing due to band crossings near the Fermi energy may increase the spin-flip probability by orders of magnitude.

Our results show an excellent agreement between fits of electronic temperature and spin polarisation curves; furthermore, as already mentioned, the extracted parameters

are compatible between measurements at different effective fluences. The intensity scaling factor given by the TEY curves reproduces well the proportionality between energy density parameters included in the fit, further confirming the robustness of our phenomenological evaluation of the pump fluence.

Interestingly, the magnetisation scaling factor R is considerably smaller (by an order of magnitude) compared to the results on Ni and Co. This is probably due to the lower atomic density, a higher Debye energy (around 0.04 eV) and a higher atomic magnetic moment ($\mu_{at}/\mu_B = 2.22$) all contributing to decrease the demagnetisation rate.

By using the value of g_{ep} extracted by the fit we can calculate the ratio g_{ep}/γ_e, which gives an estimation of the rate for energy exchange between the electrons and lattice systems. Our calculation yields $g_{ep}/\gamma_e = 2.5\,\mathrm{K\,fs^{-1}}$, which is in line with expectations - for most metals this ratio is in the order of magnitude of $1\,\mathrm{K\,fs^{-1}}$ (Ferrini et al., 2009). Considering that our experiment does not drive the system strongly out of equilibrium and the electronic temperature variation is relatively small, we conclude that we do not have access to the time resolution required for truly appreciating this energy transfer.

We noted in the previous sections how there is a delay between the rise of TEY and spin polarisation curves: this is true across all of our datasets. The M3TM correctly and naturally reproduces this behaviour: it is intrinsic in the microscopic model that the ultrafast quenching of the magnetic moment is delayed with respect to the initial excitation of the electronic system.

The successful application of the microscopic three-temperature model to our data testifies that the physical process behind the ultrafast change in spin polarisation is completely explainable in the context of a spin-flip dominated system, without resorting to near-Fermi carriers redistribution or superdiffusive spin currents.

4.9 Conclusions

In previous sections, we presented complementary measurements of time-resolved photoemission spectroscopy and polarimetry on Fe(001)-p(1x1)O/MgO aimed at giving insight into the ultrafast excitation of the electronic and spin subsystems and the subsequent deexcitation channels. We may summarise the main results as follows:

1. the ultrashort pump pulse excites the electron heat reservoir to a non-thermal state (at the limit of our temporal resolution), which then by electron-electron scattering bounces back to a thermally heated state;

2. the spin heat reservoir is subject of an angular momentum transfer from the heated electron system: in essence, the pump pulse functions as a thermal trigger of the quenching of the spin polarisation, and a threshold probe is sensitive exactly to this dynamics;

3. other phenomena associated with an effective change of the measured spin polarisation, like spin redistribution in excited states, are proven to be negligible: our experiment is thus an expression of a pure "thermal trigger" of the angular momentum transfer inducing a reduction of the spontaneous magnetic moment.

By means of direct measurements of the electron temperature and ultrafast magnetic moment quenching, we were able to conclude that the ultrafast decrease of the threshold spin polarisation in Fe(001)-p(1x1)O/MgO is driven by Elliott-Yafet-type spin-flip scattering, induced by the initial heating of the electrons and the energy transfer to the spin. Using the M3TM we succeeded in completely explaining the phenomenology

we revealed within a single theoretical model, and we derived the spin-flip probability $a_{sf} = 0.103(16)$.

Our experiment has been carried out at low fluences: this has proven to be an advantage, in two ways. First, by using low fluences we did not drive the system in a state too far from equilibrium, which reduced the amount of non-thermal transients before thermal phenomena set in; secondly, small variations of the spin polarisation due to low fluences are hardly compatible with spin currents, which tend to have a much greater effect on the detected spins.

Ultimately, our results unambiguously trace the change in spin polarisation as a true angular momentum transfer to the spin magnetic moments, and like the other ultrafast experiments discussed and cited in this part belong to the category making use of a thermal trigger: the laser pulse delivers energy to the electronic reservoir and a three-heat-reservoir model accounts for the energy distribution to the lattice and spin degrees of freedom.

An angular momentum transfer may also pass through other channels: "non-thermal triggers" of photonic or phononic origin do not deposit heat but act on spin magnetic moments through coherence. Photonic triggers like Impulsive Stimulated Raman Scattering can produce a mixed spin excited state whose decay may result in a different final spin (Kirilyuk, Kimel and Rasing, 2010); on the other hand, phonons may act as ultrafast triggers of the magnetisation via transient distortions inducing magnetic phase transitions (Afanasiev et al., 2021; A. Disa et al., 2020; Fechner et al., 2018).

Combining both thermal and non-thermal triggers would complement our experiment by supplying the access to the phononic system; the manipulation of the three degrees of freedom may provide new insight and understanding of the magnetisation dynamics and the channels of angular momentum transfer, also in more complex systems.

Part II

Layered magnetism as a source of topology

CHAPTER 5

$EuSn_2P_2$: a candidate axion insulator

> Why did you even come to the UK to measure Europium?
>
> G. Maugeri, 2019

5.1 Overview

A purely 3D magnetic order, occurring for instance in Fe as we saw in the previous part, is in its very essence a quantistic phenomenon where *3d* electrons with large densities close to the Fermi surface give rise to an exchange interaction and a band splitting. An Fe crystal at ambient conditions is the epitome of the *itinerant* model of magnetism, where *3d* electrons contributing to magnetism are partially delocalised and distributed in the whole unit cell. Both of these aspects, the 3D nature of the lattice (and its influence on magnetism) and the delocalised electron-electron interactions, have been challenged in the synthetisation of several compounds for novel functionalisations.

First of all, there is an interest in making use of *4f*-based elements, for which the reference is the *localised* model of magnetism (Jensen and Mackintosh, 1991), considering magnetic states as mainly concentrated on specific centres and interacting rather weakly with electrons from other shells. Combining lanthanides with other non-magnetic atomic species in layered structures further contributes to the profound change in the physics of magnetism in these compounds. Compared to 3D materials with isotropic bonding, highly anisotropic crystals, where atoms are strongly bonded in two-dimensional planes but the interlayer coupling is weak, have been harnessed as a way to tune and control magnetic behaviour. Without having to resort to true 2D structures, electronic states become partially confined: this has been used to great effect to induce non-trivial states of matter. With these premises (and the caveat that only basic concepts will be treated here), we enter the realm of topology.

The class of *topological insulators* at present encompasses a vast number of materials sharing the same peculiarity: that of being bulk insulators and surface conductors. The gap between valence and conduction band is closed at the interface of the crystal, *i.e.* its surface, thanks to the non-trivial topology. The electronic states crossing the Fermi level at the surface are intrinsically robust and are considered topologically protected. In the simplest picture of a strong topological insulator, valence and conduction bands are connected by a pair of linearly dispersing cones ("Dirac cones") merging at their vertex ("Dirac point"). It is also required that states at opposite momentum have opposite spin, and thus the spin has to rotate with k in isoenergetic cuts; this has implications

also on the transport properties, because the surface current is spin-polarised. A cartoon representation of the key properties of topological insulators can be found in fig. 5.1.

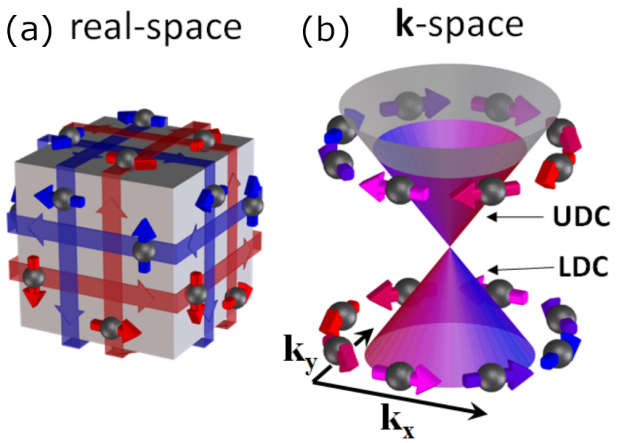

Figure 5.1: (a) Real space representation of the spin-polarised surface conductivity of a topological insulator. (b) Model of the reciprocal space topological bands connecting valence and conduction bands in a topological insulator: the two Dirac cones host electrons with defined spin polarisation, whose direction is highlighted by the colour code from blue to red. Adapted from (Jozwiak, Y. L. Chen et al., 2011).

As mentioned before, these are general considerations on the aspects of the topological insulator physics that prove relevant for the experiments outlined in this chapter. The interested reader may find more complete and thorough information in the reviews by (Ando, 2013; Hasan and Kane, 2010) or the book by (S. Shen, 2017). On top of this, an alternative and fascinating view on topological insulators states that this class is defined by being bulk magnetoelectrics, rather than surface conductors. An elegant and thoughtful treatment of this matter can be found in (Armitage and L. Wu, 2019).

When dealing with magnetism and topological states, a key role is played by one of the very fundamental processes that to our understanding governs a plethora of distinct phenomena in physics: symmetry breaking. Spontaneously broken symmetries are more than just mathematical artifices to deal with the phenomenology of phase transitions, as Lev Landau foresaw starting from 1937; they intrinsically shape the behaviour of the system via the appearance of order parameters, and are an important part of the definition of universality classes and their application via the renormalisation group.

Ferromagnetic order is a traditional example of a spontaneous symmetry breaking, more specifically time-reversal symmetry (TRS) breaking. TRS breaking relates with topological insulators in a unique way: indeed, topological surface states are protected by TRS. The interplay between magnetism and topology would not only open a gap in the topological states, but also lead to the realisation of the quantum anomalous Hall (QAH) effect and the topological magnetoelectric effect (TME) (Essin, Moore and Vanderbilt, 2009; G. Xu et al., 2011; Yu, W. Zhang et al., 2010). The postulation of a new quantum state - the axion insulator, named after its equivalent in high-energy particle physics - predicted quantised TME effects in such a material (Armitage and L. Wu, 2019; Varnava and Vanderbilt, 2018). All things considered, it comes to no surprise that synthesising a magnetic topological insulator showing axion physics has been sought after for quite

some time.

In the quest for creating such a material, the first approaches have been focusing on chemical doping of a topological insulator with magnetic species (Chang et al., 2013), or the exploitation of heterostructures where magnetic layers induce proximity effects on nonmagnetic topological insulators (Hou and R. Wu, 2019). In both cases, optimising and controlling the interplay between topology and magnetism has proven a daunting task. Therefore, it was not until the synthesis of stoichiometric compounds, in particular antiferromagnetic topological insulators (AFI) (Mong, Essin and Moore, 2010a) that the axion insulator state was in reach.

Experimental efforts have been focusing on tetradymite-type ternary chalcogenides, and in particular $MnBi_2Te_4$ (Y. J. Chen et al., 2019a; J. Li et al., 2019; Otrokov et al., 2019). However, the entanglement between the magnetic properties arising from Mn *3d* electrons and the topology of the Bi and Te *p* shells renders difficult to analyse and quantify their interplay. This is the reason why *4f* lanthanide-based compounds such as $EuSn_2As_2$, $EuIn_2As_2$ and $EuSn_2P_2$ (Arguilla et al., 2017; H.-C. Chen et al., 2020; H. Li et al., 2019; Sato et al., 2020) have been spearheading the progress in this field. Anyway, a complete characterisation of electronic states and their role in the interaction between magnetic order and topological protection of surface states is, to the best of our knowledge, absent.

This reason justifies the investigation of one of the compounds in this family, $EuSn_2P_2$, by means of the powerful tools available to state-of-the-art spectroscopy beamlines.

Part of the experimental results described in this chapter have been published in (Pierantozzi et al., 2022). What is presented in that paper is the accomplishment of a work initiated by G.M. Pierantozzi, to which we contributed equally.

5.1.1 Crystalline structure and phase transitions

When designing an antiferromagnetic topological insulator, there are powerful chemical criteria to tune the desired properties (Gui et al., 2019):

- low-dimensional structures are required for electronic orbitals confinement, a key ingredient in quantum materials;
- *5p*-based elements with moderate electronegativity provide chemical flexibility and versatility for quantum states, thanks to the sought-after strong spin-orbit coupling that contributes to the origin of topology;
- a clever placement of magnetic lanthanides in the unit cell results in magnetic order without entanglement with other electronic states.

These design rules have been applied to synthesise $EuSn_2P_2$, where Eu and Sn fulfil the third and second criteria, respectively, and its crystalline structure chracterised by weak van der Waals bonds between layers satisfies the first criterion.

$EuSn_2P_2$ has a rhombohedral structure, in which Eu atoms and the Sn-P network form hexagonal layers and stack along the *c* direction; the resulting lattice is centrosymmetric and belongs to the space group $R\bar{3}m$. Each Eu layer, separated by the $Sn@P_3$ triangular pyramids, is roughly 9 Å distant from the next one. A scheme of the crystal structure and the Brillouin zone is shown in fig. 5.2.

Field-dependent magnetisation and neutron diffraction measurements proved that $EuSn_2P_2$ undergoes a paramagnetic-antiferromagnetic transition at the Néel temperature $T_N \sim 30\,K$ (Gui et al., 2019). Ferromagnetic ordering occurs within the *ab*-plane

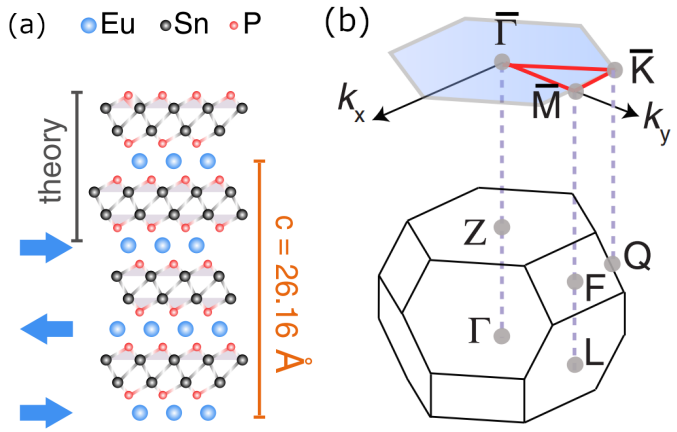

Figure 5.2: (a) Hard sphere representation of the crystalline and magnetic structure of $EuSn_2P_2$. A-type antiferromagnetic alignment of spins in Eu layers is highlighted by the blue arrows. The orange line marks the extension of the vertical axis of the unit cell, whereas the gray line portrays the depth of the unit cell taken into account by theoretical calculations in the following figures. (b) Bulk rhombohedral and corresponding projected hexagonal surface Brillouin zone for $EuSn_2P_2$, with high symmetry points and lines. Adapted from (Pierantozzi et al., 2022).

due to a strong magnetic anisotropy that prevents ordering along the *c*-axis; each layer is antiferromagnetically coupled with the nearest neighbour layers, resulting in intra-planar ferromagnetism and inter-planar antiferromagnetism. $EuSn_2P_2$ thus belongs to the class of A-type antiferromagnets, consistently with parent compounds like $EuSn_2As_2$ or $EuIn_2As_2$ (H.-C. Chen et al., 2020; Y. Xu et al., 2019). A sketch of the alignment of Eu magnetic moments is drawn in fig. 5.2a.

5.1.2 Terminations and surface states

$EuSn_2P_2$ is expected to host surface states with unusual properties. Figure 5.3 illustrates bulk- and surface-specific calculations showing the presence of surface states: in Eu- and Sn-terminated crystals, surface states are found only in the gap near Γ, whereas in the P-terminated surface they are more spaced out in k and should thus be visible up to ~ 1 eV binding energy.

Topological insulators are often described by means of topological invariants: the $\mathbb{Z}_2$ invariant, the mirror Chern number (MCN) n_M and the higher-order $\mathbb{Z}_4$ invariant. The formal treatment and physical meaning of all these parameters are beyond the scope of this section: more information can be found in (Fu and Kane, 2006; Kane and Mele, 2005).

In principle, $\mathbb{Z}_2$ is defined only when time-reversal symmetry is preserved; however it has been shown by (Mong, Essin and Moore, 2010b; Yu, Qi et al., 2011) that $\mathbb{Z}_2$ can be opportunely expanded when TRS-breaking magnetic order is present, but only if the system is arranged in a specific configuration. One of such cases is an AFI state, where time-reversal and lattice translational symmetries, represented by the operators Φ and $T_{1/2}$ are broken (by the onset of ferromagnetism and by the antiferromagnetic order, respectively) but the combined symmetry $S = \Phi T_{1/2}$ is preserved. The non-trivial topology

of $EuSn_2P_2$ is guaranteed by $\mathbb{Z}_2 = 1$.

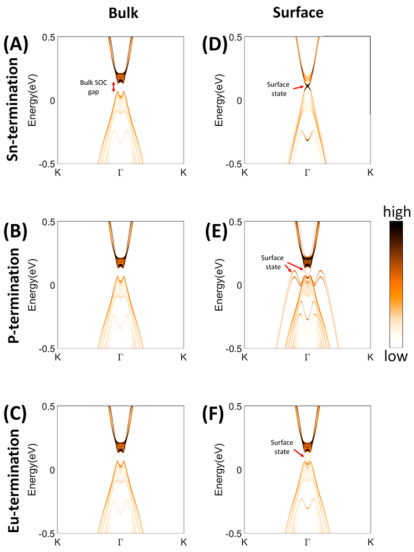

Figure 5.3: Calculated E vs k maps for different $EuSn_2P_2$ terminations: (a,d) Sn-terminated, (b,e) P-terminated, (c,f) Eu-terminated. The colour scale indicates the density of states within bands. Adapted from (Gui et al., 2019).

The MCN is a well-defined invariant for mirror-symmetric systems and can protect surfaces perpendicular to a mirror plane (Fu, 2011; Teo, Fu and Kane, 2008). In our case, $EuSn_2P_2$ has a MCN of $n_M = 1$.

Lastly, the parity-based higher-order $\mathbb{Z}_4$ invariant is well-defined even in absence of TRS for an inversion-symmetric system as $EuSn_2P_2$. This invariant is intimately connected with axionic properties; here calculations show that $\mathbb{Z}_4 = 2$, meaning that $EuSn_2P_2$ is a true candidate for axion physics.

5.2 Sample preparation

$EuSn_2P_2$ single crystals have been grown in Princeton by the Cava research group, using the Sn-flux method. More information on the characterisation of $EuSn_2P_2$ crystals can be found in (Gui et al., 2019).

2 mm to 4 mm diameter flakes have been glued on sample holders by means of Epo-Tek H20E epoxy glue, a silver-based electrically conductive bicomponent resin. The glue is heated to 150 °C for 5 minutes.

Surface-sensitive techniques such as ARPES tolerate an extremely low degree of surface contamination. Therefore, there are two ways of preparing samples suited for ARPES measurements. The sample may be grown directly inside a UHV chamber system and can be transferred in the measuring position without losing UHV conditions. This is not applicable for this sample, because of the lack of the necessary instrumentation to synthesise $EuSn_2P_2$ and/or transfer the crystals to the endstation in UHV conditions. However, the fact that the sample crystallises in layers parallel to the (001) surface (as in fig. 5.2a) suggests to follow the alternative solution of in-vacuum cleavage. In this case, a tiny metal or plastic rod is glued on top of the $EuSn_2P_2$ sample. The area of the rod has to be smaller than the sample surface area, and both the rod and the glue have to be carefully placed: a misaligned rod or an excess of glue partially covering an edge of the sample would prevent a clean and uniform cut and introduce surface strain and defects. The glue is cured with the same procedure previously illustrated.

The sample is then loaded into the vacuum system and mounted on the manipulator stage. After letting some time pass so that the sample reaches the equilibrium with the temperature of the cryostat, the cleave is performed by means of hitting the glued rod with the transfer wobblestick; a fresh surface is exposed and the rod is left to be retrieved later. It is relevant to specify that the quality of the surface resulting from the cleavage is reflected in the measurements: this issue will be addressed in section 5.6.

5.3 Results

The following measurements have been performed in one beamtime at APE-LE, one at APE-HE and one at I09.

In the first beamtime at APE-LE, $EuSn_2P_2$ samples were measured by ARPES and Spin-ARPES at six photon energies, from 27 eV to 50 eV, in a range of temperatures from 15 K to 80 K.

In the second beamtime at APE-HE, $EuSn_2P_2$ samples were measured by XPS at two photon energies, 400 eV and 810 eV, at room temperature and 100 K, as well as by XAS at 100 K across the $M_{4,5}$ edges of Eu at regular time intervals.

In the third beamtime at I09, $EuSn_2P_2$ samples were measured by XMCD across the $M_{4,5}$ edges of Eu at 15 K and 70 K, as well as by XPS at 900 eV and 1200 eV at the same temperatures.

5.4 Termination-dependent electronic behaviour

As already anticipated, the cleavage plane for $EuSn_2P_2$ crystals is the (001) surface. Sn@P_3 triangular pyramid layers and Eu layers alternate across the [001] direction, and within Sn-P layers the Sn-Sn bonds are weak: therefore, after a cleavage the crystal can present different terminations.

When comparing different cleavages, it is often challenging to discern the exact atomic termination by direct imaging. As a matter of fact, STM measurements locate atoms arranged in 2D triangular lattices with interatomic distances of 4.0(1) Å, compatible with all atomic planes (Pierantozzi et al., 2022).

However, the termination that is being measured can be identified from the electronic structure. As seen in the introduction, the theory predicts a different surface electronic structure depending on the termination: a direct comparison between first-principle calculations and ARPES data should give information on the atomic species exposed at the surface. The measurement of two different cleavages results in a stark difference in the electronic structure, as evident from ARPES Fermi surface and E vs k dispersion maps in fig. 5.4.

Features marked with red Greek letters will be described later: the important difference to be noted between the two experimental $k_x - k_y$ isoenergetic Fermi surfaces in fig. 5.4a is the presence of two extra bands, labelled σ and P, of which P matches first-principle calculations for a phosphorus-terminated surface. The near-hexagonal P band shows a strong warping in the neighbourhood of the hexagon vertexes. Such warping, found in small bandgap topological insulators as Bi_2Te_3, arises from a perturbative modulation of surface states and is predicted to give rise to exotic quantum properties deviating from those of an ideal Dirac cone (Fu, 2009). The absence of both σ and P bands at all binding energies in the case of the other termination is clear from the E vs k dispersion maps in fig. 5.4b-c.

A better characterisation of $EuSn_2P_2$ electronic states measured by ARPES along the $\bar{\Gamma}$–$\bar{K}$ and $\bar{\Gamma}$–$\bar{M}$ high-symmetry directions, together with corresponding first-principle calculations, is shown in fig. 5.5. The non-dispersive states labelled as ζ at $\sim$ 1.5 eV to 2 eV binding energy can be attributed to Eu *4f* orbitals. The band structure is otherwise dominated by numerous dispersive features labelled as $\alpha, \beta, \gamma, \delta$, mostly ascribable to P *3p* electrons. Some of them (β, γ, δ) are electron-like, whereas α remarkably shows a hole-like behaviour near the Fermi level.

As already noted, the relevant characteristic in the valence band dispersion is the presence of the two linearly dispersing bands σ and P. These two bands are clearly sep-

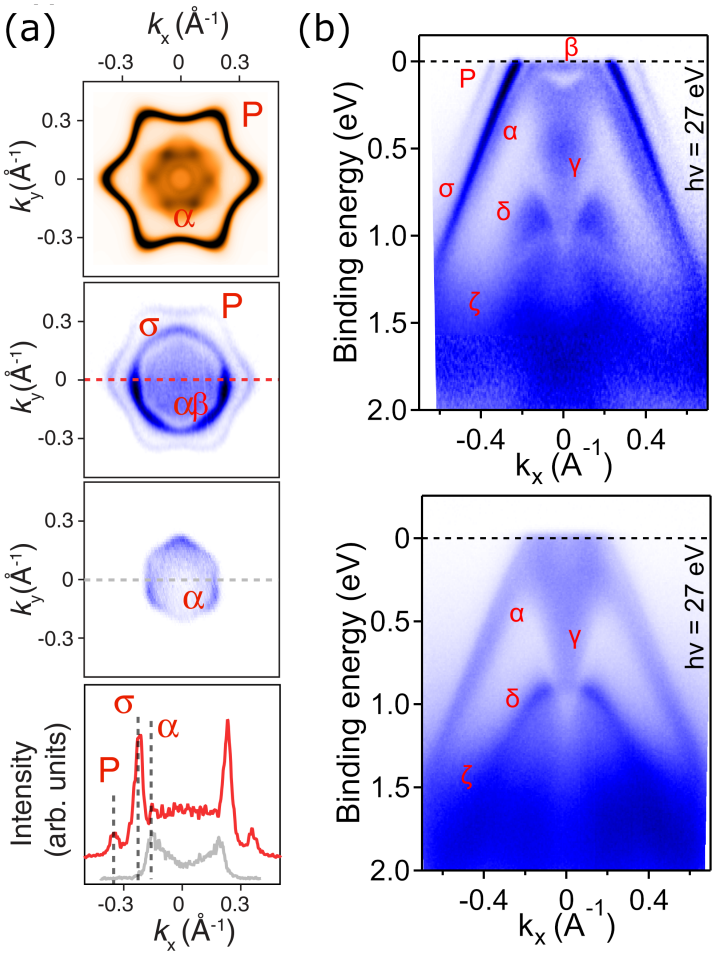

Figure 5.4: (a) From top to bottom: calculated $k_x - k_y$ isoenergetic Fermi surface for P-terminated surface, experimental $k_x - k_y$ isoenergetic Fermi surface for P-terminated and non P-terminated surfaces, experimental MDC cuts along k_x ($\bar{\Gamma} - \bar{K}$ symmetry direction) corresponding to the dashed red and gray lines in the Fermi surface data. Adapted from (Pierantozzi et al., 2022). (b) E vs *k* maps of $EuSn_2P_2$ valence band structure for P-terminated (*top*) and non-P terminated (*bottom*) surfaces.

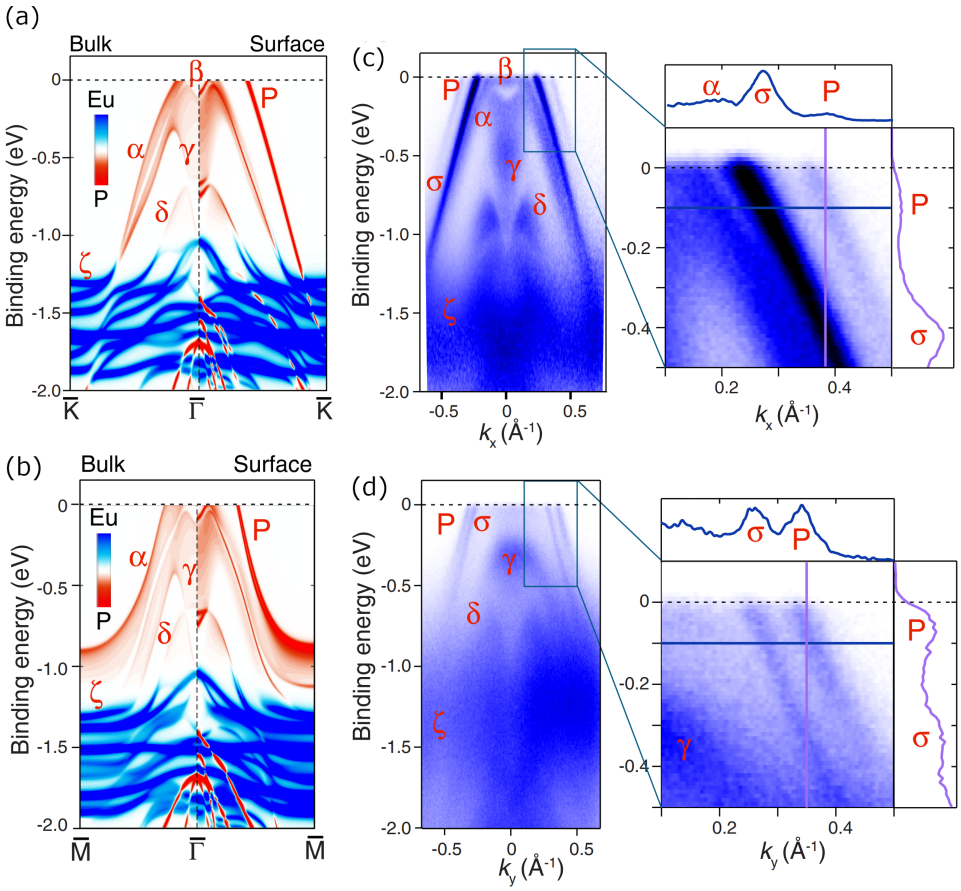

Figure 5.5: (a-b) Symmetry-resolved theoretical bulk (left) and surface-only (right) $EuSn_2P_2$ band structure, in the $\bar{\Gamma}$–$\bar{K}$ and $\bar{\Gamma}$–$\bar{M}$ high-symmetry directions, showing Eu and P orbital contributions. The position of the Fermi level has been adjusted to the experimental Fermi level. (c-d) ARPES E vs k maps along the $\bar{\Gamma}$ – $\bar{K}$ and $\bar{\Gamma}$ – $\bar{M}$ directions, measured with hν = 27 eV at 15 K and 80 K, respectively. (e-f) Magnified version of the same E vs k maps near E_F; in both cases, σ and P bands are highlighted via a EDC and MDC cuts. Adapted from (Pierantozzi et al., 2022).

arated from α, as indicated by the two zoomed-in windows in fig. 5.5d-f. As already shown in fig. 5.4a, in calculations a P-terminated surface gives rise to the P band, which is non-existent in bulk calculations (fig. 5.5a-b). P is thus clearly a surface state arising from P *3p* orbitals.

On the other hand, σ has no clear equivalent in both bulk and surface calculations. In well-characterised topological insulators such as Bi_2Se_3 and Bi_2Te_2Se, it has been shown that topological states may be accompanied by surface resonance (SR) states.(Cacho et al., 2015; Jozwiak, J. Sobota et al., 2016). These SR lie at lower *k*-values compared to the topological states but exhibit the same dispersion. We thus identify σ as a surface resonance band.

Compared to phosphorus, the metal centres give little contribution to the near-Fermi valence band, whereas just above E_F and below 2 eV binding energy Sn *5p* states can be observed, characterised by a strong mixing with P states. The latter case is highlighted in fig. 5.6, where orbitally projected calculations are compared to experimental E vs *k* dispersion maps.

The linearly dispersing P band has a Fermi velocity of 3.24 eV Å (4.92×10^5 m/s), comparable to other AFIs such as $MnBi_2Te_4$ (Y. J. Chen et al., 2019b), and k_F = 0.36 $Å^{-1}$. Photon energy-dependent isoenergetic cuts at different binding energies, shown in fig. 5.7, highlight the energy dependence of the matrix elements as well as the cross section of the P band. We note that higher photon energies result in P not being clearly visible probably due to matrix elements effects, whereas 27 eV, *i.e.* the photon energy we worked at, strongly emphasises the intensity of the band.

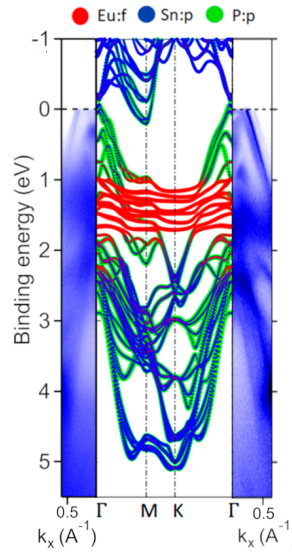

Figure 5.6: *Centre*: calculated electronic structure of bulk $EuSn_2P_2$. The colour code highlights the energy regimes of dominance of Eu, Sn and P contributions. Adapted from (Gui et al., 2019). *Left*: experimental E vs *k* map along the $\bar{\Gamma}-\bar{M}$ direction, for direct comparison with the leftmost part of the theoretical band dispersion. *Right*: same as left, but for $\bar{\Gamma}-\bar{K}$.

5.5 Surface chemical environment

We showed in the previous section that ARPES data are able to retrieve information on the surface termination. In order to get further insight into surface quality and chemical environment, trading the angular resolution for the sensitivity to single atomic species, we performed an XPS-based study on samples already cleaved and measured in ARPES.

Specifically, in this experimental run we characterised two $EuSn_2P_2$ crystals whose cleavages exposed two different surface terminations already seen in fig. 5.4, and replicated here below in fig. 5.8: the P-terminated surface belongs to sample H ("Highlander"), whereas the non P-terminated surface belongs to sample S ("Sauron").

A 1:1 correspondence between features the surface band structure and core photoemission peak lineshapes is actually hard to assess. Several differences between the two experiments need to be accounted for: different endstations, different beam spot sizes, different photon energies are the most relevant factors preventing a direct comparison. It should also be noted that ARPES results strongly depend on the local ordering of the irradiated surface: when scanning the surface of sample H, for example, we found stark

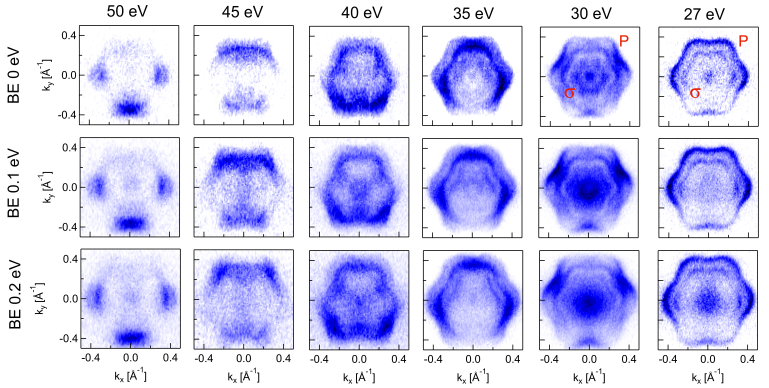

Figure 5.7: Photon energy-dependent k_x – k_y isoenergetic maps on a P-terminated $EuSn_2P_2$ surface; the photon energy ranges from 27 eV up to 50 eV.

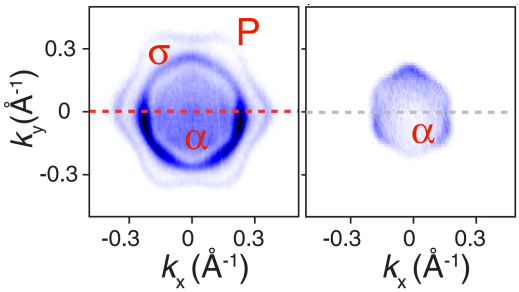

Figure 5.8: k_x – k_y isoenergetic maps for P-terminated (*left*) and non P-terminated (*right*) $EuSn_2P_2$ surfaces, corresponding respectively to sample H and sample S, acquired at $h\nu$ = 27 eV. Adapted from (Pierantozzi et al., 2022).

inhomogeneities among the ARPES E vs *k* maps depending on where the photon beam is impinging, as demonstrated by fig. 5.9. A cleavage may expose different layers and create a terrace-like surface; one of those terraces can be seen in the STM scan in fig. S1 of (Pierantozzi et al., 2022). The lack of a sufficient crystalline quality would severely hinder the protection of the topological states, meaning that the P band may not appear. Furthermore, there is no guarantee that those same layers are terminated by the same atomic species. It is easy to be lead astray by the hope that a uniform termination would be found over the whole sample area, but this expectation is highly unlikely.

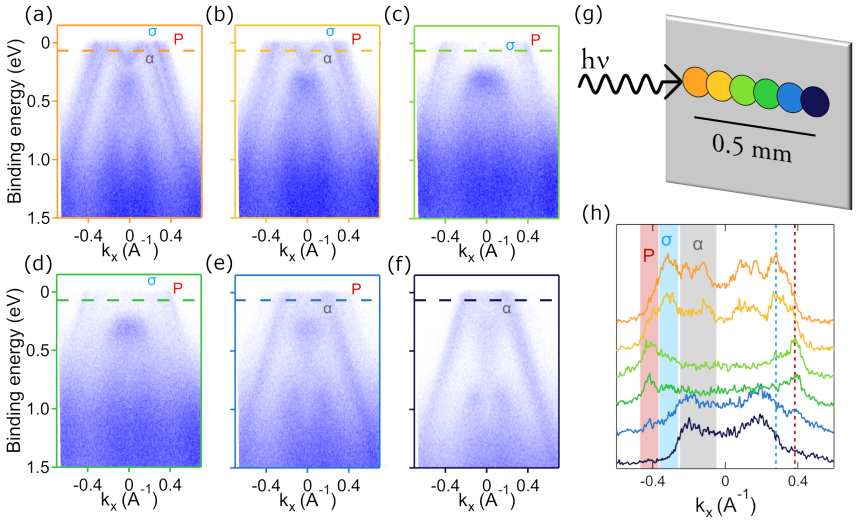

Figure 5.9: (a-f): E vs *k* maps showing the inhomogeneity of $EuSn_2P_2$ surface. Each colour corresponds to a different spot on the surface, as indicated by the scheme in (g), as well as to different MDC cuts in (h).

ARPES results can nonetheless be employed as a guideline, as they give a general anticipation of what can be expected from XPS results; extreme care will anyway be needed when drawing final conclusions.

First of all, XPS surveys across the whole available electron kinetic energy range have been carried out at 400 eV and 810 eV to check surface order and presence of contaminants (fig. 5.10a). On both samples there is no evidence of O adsorption; a small signal coming from C *1s* states at 284 eV is visible, but its magnitude together with the high cross section at these photon energies suggest that C surface contamination constitutes less than 20 % of the atomic density of P.[1]

This is expected, as these samples have been characterised by ARPES, which is highly sensitive to surface composition and contaminations. The high quality of ARPES data suggests that samples contamination was negligible; the *in-vacuo* sample transfer between the two APE endstations does not affect in a major way the surface cleanliness, as only a small amount of C revealed by the signature *1s* peak could be detected, with no other spectroscopic evidence of surface contaminants.

By comparing XPS surveys acquired on different samples at the same photon energy (fig. 5.10b-c and fig. 5.11), we can find proof of different surface conditions.

[1] Calculated with respect to the P 2*s* core level.

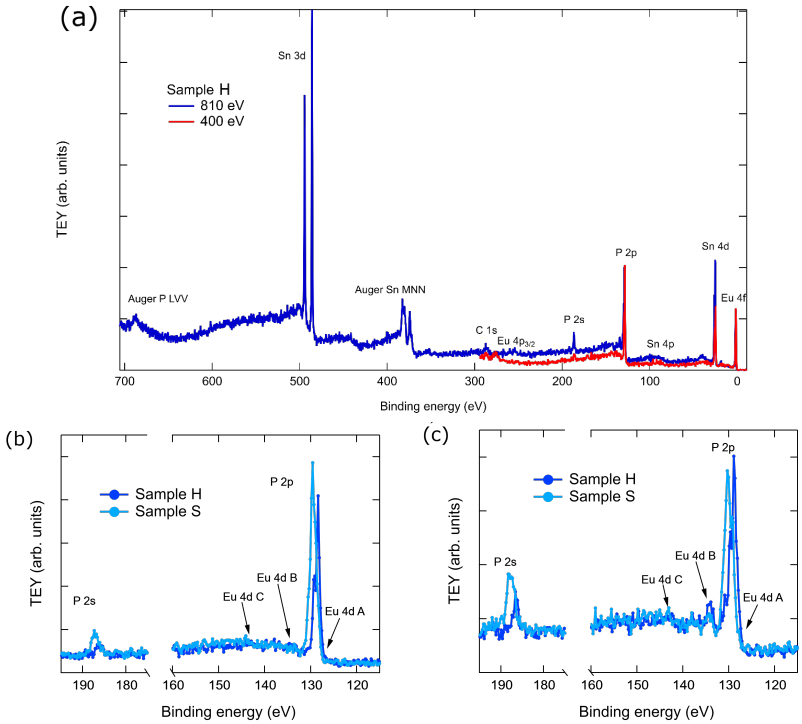

Figure 5.10: (a) XPS spectra of Eu, Sn and P core levels of $EuSn_2P_2$ sample 1, at two different photon energies (400 eV and 810 eV). The main photoemission features have been labelled to help identification. P *2s*, P *2p* and Eu *4d* core levels have been measured at $h\nu$ = 400 eV (b) and at $h\nu$ = 810 eV (c); for Eu *4d*, following the notation found in (Gerth et al., 2000), the labels A, B and C identify specific features in the Eu^{2+} photoemission spectrum.

On the one hand, Sn *4d* and *3d* states are *de facto* comparable in terms of lineshape and intensity, for both samples H and S and for both photon energies too (in the case of the *4d* shell), as seen in fig. 5.11. This suggests that Sn is not involved in bonding with surface atoms.

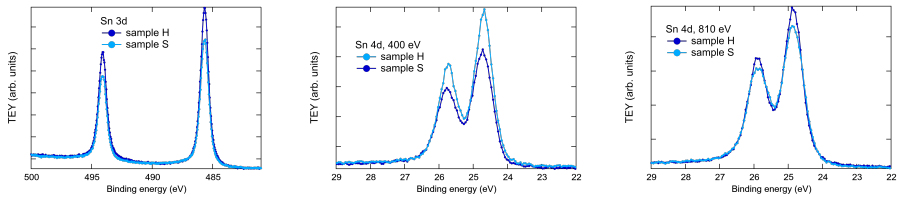

Figure 5.11: Sn *d* shells: Sn *3d* at hν = 810 eV (*left*), Sn *4d* at hν = 400 eV (*centre*) and Sn *4d* at hν = 810 eV (*right*).

On the other hand, phosphorus (P) states reveal several important differences between the two samples. Indeed, we may highlight two facts: (i) the P *2s* peak is significantly broader in sample S than it is in sample H, and (ii) the P *2p* peak shows a different lineshape. Point (i) hints at two inequivalent P chemical states coexisting in sample S; point (ii) asks for a more accurate inquiry, which we have performed in the form of the acquisition of narrow, high-resolution XPS spectra in the energy range of the P *2p* core level, which incidentally is the same binding energy region of Eu *4d* and Sn *4s* states.

Figure 5.12 reports the deconvolution of Eu *4d* and P *2p* peaks in this region for sample H as measured with the two different photon energies hν = 400 eV and hν = 810 eV. The measured spectrum shows for both samples an excellent agreement with the presence of the $2p_{1/2}$ and $2p_{3/2}$ phosphorus doublet, as well as a ^9D_J quintuplet and a peak around 134 eV binding energy (labelled B) as reported for Eu^{2+}, (Gerth et al., 2000) including branching ratio and spin-orbit splitting. The P *2p* shell lies between 128 eV and 130 eV binding energy, *i.e.* at the lower end of the binding energy interval reported in literature; these values have been observed for phosphides when P binds with elements closely related to tin in the periodic table (Moulder et al., 1992).

The identification of these features with Eu and P atomic species is further strengthened by a direct comparison between the two acquired photon energies.

In order to correctly assess the relative weight of the different spectral components at two photon energies, it is essential to take into account relative changes of both Eu *4d* and P *2p* photoionisation cross sections. Table 5.1 reports values of the total subshell photoionisation cross section for the elements of interest, with the addition of Sn *4s*.

When decreasing the photon energy from 810 eV to 400 eV, an estimation of the change in intensity of photoemission peaks related to P or Eu core levels is given by the change of photoionisation cross sections of each specific element at those photon energies: $\sigma_{P,400}/\sigma_{P,810}$ and $\sigma_{Eu,400}/\sigma_{Eu,810}$.

We thus multiplied P and Eu peaks, extracted from the fit of the spectrum at 810 eV, by the corresponding cross section ratios; the resulting peak structure, net of a global multiplication factor and a change in the background (because the photon energy of choice affects the total photon flux and the inelastic electron scattering), can be compared to the experimental spectrum acquired at 400 eV; as seen in fig. 5.13, the correspondence between the two is remarkable and confirms the identification of the features under exam with a P *2p* doublet and the Eu *4d* multipeak structure. As the kinetic energies of the peaks scale with the photon energy, the full correspondence of the fitting parameters indicates that there is no depth composition profile for the two elements.

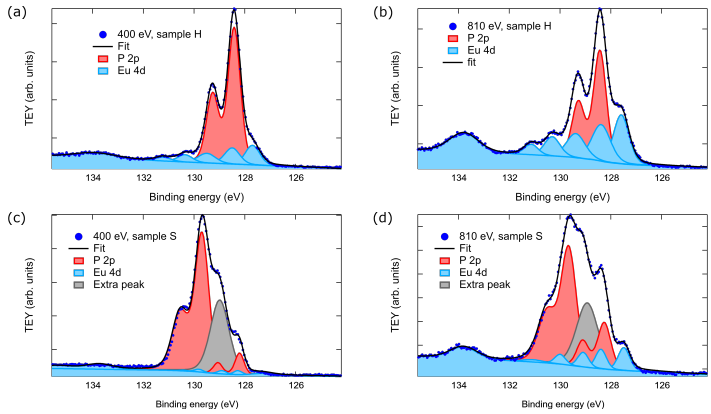

Figure 5.12: (a-b) XPS high-resolution spectra on P 2p core level energy region for sample H. Deconvoluted P (red), Eu (blue) and Sn (gray) peaks, at hν = 400 eV (a) and hν = 810 eV (b). (c-d) Same for sample S, at hν = 400 eV (c) and at hν = 810 eV (d).

Atomic orbital	S-O splitting (eV)	Cross section @ 400 eV (Mb)	Cross section @ 810 eV (Mb)
P *2p*	0.85	0.7348	0.098
Eu *4d*	5	0.851	0.408
Sn *4d*	1	0.5581	0.1621
Sn *3d*	8.4	-	1.723
Sn *4s*	-	0.0929	0.0299

Table 5.1: Comparison of spin-orbit (S-O) splitting and photoionisation cross section at 400 eV and 810 eV for different $EuSn_2P_2$ shells. Cross sections taken from (Yeh and Lindau, 1985), calculated in the dipole length approximation.

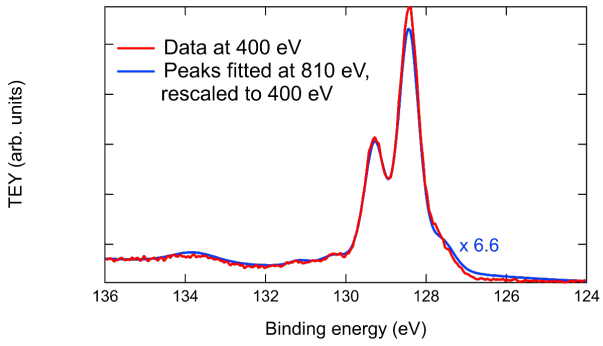

Figure 5.13: Experimental XPS high-resolution spectrum on P *2p* core level energy region for sample H at hν = 400 eV (red line) superimposed to peaks fitted from the XPS spectrum on the same sample at hν = 810 eV and rescaled according to the total cross section of the corresponding shell (blue line), as listed in table 5.1.

It is worth noting that we find no Sn *4s* signal in sample H (fig. 5.12a-b), despite a peak is expected in this energy interval. On this regard, we note that the Sn *4s* photoionization cross section is around one order of magnitude smaller compared to the other atomic subshells here considered (table 5.1), whereas the measurability of Sn *3d* and *4d* shells is related to their much higher cross section; the lack of a Sn *4s* signal is therefore not worrying.

Coversely, sample S seems more intriguing. First of all, we still verify the presence of the same Eu *4d* features. However, in this case we identify two distinct P *2p* doublets, whose $2p_{3/2}$ core levels lie at ∼128.2 eV and 129.6 eV binding energy. The former corresponds to the $2p_{3/2}$ core level in sample H, whereas in sample H we could not find an equivalent for the higher energy doublet. We may recall that the P *2s* core level in sample S appeared much broader compared to sample H (fig. 5.10b-c): this may lead us to hypothesise that sample S has two inequivalent P sites.

We also note that an additional peak at around 128.9 eV binding energy (fig. 5.12b-c) is required to fit the data. Another Eu-derived peak can be excluded, because all Eu peaks have been accounted for. Furthermore, the Eu peak at 134 eV, where no other spectroscopic features are intermingled, sets a limit on the intensity of Eu *4d* features, which cannot account for the high intensity of the extra peak at 128 eV.

On the other hand, the identification of this feature with the Sn *4s* core level would be puzzling, due to the large shift towards lower binding energy compared to the values reported in literature (generally around 137 eV (Moulder et al., 1992)); a 9 eV chemical shift is indeed quite unconvincing. In conclusion, the result of this analysis suggests that (i) a second P doublet is detected in sample S, with no equivalent in sample H, probably indicates two P sites, and (ii) an extra peak (whose attribution is challenging) is detected in sample S, hinting at a more complex surface environment in this sample.

5.6 Surface stability

In general, mechanical cleavage is in some way a "traumatic" operation for any sample. For example, the presence of charging effects of cleaved surfaces is a well-known phenomenon (J. F. Dillon and C. E. Olson, 1965; J. B. Engelhardt, Dabringhaus and Wandelt, 2000; Giuliani and Vignale, 2005a). We also already witnessed in fig. 5.9 the inhomogeneities on $EuSn_2P_2$ surface inducing a relevant variance in the electronic structure, as well as the starkingly different chemical environments at the surface in section 5.5. Probably owing to the combination of all these factors, cleavages have been observed to show a varying degree of stability.

For this reason, XAS spectra across the $M_{4,5}$ edge of Eu have been performed as a way of monitoring the sample conditions during the experiment. We chose the Eu $M_{4,5}$ absorption edge because it is a flag not only of the chemical state, but also of the magnetic state of the sample (as we will discuss in section 5.7).

In fig. 5.14 two cases representative of measured samples can be identified. In both of them a freshly cleaved sample is monitored during a day-long measurement. The first case, seen in fig. 5.14a, exemplifies an instance when the sample remains stable: the lineshape of the XAS denotes a pure Eu^{2+} valence state and is unchanged during the measurement. Conversely, in fig. 5.14b an evolution is monitored: the system clearly evolves from a pure Eu^{2+} state, to a mixed valence state, and finally to a Eu^{3+} state (Thole, van der Laan et al., 1985).

The formation of Eu^{3+} is accompanied by a gradual increase in the XPS intensity of the C *1s* shell, as seen in fig fig. 5.14c. We might conclude that surface contaminants act

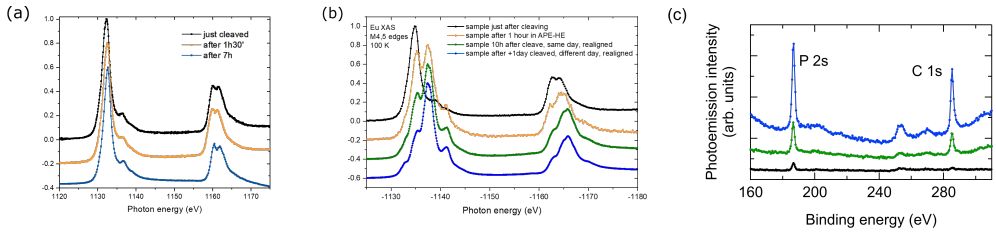

Figure 5.14: (a) XAS spectra across the $M_{4,5}$ edges of Eu for a stable surface. (b) XAS spectra across the $M_{4,5}$ edges of Eu when the cleavage renders the termination unstable. (c) XPS surveys evidencing surface contamination; the colour code corresponds to that in (b).

as ligands, leading to the formation of compounds with Eu^{2+} valence (Anderson et al., 2017; Negusse et al., 2009). In any case, a clear surface chemical evolution is taking place.

It should be specified that this effect has been observed only once, and in combination with a high degree of surface contamination as monitored by XPS; for this reason, it is extremely unlikely that such an occurrence might influence the other measurements we presented in this chapter, because in presence of a high degree of contaminants an ARPES spectrum would not be measurable at all.

Another relevant phenomenon taking place at the $EuSn_2P_2$ surface is charge doping. Even if exposed to UHV, cleaved surfaces may in the long run be subject to charge doping due to adsorbates. This evolution can be observed in ARPES as a shift of the Fermi level: the direction of the shift depends on the sign of the charges.

In fig. 5.15 we see an apparent shift of the E vs k ARPES maps towards higher binding energies: this corresponds to an electron doping, because of the shift upwards of the Fermi level. As explained in the caption, the timescale of this effect is a day or two; while this is long enough not to influence individual spectra acquisitions, the comparison of data from different days often requires a small rescaling.

Occasionally, a different effect has been measured. Figure 5.16a-b display two spectra acquired a day apart; in addition, in between the two measurements the sample was removed from the cold manipulator and placed in a storage area within the UHV system. The result is a shift in the opposite direction compared to the case in fig. 5.15: the spectrum drifted towards lower kinetic energies, *i.e.* the chemical potential has changed and the sample is electron-doped. After another day, a shift of the spectrum towards higher kinetic energies is again observed, therefore a progressive hole doping is taking place.

Given the phenomenology of the charge doping, we may propose an explanation to justify the above.

The presence of small quantities of oxygen in the UHV residual pressure is not surprising. Given the high electronegativity of oxygen, it is possible that electrons participating to O bonds are strongly attracted to the oxygen nuclei, depriving $EuSn_2P_2$ of valence electrons; in other words, adsorbed oxygen shifts the chemical potential, in practice behaving as an electron acceptor for the $EuSn_2P_2$ surface.

When the sample is moved to the storage area in between fig. 5.16a-b, there is no cryostat keeping it at 15 K anymore. When the temperature increases above its boiling point, the oxygen desorbs quickly and its acceptor-like behaviour disappears. After the sample is cryocooled again, oxygen starts to adsorb again and hole doping sets in.

All in all, the crucial takeaway from this section is that $EuSn_2P_2$ surfaces experience

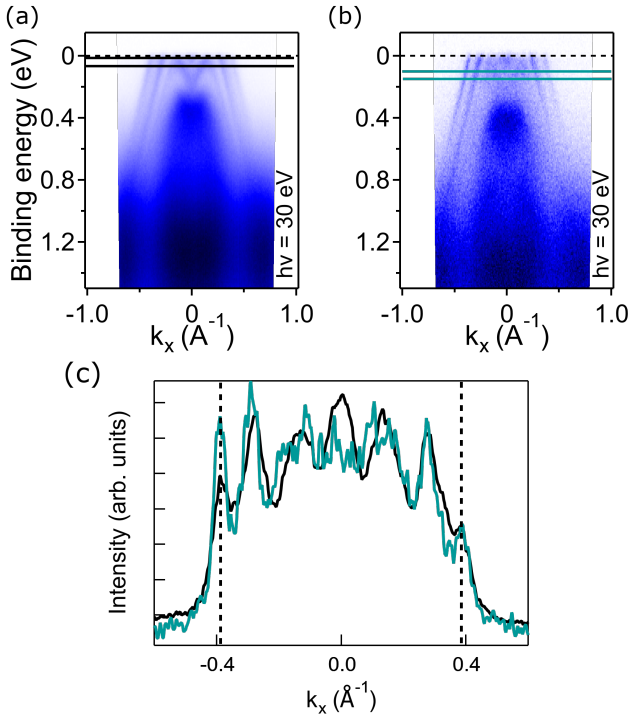

Figure 5.15: E vs k maps of the same cleavage at 60 K and hν = 30 eV: after (a) two and (b) four days of measurement. (c) MDC cuts along the coloured stripes.

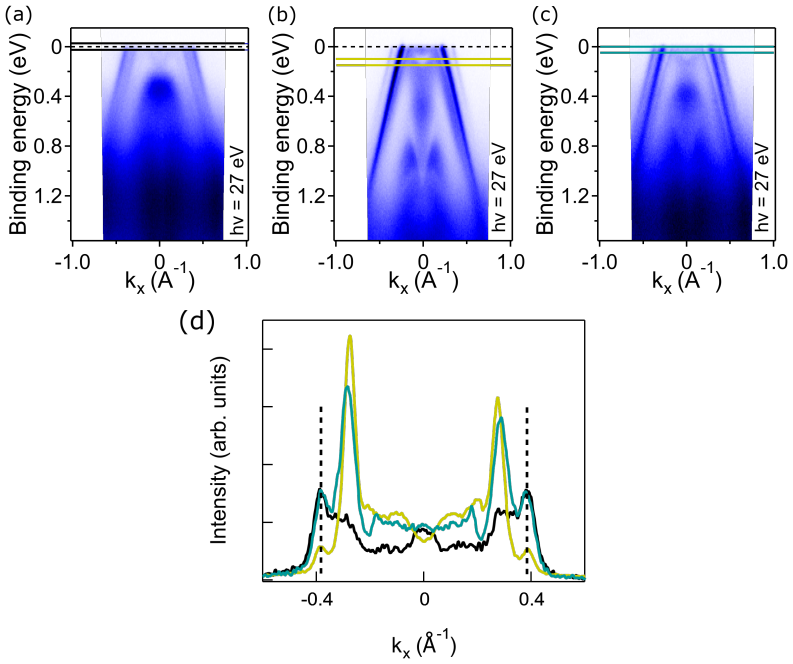

Figure 5.16: E vs k maps of the same cleavage at 15 K: after (a) two, (b) three and (c) four days of measurement. Inbetween (a) and (b) the sample has also been dismounted from the cryocooled manipulator. (d) MDC cuts along the coloured stripes.

varying degrees of stability with a complex phenomenology; however, some effects (like charge doping) can be understood and opportunely treated during data analysis, while others (like valence changes) can be monitored and used as a gauge to assess the validity of datasets acquired in those conditions. Once this is understood and properly taken into account with a rich enough dataset, then a reliable analysis on the ensemble of experimental results can be performed in these materials, in spite of the low energy scale of the characteristic electronic features. Anyway, the topological character of $EuSn_2P_2$ is robust with respect to these effects, as they bear no influence on the spin texture of the bands that we are going to illustrate in the next section.

5.7 Magnetic state and topological properties

As already mentioned, Eu *4f* electrons are highly localised in a non-dispersive band at 1.5 eV. It is known that electronic states with weak hybridisation favour spin unpairing, hence a localised magnetic character: this contributes to establish Eu as the main magnetic driver in $EuSn_2P_2$.

However, the proximity of the *4f* orbitals to the Fermi level could lead to instabilities in the Eu charge configuration. As we saw in section 5.6, the assessment of the Eu valence state is an important tool to determine the stability of the surface and uniformity of the termination, and thus ultimately the electronic properties of the material.

Firstly we performed XAS in TEY mode on a freshly cleaved sample. The top half of fig. 5.17 shows the Eu $M_{4,5}$ edges revealing a clear Eu^{2+} valence, from the comparison with (Thole, van der Laan et al., 1985).

Two XAS spectra measured with oppositely polarised circular light (circular left and circular right) result in an XMCD measurement, that gives insight into the average Eu magnetic moment across the footprint of the probing beam over the sample surface. Since Eu atomic planes are intra-layer ferromagnetically coupled, the average over a surface area would not affect the result. However, planes are antiferromagnetically coupled with each other; thus the probing depth of our measurement has to be assessed. Following (Frazer et al., 2003), we estimate at 6 nm our probing depth for XAS measurements across the Eu $M_{4,5}$ edges.

An XMCD signal is effectively measured at 15 K, below the magnetic transition temperature, as seen in the bottom half of fig. 5.17. The inset, from (Ruck et al., 2011), illustrates a dichroic signal from Eu^{2+} whose shape closely resembles our experimental data. The signal in that case however is between one and two orders of magnitude larger compared to the dichroism we measured on $EuSn_2P_2$.

To properly quantify the Eu spin magnetic moment from our acquired data, we follow the theory explained in (Thole, P. Carra et al., 1992) and (Paolo Carra et al., 1993);[2] hence we find $\mu_{s,eff} = 0.068(7)\ \mu_B$.

An isolated fully saturated Eu magnetic moment in the $4f^7$ $(6s^2)$ configuration has a total spin of S = 7/2; previous measurements on Eu $M_{4,5}$ edges yielded results close to the value of a free Eu^{2+} cation: $\mu_s = 6.6\ \mu_B$ in (Kawamoto et al., 2013), $\mu_s = 7.90(4)\ \mu_B$ in

[2] We adhere to the notation from (J. Stöhr and König, 1995) and write the spin magnetic moment for the $M_{4,5}$ edges as $\mu_{s,eff}(4f) = -\frac{5p-3q}{2r}\left(1 + 3\frac{T_z}{S_z}\right)^{-1} N_h$, where N_h is the number of holes in the *4f* shell, p is the integral of the XMCD signal over the M_5 edge, q is the integral of the XMCD signal over the M_5 and M_4 edges, r is the integral of the white line and T_z is the dipolar operator. Our calculation neglects the dipolar term T_z because our TEY measurement averages over several layers, and in first approximation estimates $N_h = 7$; we also consider the synchrotron light to be 100 % polarised, which is reasonably close to the experimental conditions of beamline I09 (see section 2.2).

(Arguilla et al., 2017), and magnetometry on $EuSn_2P_2$ itself yielded a saturated magnetisation of $\mu_S \sim 6.0\ \mu_B$ (Gui et al., 2019). The above means that our result is two orders of magnitude smaller than what at first could be expected.

The layered nature of $EuSn_2P_2$ may clear this behaviour. Since each Eu atomic plane lays at ∼9 Å from the next Eu layer, averaging the XMCD over 6 nm depth means the signal comes from 6 to 7 Eu layers, depending on the termination. This also explains why the signal is not exactly cancelled out by opposite contributions due to antiparallely aligned Eu spins: the contribution from each layer is weighted by their proximity to the surface, so that in the end a small intensity is detectable. Lastly, all XMCD data have been acquired in zero-field cooling conditions, *i.e.* without applying any external magnetic field; therefore, any signal is given by spontaneous magnetisation and may involve non perfectly aligned domains.

The dichroic signal disappears above the Néel temperature, as shown in fig. 5.17b: at 60 K the area is equally distributed above and below zero, whereas at 15 K points are mostly below zero, proving that within the experimental resolution the magnetisation vanishes above $T_{Néel}$.

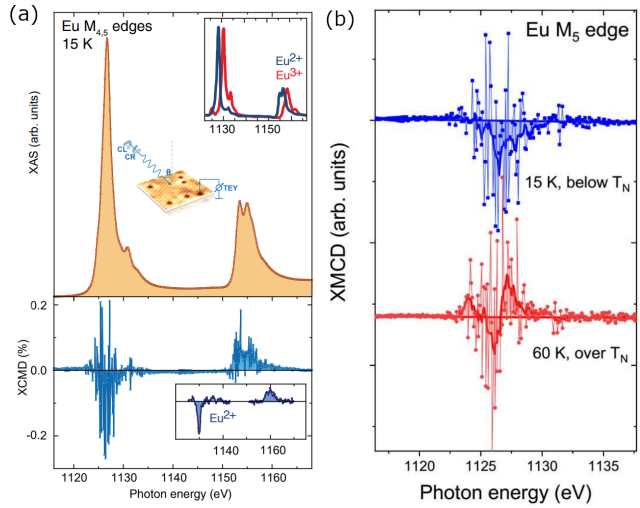

Figure 5.17: (a) *Top*: averaged (CR+CL) XAS spectrum across the Eu $M_{4,5}$ edges. The inset shows theoretical calculations of the $M_{4,5}$ edges for Eu^{2+} and Eu^{3+} valence states, from (Thole, van der Laan et al., 1985). *Bottom*: normalised XMCD across the same edges, obtained as the difference between absorption spectra with circular right and circular left polarisations. (b) Normalised XMCD obtained as the difference between absorption spectra with circular right and circular left polarisations, only at the M_5 edge. Adapted from (Pierantozzi et al., 2022).

Due to the geometry of the experiment, the XMCD signal in fig. 5.17 is compatible with A-type antiferromagnetism, but gives no information on the direction of the magnetisation. For this reason, vectorial spin-resolved ARPES measurements on the *4f* peak can be carried out to quantify the three components of the spin polarisation. As a matter of fact, Spin-ARPES is much more surface sensitive compared to XAS: a maximum of two Eu layers effectively do contribute to the measurement with the photon energy under exam (King et al., 2021; Seah and Dench, 1979), thus the first layer should give a

measurable contribution.

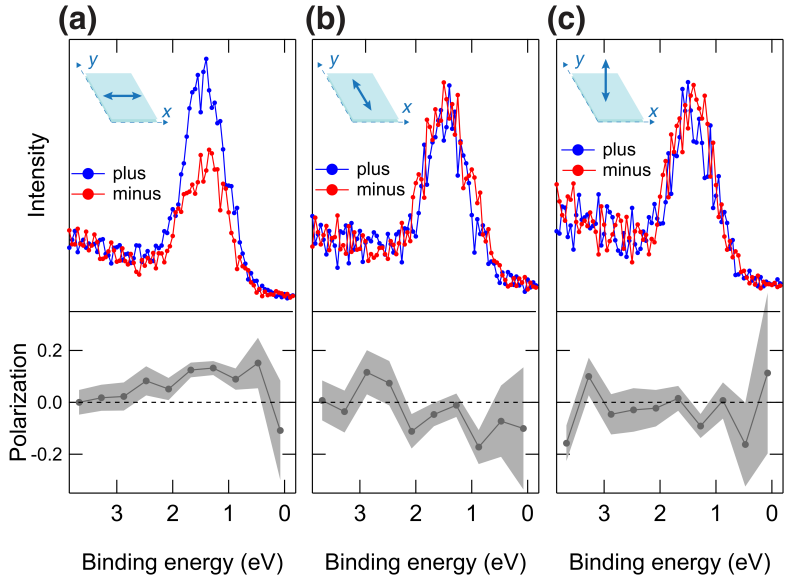

Figure 5.18: Spin-resolved EDCs on the Eu *4f* band, with the corresponding spin polarisation. The scheme in the top-left of each graph illustrates the direction along which the measurement has been performed. Adapted from (Pierantozzi et al., 2022).

Indeed, from fig. 5.18 it is evident that a spin-polarised signal (19 %) on Eu *4f* states is measured along the x direction. On the other hand, no spin polarisation is found along the y and z directions: the magnetisation is fully in-plane and has no out-of-plane component. Moreover, the polarised signal along x disappears above $T_{Néel}$ (fig. 5.19), following the same behaviour as the XMCD.

The combination of absorption and photoemission measurements allowed us to measure a fully Eu-derived magnetic signal in absence of external magnetic field. It is also confirmed that Eu magnetic moments are oriented in-plane, with no out-of-plane component, a result clearing the doubts left by neutron diffraction measurements. The first condition for the emergence of axion physics, the presence of long-range spontaneous magnetic ordering (C. Liu et al., 2020), is thus fulfilled.

The second step is ascertaining the character of $EuSn_2P_2$ topological bands in presence of AFM ordering. Spin-ARPES again can be applied to assess the spin polarisation of electrons from the topological band P pinpointed in fig. 5.5.

We measured spin-polarised EDCs at 15 K in two opposite k-points along the k_y direction: the inversion of the sign of the spin polarisation of the P band when momentum is reversed, seen in section 5.7, is a signature of spin-momentum locking.

The fact that σ shows the same spin inversion behaviour as P may be surprising, but it is documented that surface resonances accompanying topological states are actually spin polarised too and display spin inversion (Jozwiak, J. Sobota et al., 2016).

It is worth mentioning that in-plane ferromagnetism does not influence the topological character of our bands, compared to what has been observed in other similar systems such as $MnBi_2Te_4$ (Otrokov et al., 2019). Section 5.7 proves that the measured spin

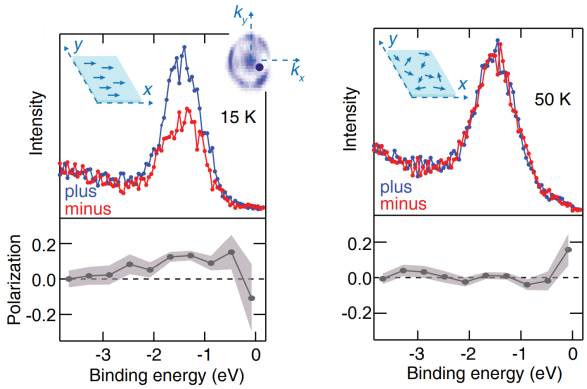

Figure 5.19: Spin-polarised EDCs along the x direction on the Eu $4f$ band, at 15 K and 50 K. The scheme in the top-left of each graph qualitatively mimics the degree of order of magnetic momenta. Adapted from (Pierantozzi et al., 2022).

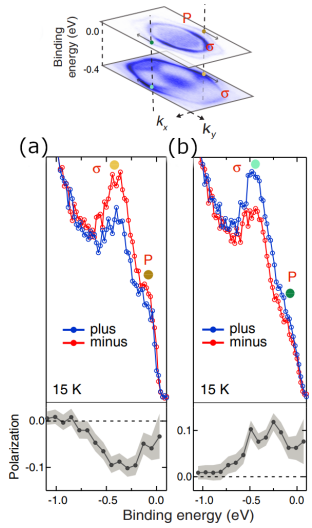

Figure 5.20: Spin-ARPES EDCs at fixed k-point (indicated by the dots in the isoenergetic maps at the top) measured with hν = 27 eV at 15 K along the y direction. The EDCs are extracted at a positive (a) and negative (b) k-point. The resulting spin polarisation for each curve is also shown as a gray line and a shaded area to represent the error. Adapted from (Pierantozzi et al., 2022).

polarisation is fully in-plane along the y direction, and no other component is detected for the P band.

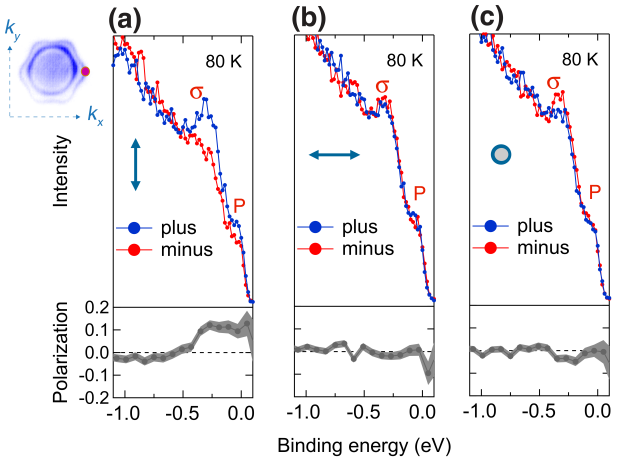

Figure 5.21: Spin-ARPES EDC cuts at a fixed k-point (indicated by the magenta dot in the isoenergetic map at the top left) measured with hν = 27 eV at 80 K along the y (a), x (b) and z (c) directions. The resulting spin polarisation for each curve is also shown as a gray line and a shaded area to represent the error. Adapted from (Pierantozzi et al., 2022).

Moreover, at 80 K, *i.e.* above the magnetic transition, the spin-momentum locking persists on both σ and P, confirming that the origin of this spin polarisation signal is not magnetic: the in-plane magnetisation does not influence topological states, as opposed to what happens for out-of-plane magnetic moments in $MnBi_2Te_4$ (Otrokov et al., 2019): the bands are thus characterised by a *strong* topological character.

This outcome is in some way expected, because we saw from fig. 5.5 onwards that Eu *4f* orbitals are highly localised. A hybridisation with P-derived bands would be expected to be unlikely and weak, and then the shift/realignment of spins due to the local magnetic field is negligible.

We must note that two topological bands are predicted by first-principle calculations, but a single band is measured, within the experimental resolution of ΔE = 30 meV and Δk = 0.01 Å^{-1}, by both ARPES and Spin-ARPES. The latter would in principle be able to resolve finer details: even if the bands partially overlap within the experimental resolution, and a spin-integrated measurement reveals a photoemission intensity apparently ascribable to a single band, the spin resolution would discern the opposite sign of the spin polarisation from the two separate bands. In any way, the presence of a spin polarisation could be due to an imbalance in the spin-projected weight of the two bands.

Finally, a discussion is warranted about the veracity of spin polarisation measurements in ARPES, which has been questioned with merit (Jozwiak, Y. L. Chen et al., 2011). As a matter of fact, final-state effects on photoelectrons from circularly polarised 6 eV photons are responsible of inversion or oscillations of the value of the spin polarisation, via spin-dependent matrix elements. However, it has been shown by (Sánchez-Barriga et al., 2014) that while final-state effects dominate in the low-energy regime, photons in the UV range probe the initial-state spin texture. Our 27 eV photon is lower than the range from 50 eV to 70 eV considered in the above study, but it is still large enough to probe an energy region sufficiently far away from the Fermi level: we can conclude that

the measured dependence of the spin polarisation on the k vector is likely not resulting from final-state effects, but is derived from a true topological property.

5.8 Closing remarks and open questions

In the previous sections, we presented absorption and photoemission spectroscopy measurements on $EuSn_2P_2$ aimed at characterising its electronic and magnetic properties, as well as how each of the two influences the other. The main results can be summarised as follows:

1. the electronic structure is termination-dependent, with a complex surface chemical environment and extra phosphorus-originated bands;
2. fully Eu-derived in-plane ferromagnetic order and layered antiferromagnetic coupling coexist below the Néel temperature;
3. P and σ surface-exclusive states display spin-momentum locking independently on the temperature.

Our work, by confirming $EuSn_2P_2$ as a potential axion insulator candidate, provides a strong argument in favour of the experimental realisation of the axion insulator phase.

The careful reader would probably have noticed by now a discrepancy between the expectations set in the overview in section 5.1 and the results herein outlined. Although the introductory part mentioned the overlap of two Dirac cones connected at the Dirac point, the experimental evidence showed a warped, linearly dispersing band converging somewhere above the Fermi level; no direct visualisation of the Dirac point is possible in the current state.

We performed two series of tests to measure the Dirac point. In the first case, we measured Gd-doped $EuSn_2P_2$ crystals: Gd acts as an electron donor due to the $4f^7 5d^1$ electronic configuration. In this case, the band structure did not display an appreciable difference other than a general decrease in quality of the ARPES image due to lower crystalline order and the absence of surface states. This confirms Eu as an important driver in the determination of the topology in $EuSn_2P_2$ as even doping with small quantities of a neighbour element prevents the high-quality data we witnessed in intrinsic crystals.

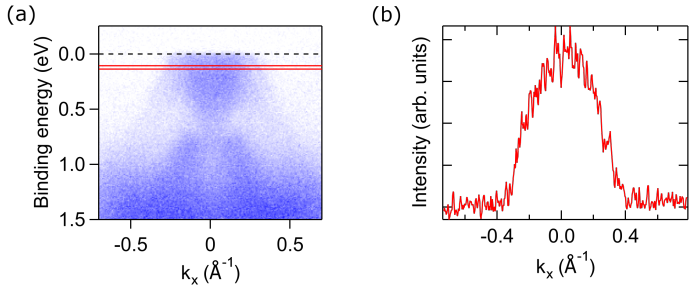

Figure 5.22: (a): E vs k maps of Gd-doped $EuSn_2P_2$, at hν = 30 eV, and (b) MDC cut corresponding to the red stripe in (a), to further evidence the absence of the surface states.

In the second instance, we tried to populate the empty electronic states by potassium (K) dosing directly on $EuSn_2P_2$ surface. This is a standard procedure in *e.g.* MoS_2 (Y.

Zhang et al., 2016) for observing the bottom of the conduction band in direct photoemission: due to its extremely low electron affinity, K provides electrons "locally", *i.e.* only at the sample surface, but for surface-sensitive ARPES measurements it is a totally acceptable compromise. On our sample the shift of the Fermi level was only in the order of some hundreds of millielectronvolt - K evaporation must be limited to a low dosage, because even the formation of 0.2 monolayer is sufficient for the emergence of K-induced surface states (Magnusson and Reihl, 1989). Moreover, the shift was accompanied by a progressive degradation of the quality of the spectrum, to the point where topological surface states were not detected anymore.

Still, some hypothesis can be formulated on the presence of the Dirac point and its position with respect to symmetry points: the concern is anything but trivial, as explained in the next paragraph.

On the one hand, the value of the higher-order $\mathbb{Z}_4$ invariant hints at a non-trivial axion coupling, and thus gapped surface states and gapless chiral hinge states on all surfaces. On the other hand, $\mathbb{Z}_4$ is not the only invariant protecting surface states: indeed, the $\mathbb{Z}_2$ invariant should protect the surface states on the (010) surface of $EuSn_2P_2$, the side surface with respect to the atomic layers, and the MCN n^M should protect another gapless surface state on the surface perpendicular to a mirror plane lying along the *c*-axis, *i.e.* a surface state along the Γ-M direction of the (001) plane (H. Li et al., 2019). In the latter case, the Dirac point is not pinned on $\bar{\Gamma}$, but lies in the in-plane direction projection of the mirror plane: along k_y. This is due to TRS breaking, because of intra-layer ferromagnetism, differently from the side surface.

A similar situation has been identified in $EuSn_2As_2$ (section 5.8a).

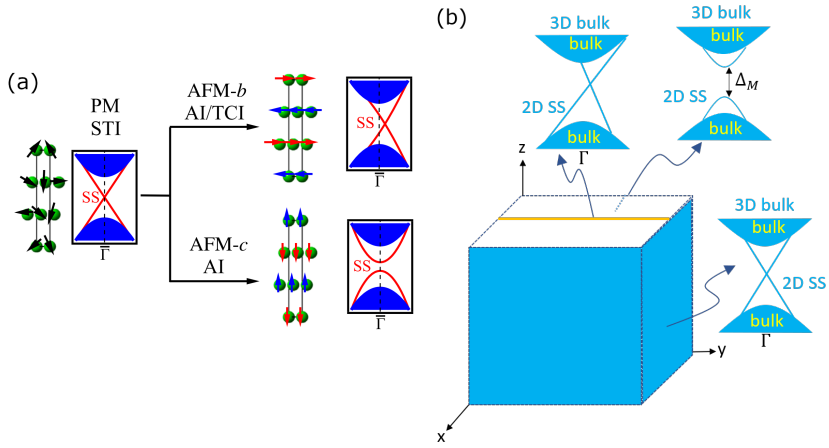

Figure 5.23: (a) Diagram of the Dirac cone of $EuSn_2As_2$ in different magnetic phases: paramagnetic (PM), in-plane antiferromagnetic (AFM-*b*) and out-of-plane antiferromagnetic (AFM-*c*). Adapted from (H. Li et al., 2019). (b) Sketch of the surface states on different surfaces of $EuSn_2P_2$ depending on the topological protection .

$EuSn_2P_2$ indeed shows a multifaceted topology linked to the alignment of Eu magnetic moments, again hinting at the importance of Eu for the stabilisation of topological properties in this material. However, these are theoretical predictions and as we saw, the determination of the presence or absence of an energy gap in $EuSn_2P_2$ surfaces is so far inaccessible. If an experimental confirmation or rebuttal of the above picture is to be

pursued, the route to follow should be leading to time-resolved photoemission.

This strategy has already been applied with success to *e.g.* Sb_2Te_3 (Zhu et al., 2015), which shares with $EuSn_2P_2$ the separation of the topological states in the neighbourhood of the Dirac cone from the bulk states; on the other hand, in other topological insulators such as Bi_2Se_3 the Dirac cone is not isolated from bulk bands, rendering the spectroscopic disentanglement of different contributions much harder (J. A. Sobota et al., 2013).

The fact that both the upper and lower parts of the Dirac cone are empty does not allow a direct visualisation by direct photoemission; however, there is an advantage of this configuration, in the sense that a pump-probe experiment would be able not only to populate empty electronic states and confirm the theoretical prediction (as well as possibly probing the presence of a shift of the Dirac point from $\bar{\Gamma}$ in the magnetic phase, and its absence below the Néel temperature), but also to study the hot carrier dynamics and the interplay with the spin degrees of freedom in view of potential applications for ultrafast devices.

Part III

2D materials, the advent of magnetism in flatland

CHAPTER 6

Magnetic semiconductors VI_3 and CrI_3

> I call our world Flatland, not because we call it so, but to make its nature clearer to you, my happy readers, who are privileged to live in Space.
>
> Edwin Abbott, *Flatland*

6.1 Overview

As we saw in the previous part, spatial confinement plays a huge role in tailoring magnetic and topological properties in $EuSn_2P_2$. Low-dimensional systems are subject to a significant reduction of their phase space and screening: both factors favour enhancement of electronic correlations and emergence of quantum effects.

Layered crystals, often known as *van der Waals* (vdW) crystals, are a class of materials exhibiting strong in-plane covalent bonds but weak out-of-plane van der Waals forces; as a consequence, the interconnection of atomic orbitals between planes is greatly diminished, and planar structures composed of few layers or even a single layer can be easily isolated. Therefore, exfoliation down to the monolayer limit and engineering tailored heterostructures is rather straightforward.

The most famous example in this family is graphene, whose (re)discovery in 2004 in its free-standing form triggered an enormous amount of research (Geim and Novoselov, 2007; Novoselov, Geim et al., 2004; Novoselov, Jiang et al., 2005). Since then, several subclasses were identified, owing to different crystalline structure and electronic properties (fig. 6.1).

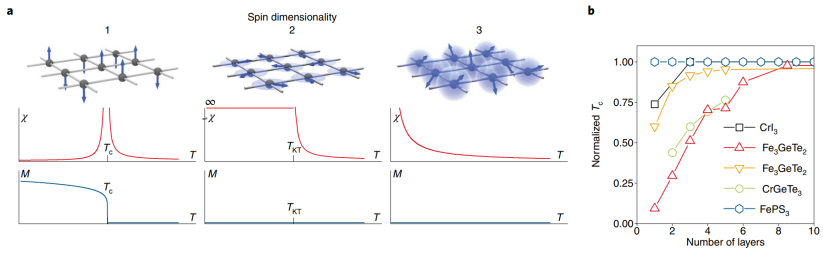

Figure 6.1: Role of spin dimensionality (a) and evolution of the Curie temperature T_C (b) in two-dimensional systems. Adapted from (Gibertini et al., 2019).

Pushing the limit towards atomically thin magnetic materials is proven to drastically change the properties of 3D crystals: a notorious and well-characterised example is the indirect-to-direct bandgap transition in transition metal dichalcogenides (TMD) (Mak et al., 2010). In general, vdW materials are known to exhibit a host of exotic quantum properties, such as Mott transitions (Y.-P. Wang and Long, 2020), Dirac physics (L. Chen et al., 2021; T. Yang et al., 2020) and even layer-dependent long-range magnetic order (Butler et al., 2013; Gibertini et al., 2019; Mounet et al., 2018; Samarth, 2017): exploring and exploiting vdW crystals for novel optical, electronic and magnetic "few-layers" functionalities has become a real possibility.

6.1.1 Transition metal iodides

Within the class of vdW materials, layered transition metal compounds - in particular the family of transition-metal iodides MX_3, where M is a transition metal species and X is a halogen - have attracted a large deal of attention. Crystals such as CrI_3 and VI_3 undergo structural and electronic transitions as a function of temperature, exhibit net long-range magnetisation within layers and, in the case of CrI_3, layered antiferromagnetism (Gati et al., 2019; He et al., 2016; B. Huang et al., 2017; Liqin and Katsnelson, 2021; McGuire, Dixit et al., 2015; Son et al., 2019; Tian et al., 2019).

The importance of dimensionality effects has been recognised and for this reason the majority of experimental and theoretical work has focused on monolayers and few-layers films. However, both the interplay of dimensionality with spin-orbit coupling (SOC) and orbital ordering and the possible crossover of 3D vs. 2D electronic properties are not well understood.

In this respect, open questions include: i) the role of Coulomb interaction and SOC in determining the *3d* electronic states and their long- and short-range ordered collective excitations (Reyes-Retana and Cervantes-Sodi, 2016), ii) if and how the orbital filling in the electronic ground state is modified at the surface in view of "few-layers" applications, and iii) whether the bandwidth and the hybridisation of halogen and transition metal states change when dimensionality is reduced, *e.g.* from bulk to surface.

Detailed experimental information on the ground state electronic properties of transition metal iodides is still lacking, often owing to their extreme air sensitivity and challenging chemical environment: these materials are known to be extremely hygroscopic, to the point of irreversible dissolution if exposed to ambient conditions.

The above issues need to be experimentally addressed, since they have a significant impact in the potential electronic and spintronic applications and their control may drive the progress in understanding the role of relevant interactions in defining the properties of these materials when dimensionality is reduced (Nguyen et al., 2021; Zollner, Gmitra and Fabian, 2020).

Part of the experimental results described in this chapter have been published in (De Vita et al., 2022). A portion of the unpublished data is currently under scrutiny and another publication is in preparation.

6.1.2 Crystalline and electronic structure

The crystal structure of MI_3 (M = Cr, V) is characterised by one M cation surrounded by six I anions, arranged in edge-sharing octahedra. Within the planes, the M atoms are arranged in a honeycomb geometry, as shown in fig. 6.2a.

fig. 6.2b reports the bulk and surface-projected first Brillouin zone for VI_3 and CrI_3. As for $EuSn_2P_2$, the extreme surface sensitivity of ARPES when performed with photon

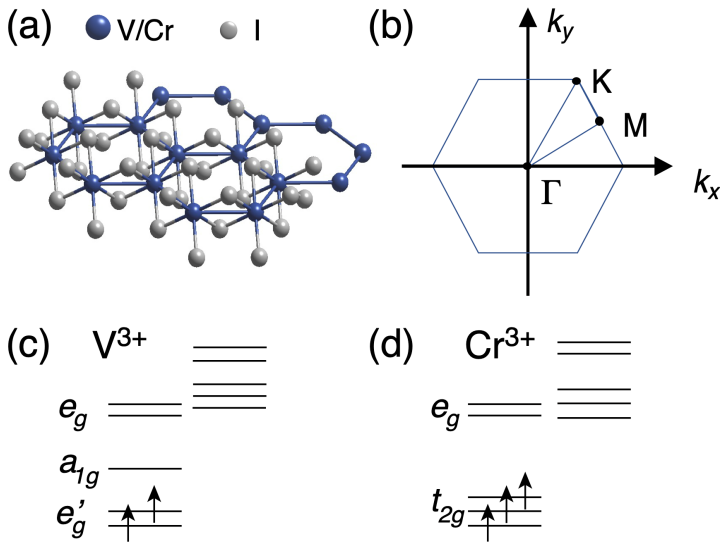

Figure 6.2: (a) Crystal structure of CrI_3 and VI_3 monolayers. (b) 2D Brillouin zone. Crystal-field splitting and related electron filling for (c) Cr and (d) V. From (De Vita et al., 2022).

energies in the range from 20 eV to 55 eV (from 5 to 10 Å (Seah and Dench, 1979), corresponding to a single layer unit) means that we are actually probing the topmost layer of the whole MI_3 structure, so we must refer to the surface-projected BZ.

CrI_3 undergoes a structural transition at $T_{S,CrI3} = 220$ K from the high-temperature monoclinic structure to the low-temperature rhombohedral structure R-3, while VI_3 changes from the rhombohedral structure R-3 above $T_{S,VI3} = 79$ eV K to a monoclinic phase below the transition temperature (C. Huang et al., 2020).

Both CrI_3 and VI_3 are extremely vulnerable to contamination in ambient conditions and intense photon exposure, in particular in presence of moisture (Kratochvílová et al., 2022).

Concerning the electronic structure, the expected crystal field splitting and related electronic filling for Cr^{3+} and V^{3+} are reported for reference in fig. 6.2c-d. In particular, we note a key difference between VI_3 and CrI_3: the latter shows a standard t_{2g}-e_g crystal field splitting, while the former displays an additional splitting of the t_{2g} levels into e'_g and a_{1g}. The trigonal distortion in this system is small and thus not able alone to significantly split the t_{2g} into e'_g and a_{1g}; an energy gap is opened by an additional on-site Coulomb interaction contribution.

For VI_3, two different descriptions were proposed in literature: (i) a metallic ground state, in which the a_{1g} orbital state is fully occupied, and the doubly degenerate e'_g orbital state is half occupied (He et al., 2016; Kong et al., 2019; K. Yang et al., 2020); (ii) a Mott-insulating ground state, in which the e'_g state is fully occupied, while the a_{1g} state is unoccupied (Nguyen et al., 2021; Zhou, Pandey and Feng, 2021).

This last picture appears to be consistent with a previous experimental measure of the optical band gap in VI_3 (Kong et al., 2019; Son et al., 2019) and a recent spectroscopic investigation (Kundu et al., 2020): indeed, no density of states at the Fermi level has been detected. However, a firm characterization of the ground state of VI_3 has not been reached yet.

As for CrI_3, it has been proposed that a surface structural relaxation may explain the onset of bulk ferromagnetism vs few-layers antiferromagnetism (Z. Wang et al., 2018); conversely, it has also been argued that parallel spin states are energetically favoured in both stacking configurations, and anyway the result strongly depends on the on-site Coulomb energy employed in the calculations (Nguyen et al., 2021).

The above considerations demonstrate that a fair share of debate has been dealing with the ground state properties of CrI_3 and VI_3. A better understanding of the orbital occupation/arrangement would be helpful to reveal its influence on the electronic ground state configuration; furthermore, additional insight is needed to determine to what extent interlayer interactions affect and determine the electron configuration and magnetic behaviour.

6.2 Sample preparation

Commercially available VI_3 and CrI_3 crystals were mounted on sample holders in an N_2 glovebox environment; in order not to expose them to air, they were transferred in N_2 atmosphere to the ultrahigh-vacuum (UHV) chamber system by means of a specifically designed suitcase, prior to be cleaved at p = 5×10^{-10} mbar.

6.3 Results

The samples were measured at the APE-LE beamline of the synchrotron radiation source Elettra (Trieste, Italy). The ARPES experiments were performed at a base pressure better than 5×10^{-10} mbar using p-polarized light (45° incidence, normal emission), unless otherwise specified. Samples were grounded and measurements of the Fermi edge from a polycrystalline Au foil have been used to estimate the position of the Fermi level and help in compensating charging effects, as explained in the eponymous section.

The sample is oriented such that the analyser slit, and thus the probed momentum, lies along the $\bar{\Gamma} - \bar{K}$ symmetry direction. In our experimental geometry, s-polarised photons have only an in-plane component parallel to the analyser slit and hence in the mirror plane; p-polarised photons instead have an in-plane orthogonal to the analyser slit and hence to the mirror plane, but they also possess an out-of-plane component which by definition lies in the mirror plane. This implies that both light polarisation vectors have one component (in-plane for s-polarisation, out-of-plane for p-polarisation) which is symmetric with respect to the mirror plane, so that non-zero matrix elements are expected.

XAS measurements have been performed at the APE-HE beamline of the synchrotron radiation source Elettra (Trieste, Italy), in total electron yield (TEY) mode, at a base pressure better than 5×10^{-10} mbar. p-polarized light was used at 45° incidence.

6.4 Charging effects

MI_3 vdW crystals are semiconductors: due to the sizeable bandgap, samples exhibit charging upon photon flux exposure. Measurements have been performed with decreasing photon flux, in order to assess the charging effect on the band structure (Fig. fig. 6.3): the resulting spectra show that, if the sample temperature is not too low, charging does not influence the lineshape but rigidly shifts the curve towards higher BEs.

We set the minimum temperature for our measurement by noticing when charging effects start becoming more problematic, i.e. when spectral deformation takes place.

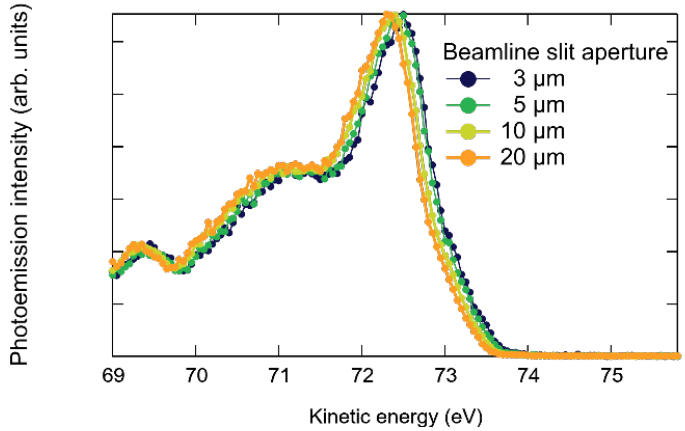

Figure 6.3: Angle-integrated spectra of CrI_3 ($h\nu$ = 80 eV, T = 300 K) as a function of the aperture of the beamline slit, regulating the photon flux impinging on the sample. Charging effects are manifest at higher fluxes as a rigid shift of the spectrum towards lower kinetic energies. From (De Vita et al., 2022).

Measuring at any lower temperature than 150 K for VI_3 and 300 K for CrI_3 foils any attempt of reproducibility in our case.

Since a small sample charging only affects the position of the spectrum in kinetic energy and not its lineshape, this affects the estimation of the position of the Fermi level. We reduced the photon fluence of the measurement until no shift is observed, as shown in Fig. fig. 6.3. We set this experimental condition as representative of a non-charging spectrum.

At the same time, we acquired the spectrum from a polycrystalline Au foil across the Fermi edge: the correspondence between these two independent measurements allowed us to properly rescale the kinetic energy scale to binding energy on the non-charging spectrum. This acted as a reference for the evaluation of any charging effect shift of the other spectra.

6.5 Bulk and surface bands and orbital filling

In order to assess the valence of the metal centres in the two compounds, XAS measurements across the V and Cr $L_{2,3}$ edges have been carried out; results are shown in fig. 6.4.

For VI_3, there are no XAS spectra in literature that we are currently aware of, so no direct term of comparison is available; anyway, V $L_{2,3}$ edges closely resemble those of other V-based compounds with a 3+ valence state, such as V_2O_3 (Caputo et al., 2022; Groot et al., 1990), including the characteristic V *2p* to V *3d* transitions to the empty t_{2g} states, visible in the near-edge regions at 514 eV and 522 eV (fig. 6.4a). On the other hand, the lineshape and photon energy of L_3 and L_2 edges of CrI_3 are fully consistent with previous measurements on the same compound (Groot et al., 1990; D.-H. Kim et al., 2019), where comparisons with theoretical simulations of Cr^{3+} $L_{2,3}$ absorption edges based on crystal field theory show excellent agreement with experiments. The above thus confirms the 3+ valence state of bulk VI_3 and CrI_3.

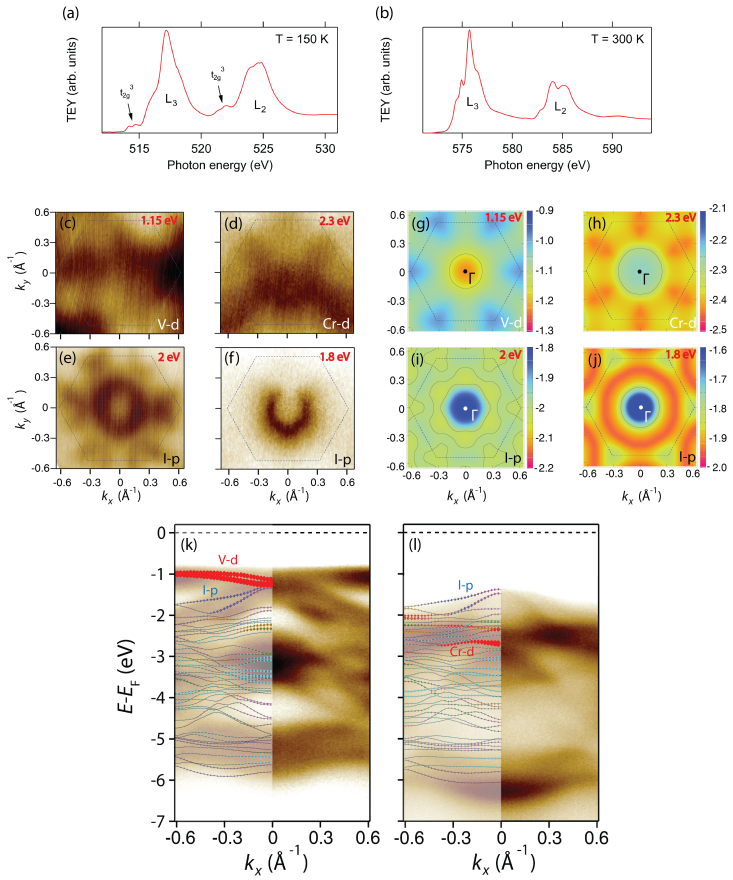

Figure 6.4: XAS spectrum of VI_3 (a) over the V $L_{2,3}$ edge (T = 150 K), and CrI_3 (b) over the Cr $L_{2,3}$ edge (T = 300 K).
ARPES isoenergetic k_x-k_y maps of VI3 (T = 150 K, hν = 32 eV) at (c) 1.15 eV and (e) 2 eV, and CrI_3 (T = 300 K, hν = 41 eV) at (d) 2.3 eV and (f) 1.8 eV, highlight the threefold symmetry of V/Cr *d* states and the sixfold symmetry of I *p* states. The energy in red in the top-right corner of each map pinpoints the binding energy of the isoenergetic cut. DFT calculation of the total energy map with contours shown as black lines for specific energies of VI_3; (g) 1.15 eV, (i) 2 eV, and CrI_3; (h) 2.3 eV, (j) 1.8 eV. Dashed lines in each image represent the 2D hexagonal first Brillouin zone. The energy in red in the top right corner of each map is the binding energy of the isoenergetic cut.
ARPES spectra of (k) VI_3 (T = 150 K, hν = 32 eV) and (l) CrI_3 (T = 300 K, hν = 32 eV) along the Γ-K direction. Theoretical band structures with FM configuration and SOC for VI_3 (GGA+U, U = 2 eV) and CrI_3 (bare GGA) monolayers are superimposed on experimental data. The colours highlighting the bands represent the following components: for V/Cr *d* orbital, red denotes $d_{3z2\text{-}r2}$, green denotes d_{xz} and d_{yz}, yellow denotes d_{xy} and $d_{x2\text{-}y2}$. For I *p* orbital, gray denotes p_x, magenta denotes p_y, blue denotes p_z. From (De Vita et al., 2022).

XAS spectra are intrinsically integrated over a thickness from 4 nm to 6 nm of material (Frazer et al., 2003), and as such they do not retain information coming from the very first layer of CrI_3 and VI_3.

For this reason, the direct surface analysis and investigation of the energy and the overall symmetry of the electronic states of VI_3 and CrI_3 was addressed by collecting k_x-k_y photoemission intensity maps at constant energy (see fig. 6.4c-f) and E vs k spectra (see fig. 6.4k-l). Experimental results were compared to DFT calculated electronic structures,[1] where the U value was changed in the range from 0 eV to 3 eV (De Vita et al., 2022) for both materials, seeking the best agreement with ARPES data.

Calculations were performed for the FM configuration, i.e. the magnetic ground state in monolayer form for VI_3 and CrI_3, both with and without SOC. The magnetisation direction, when SOC was included, was out-of-plane, consistently with the orientation of the magnetic moments. We note that our ARPES data were measured above the Curie temperature; nevertheless, a much better agreement is found with spin-polarized DFT, rather than with non-magnetic DFT calculations. The latter would in fact result in a metallic ground state, inconsistent with experimental results on these materials. Local magnetic correlations may actually occur even above the Curie temperature and this is implied by the good agreement of experimental data and spin-polarized DFT, even in the absence of long-range magnetic ordering.

Our experimental data show the existence of a sizeable bandgap for both systems, and allow us to evaluate the bandgap energies to be larger than 0.9 eV for VI_3 and 1.35 eV for CrI_3. These values have been obtained by comparing ARPES data, and in particular the valence band maximum, to the experimentally determined Fermi level.

It is important to underline that the experimental bandgap values are lower limits for the full bandgap, as ARPES detects occupied electron density of states (DOS) only; in addition, the presence of small charging effects of cleaved surfaces (J. Engelhardt, Dabringhaus and Wandelt, 2000; Harris and Fiasson, 1985; Wintle, 1997) cannot be excluded. The latter are common and well-understood in ARPES measurements of insulating compounds and can determine an artifactual rigid shift of the Fermi level of a few hundreds of millielectronvolts, without further changes in the band structure. As we already mentioned in section 6.4, sample charging due to excessive photon fluxes can be controlled and mitigated when necessary, so in this case it does not represent an issue.

We note that in this line of reasoning we cannot use DFT calculations for quantitative comparison, as the underestimate of band gaps is a well-known DFT problem in treating excited states (Giuliani and Vignale, 2005b). Nevertheless, a good agreement with previous experimental results is found, yielding a similar value obtained from optical measurements for CrI_3 (J. Dillon and C. Olson, 1965) and also both from optical (Son et al., 2019) and spectroscopic (Kundu et al., 2020) measurements for VI_3.

From fig. 6.4, we note that the overall electronic structures of VI_3 and CrI_3 show several similarities. In fact, the *3d* electronic states originating from V or Cr give rise to similar nearly-dispersionless features in the VB, whose intensity is prominent in the collected spectra (fig. 6.4k-l). On the other hand, the I-derived *5p* orbitals are very dispersive and the orbital-mixing is strong for both VI_3 and CrI_3. The orbital character of these bands, as inferred from DFT, shows that the SOC is crucial for explaining the observed energy-momentum spectra.

The effect of SOC modulates the band structure involving the V/Cr $d_{z2\text{-}3r2}$ and I p_x-

[1] Since vdW crystals are quasi-two-dimensional systems with weak interaction along the c-axis layer stacking direction, comparing experiments with theory for a single MI_3 layer is justified; therefore, calculations have been performed on a monolayer slab under a 20 Å vacuum layer. For further details on DFT methods, see (De Vita et al., 2022).

p_y orbitals at binding energies of ~ 1 eV in VI_3 and around 2.5 eV in CrI_3. Moreover, the inclusion of SOC is relevant in closing the gap between V a_{1g} and I p bands at Γ (De Vita et al., 2022).

Despite I p bands being fairly similar, our results show that VI_3 and CrI_3 behave in a different way from the electronic point of view. To emphasize this point, we carried out polarisation-dependent measurements on both compounds. p-polarised light has both in-plane and out-of-plane components of the wavevector with respect to the sample surface, whereas s-polarised light has only the in-plane component. By exploiting the light polarisation dependence we are thus selectively sensitive to in- and out-of- plane orbitals, as seen in fig. 6.5.

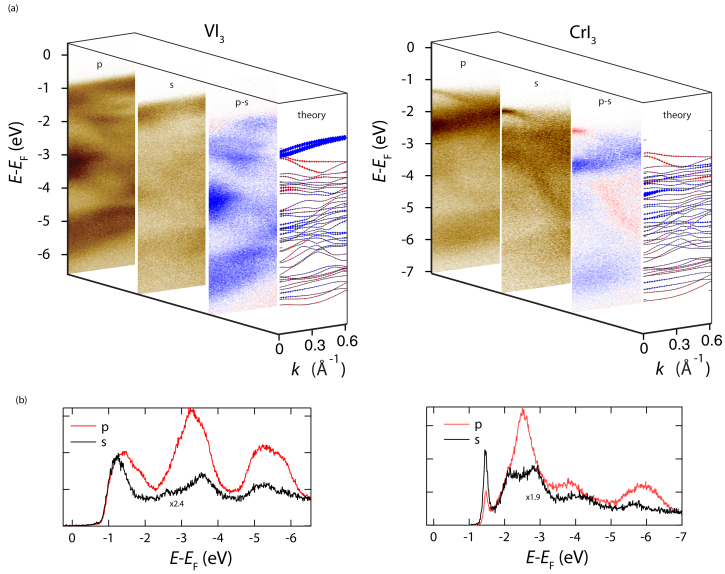

Figure 6.5: (a) VI_3 (left) and CrI_3 (right) spectra as a function of light polarization (p- polarization, s-polarization, difference p-s). p-polarized light has an out-of-plane component, while s-polarized light is completely in-plane. The "theory" panel displays the DFT band structure; a blue colour indicates bands with out-of-plane component, while a red colour emphasizes in-plane bands. (b) Angle-integrated spectra of VI_3 (left) and CrI_3 (right) evidencing polarization-dependent intensity of specific band features. From (De Vita et al., 2022).

For VI_3, we clearly see in fig. 6.5a that the orbitals contributing to the spectroscopic signal at ~ 1 eV are mostly out of plane, i.e. those with a_{1g} character. A value of U = 2 eV is thus found to best simulate our data. Higher values of U would shift the V a_{1g} states up towards the Fermi level, opening a gap between them and the I bands which is not observed in the experiment (De Vita et al., 2022). Lower values of U, instead, would place V d_{xz} and d_{yz} orbitals at an energy of ~ 1 eV, which is inconsistent with the data.

ARPES results for CrI_3 are in striking difference with those shown above for VI_3. First, from fig. 6.5a we deduce that bands at 2.5 eV BE are ascribed to the out-of-plane $d_{3z2\text{-}r2}$ orbitals. Second, we observe that, as soon as U values different from zero are introduced in the DFT calculations, those orbitals move to higher BEs (De Vita et al., 2022), a feature that is not observed by ARPES. This can be interpreted as follows. CrI_3

exhibits t_{2g} – e_g crystal-field splitting of *d* states; the different orbital filling of Cr^{3+} ions compared to V^{3+} results in a t_{2g} level completely filled by majority electrons. The orbital splitting between e_g and t_{2g} orbital states is sufficiently large in this case to stabilize a fully-insulating state, even in the absence of a finite U-value within the DFT+U approach.

Another relevant difference between the two compounds is that DFT calculations compare well with ARPES spectra, with the exception of the a_{1g} orbital filling of VI_3. The a_{1g} are clearly revealed as filled states by ARPES, whilst are predicted to be empty by DFT consistently with a V^{3+} ionic charge. On top of this, XAS results also indicate a V^{3+} valency of the bulk.

This peculiar behaviour is nevertheless clearly revealed by ARPES, which probes just the topmost layer of the material, therefore including intrinsic and extrinsic surface effects like relaxation and defect-doping effects that can be responsible of the local electron filling of the a_{1g} band. We thus suggest that a different ground state, characterized by a V^{2+} orbital filling, stabilizes at the surface: it turns out that the gap between filled and empty states observed in ARPES measurements is opened by the octahedral crystal field, rather than that by the bulk trigonal crystal field splitting of a1g and eg' levels. On the other hand, CrI_3 does not show any evidence of a different surface electronic environment.

In fig. 6.4c-f, we note that the constant energy ARPES maps for VI_3 and CrI_3 display a different symmetry in connection with the orbital character of the electronic states. I *5p* states display an apparent sixfold symmetry, while V and Cr *3d* states show a threefold symmetric pattern, differently from DFT results (reported in fig. 6.4g-j). The threefold symmetry of V *3d* states is highlighted also in fig. 6.6.

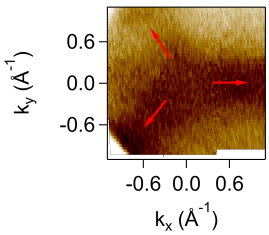

Figure 6.6: ARPES $k_x - k_y$ isoenergetic map on VI_3 at ($h\nu$ = 80 eV, T = 150 K) at 1.15 eV BE. The red arrows highlight the threefold symmetry of the V band.

Indeed, the expected trigonal symmetry is not necessarily reproduced in our single-layer calculations, since the primitive cell encompasses two layers. In previous works, it has been suggested that such a pattern could be connected with the onset of the ferromagnetic ground state (Kundu et al., 2020), that breaks time-reversal symmetry when VI_3 undergoes the magnetic transition. At the surface, this combines with the loss of inversion symmetry, giving rise to a P-T symmetry-breaking system.

Our ARPES data (150 K for VI_3, 300 K for CrI_3) were collected at sample temperatures well above the Curie point (CrI_3: $T_{C,CrI3}$ = 61 K, VI_3: $T_{C,VI3}$ = 50 K), and suggest a different interpretation with respect to the one given in (Kundu et al., 2020).

The reduction of symmetry of ARPES constant energy maps with respect to DFT results may be ascribed to surface effects, that are not accounted for in the DFT simulations of VI_3 and CrI_3 single-layers (i.e. not for semi-infinite crystals). However, we cannot rule out the existence of magnetic fluctuations and their role in breaking time-reversal symmetry.

The relevance of short-range magnetic interactions in vdW magnetic materials, including VI_3, has been pointed out by numerous studies (McGuire, Clark et al., 2017; M. Suzuki et al., 2019; Tian et al., 2019; Zeisner, Alfonsov et al., 2019; Zeisner, Mehlawat et al., 2020). Well above the Curie temperature, thermal fluctuations randomly orient the electron spins in the valence band, but the nonmagnetic ground state can be locally

described in terms of orbital filling of the TM states by majority electrons.

The occurrence of magnetic fluctuations above the Curie point in the absence of long-range order is well-documented for correlated materials [39-41]; the observed narrow bandwidth of V- and Cr-derived *3d* bands hints at the importance of electron-electron interactions as well. Furthermore, V- and Cr- projected states would be more affected by short-range correlation effects, whilst the I contribution to the magnetic moment is negligible (He et al., 2016), leaving the symmetry of I *5p* states as dictated by the structure.

The intra-layer atomic arrangement does not change even at the structural transition that both crystals undergo at $T_{S,CrI3} = 220$ K and $T_{S,VI3} = 78$ K, involving only layer stacking. The comparison of calculations and surface-sensitive experimental data allows us to conclude that the band structure is largely unaffected across the structural transitions.

6.6 Probing orbital character and dimensionality with ResPES

The use of ResPES allows to exploit the selective abrupt changes of photoionization cross sections in order to identify the orbital contributions to the spectra. V *3d* orbitals contributing to the bands at 1 eV BE, and similarly Cr *3d* orbitals contributing to the bands at 2.5 eV BE, are resonantly enhanced when the photon energy reaches the photoionization threshold of the V and Cr *3p* core levels, respectively. In this way we experimentally probe the atomic character of the wavefunctions contributing to ARPES intensities.

The large signal enhancement of the non-dispersing bands when the photon energy coincides with the *3p* edges (fig. 6.7a,c) is a direct signature of their V/Cr orbital nature, and can be mapped onto the DFT orbital projection of the DOS (fig. 6.7b,d).

Photon energy dependent ARPES, such as ResPES, intrinsically also probes the k_z dispersion. The absence of dispersion of both V and Cr projected bands, highlighted by the EDC spectra (fig. 6.7a-c, right panel), indicates that those states are "2D-like" with negligible interlayer interaction (assuming no artifacts are introduced by rescaling the spectra to compensate charging effects). The consistency of ARPES results with single-layer calculations appears therefore strengthened.

The claim that electronic states in VI_3 mostly show a two-dimensional nature can be further supported by directly showing the k_z band dispersion. Figure fig. 6.8 exemplifies this point for VI_3: bands are mostly flat across the probed k_z range. We chose to display the cut at $k_z = 0.33$ Å^{-1} in order to clearly separate the two I-derived bands around 2 eV BE: notably, we see how the topmost band is slightly dispersing in k_z, whereas the lower one is totally flat.

Across this photon energy interval, almost the entirety of the Brillouin zone is scanned (Fig. fig. 6.8b).

6.7 Magnetic character of VI_3 by XMCD

In its ground state at low temperatures, VI_3 is ferromagnetic, with magnetic moments perpendicular to the atomic planes (Gati et al., 2019; Son et al., 2019; Tian et al., 2019). The ferromagnetic behaviour is expected to be found even down to the monolayer limit, similarly to what has been observed for other halides.

A legit question would be asking what is the universality class of the ferromagnetic ordering in VI_3. The ordered arrangement between neighbouring magnetic moments at low temperature is gradually destroyed by the increasing temperature: long-range fluctuations, created with a certain energy cost, are increasingly favoured by the increase in entropy. The circumstances in which the competition between energy and entropy

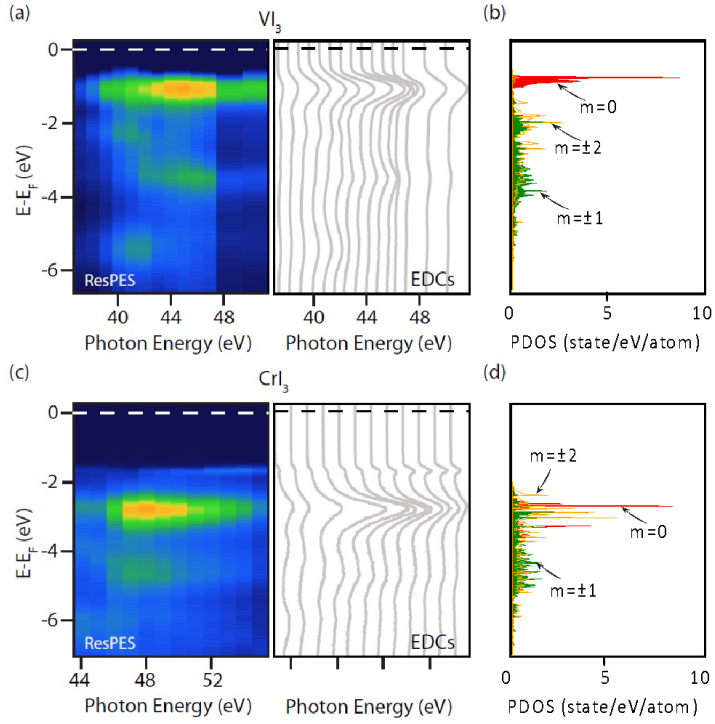

Figure 6.7: (a) ResPES in the first BZ for VI_3: the colour map – *left panels* – displays the momentum-integrated photoemission intensity; the resonant EDCs – *right panels* – emphasise the band dispersion (or lack of) along the measured photon energy. (b) d-orbital projection DOS of VI_3; the colour scale represents *d* orbital characters as follows: filled red: m = 0, filled green: m = 1, orange: m = 3. (c-d) Same as (a-b), but for CrI_3. From (De Vita et al., 2022).

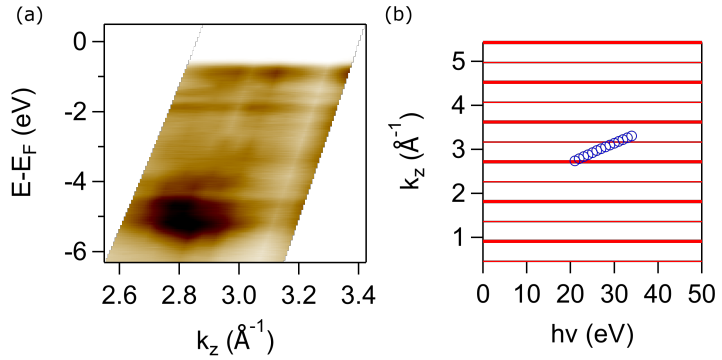

Figure 6.8: (a) k_z dispersion of the valence band structure of VI_3 (k_x = 0.33 eV, in order to clearly discern the I-derived bands around 2 eV BE). (b) Calculated k_z as a function of the photon energy scanned in our experiments on VI_3. Thick red lines represent the borders of Brillouin zones along k_z. We considered an inner potential of V_0 = 15 eV. From (De Vita et al., 2022).

determines the qualitative nature of the critical behaviour are determined by the dimensionality of the lattice and the degrees of freedom of the spin system. Identifying in the V magnetic moment the order parameter (and in the external magnetic field H_{ext} the ordering field), it is possible to study the criticality of the material in the neighbourhood of T_C.

At low temperatures, we were not able to directly access photoelectrons and using Spin-ARPES to assess the spin polarisation of the electronic bands, due to sample charging effects becoming too extreme below 100 K. However, we can access the average spin magnetic moment of the *3d* states via XMCD.

6.7.1 Data acquisition and analysis

The measurements were performed at the XMCD endstation of the ID32 soft X-ray beamline at the European Synchrotron Radiation Facility (ESRF) in Grenoble. A commercial (HQGraphene) bulk VI_3 crystal was mounted on the copper ID32 special holder using carbon tape and then cleaved in the load-lock chamber under N_2 pressure before being transferred in UHV, to expose a clean surface.

As for ARPES, since the material is extremely hygroscopic the whole sample preparation and transfer to the end-station were carried out under nitrogen inert atmosphere, *i.e.* the first inside a N_2 glovebox, the second using an air-tight transfer box. Measurements have been performed in the 4 K-100 K range in a background pressure lower than 3×10^{-10} mbar, using circular (right-hand, CR, and left-hand, CL) polarised light, depending on the specific technique. The beam has a degree of linear polarisation of almost 100 % and the setup has resolving power better than 5000. The signal was measured in total electron yield (TEY) mode and normalised by the intensity collected by a gold mesh placed before the sample stage. All measurements have been performed with an applied field H_{ext} = 2 T unless specified otherwise (*e.g.* in a histeresis cycle).

Since a drift in the background is generally unavoidable, we performed XMCD measurements alternating light polarisation. We acquired sets of XAS spectra at opposite polarisations along the scheme "CR-CL-CL-CR", and then averaged over measurements with the same polarisation: potential drifts are therefore cancelled out. Each set comprised 16 acquisitions, *i.e.* 4 for each light polarisation.

We calculated the XMCD by dividing spectra by the maximum of the sum of both polarisations, and then computing the difference between CR and CL polarisations. Experimental errors on XMCD are determined by the repeatability of XAS spectra during an experimental run. To estimate the error on the evaluation of the XMCD, we singled out pairs of XAS curves at opposite polarisations, calculated the XMCD and obtained a set of XMCD curves at each temperature; we then evaluated the variance of the dichroism and we used that value as error of the XMCD calculated from the averaged curves.

6.7.2 Results

The VI_3 XAS spectra have already discussed in previous sections: two main peaks at 515.4 eV and 522.2 eV are measured, corresponding to the L_3 and L_2 edges, and the lineshape is characterised by a multiplet structure due to crystal field and other interactions, with the characteristic ${t_{2g}}^3$ transitions in the pre-edge region.

Right and left circularly polarised light generate different XAS white lines below the Curie temperature T_C = 50 K, as seen in fig. 6.9a-b, giving rise to a sizeable dichroism (in the order of 15-20 % at the main peak of the L_3 edge). The lineshape of the dichroism is consistent with other examples in (Maganas et al., 2020; Schmitz et al., 2020; Vinai et al.,

2020) and references therein. The dichroism decreases when the temperature increases, and is reduced to negligible magnitude at 70 K (fig. 6.9c); a small residual signal may be expected due to the presence of H_{ext} forcing a small magnetic moment even in the paramagnetic phase.

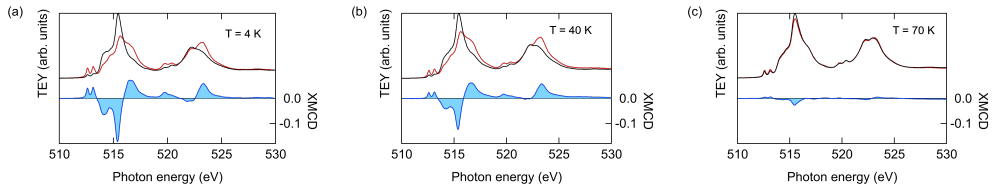

Figure 6.9: Experimental XAS spectra and corresponding XMCD curves of VI_3 at the V $L_{2,3}$ edges measured in the ferromagnetic (a-b) and paramagnetic (c) phases. XAS spectra taken with left-hand and right-hand circular polarisation are respectively in black and red, while the XMCD signal is in blue.

We may note that the dichroism at 4 K and 40 K do not display major dissimilarities. (Gati et al., 2019) found a second ferromagnetic transition at $T_{C,2} = 36$ K, attributed by NMR to the ordering of two different V sites (compared to a single V site with ordered magnetic moments above $T_{C,2}$).

Our XMCD data do not suggest the onset of such a variance in the ferromagnetic ordering, as the lineshape of the dichroic signal shows no qualitative difference in a comparison between fig. 6.9a-b. Interestingly, the separation between the two transitions studied in (Gati et al., 2019) disappears when an external pressure above 0.6 GPa is applied. We conclude that the presence of a strong external magnetic field in our measurements forces the system in a region of the phase space where the two transitions are not distinct; this is also consistent with the magnetometry measurements of (Tian et al., 2019), where a kink in the magnetisation curve disappears at $H_{ext} = 5$ T. We may hypothesise that this correspondence between external pressure and external magnetic field in the VI_3 phase diagram emerges due to strong coupling of structural and magnetic degrees of freedom in this material.

We also performed element-sensitive hysteresis loop at 4 K at the same V edges, by selecting the L_3 edge and scanning the magnitude of the magnetic field in the range from –3 T to 3 T, as shown in fig. 6.10.

At this temperature, VI_3 presents a coercive field of ~ 0.6 T and a ratio of remanence magnetisation over saturation magnetisation of ~ 90 %: this clearly indicates ferromagnetic behaviour and ensures that a $H_{ext} = 2$ T field completely saturates the magnetic moments.

As already mentioned, the XAS lineshape suggests a V^{3+} valence state. The absolute value of the spin magnetic moment is expected to be given by $\mu_s = g\sqrt{s(s+1)}\mu_B$; the prefactor of the Bohr magneton, determined by the Hund's rules, is determined by the V^{3+} high spin $s = 1$ configuration, and the resulting expected value of the magnetic moment is $\mu_0 = 2.84\mu_B$.

The extraction of the spin magnetic moment via sum rules in light transition metals is known to warrant additional care. The application of sum rules requires L_3 and L_2 edges to be pure in their $2p_{3/2}$ and $2p_{1/2}$ nature, without mixing by multiplet effects, and clearly separable (De Groot and Kotani, 2008); in general, vanadium is not an ideal system in this regard, due to the small spin-orbit splitting and the resulting mixture of $2p_{3/2}$ and $2p_{1/2}$ characters. In any case, by considering data at 4 K, we obtain $\mu_{s,eff} \approx$

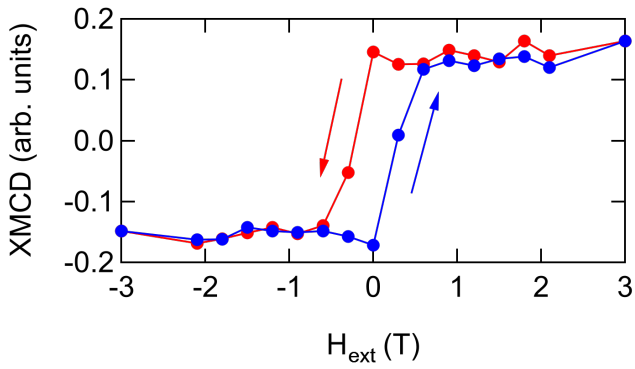

Figure 6.10: Hysteresis loop of the XMCD signal on VI_3 at the V $L_{2,3}$ edges, at T = 4 K.

2.9(2)μ_B, which is in line with theoretical predictions of a fully saturated saturated spin magnetic moment.

The behaviour of the V spin magnetic moment as a function of the temperature across the ferromagnetic transition may thus be computed in units of μ_0, as in fig. 6.11. In the graph, three additional curves have been drawn to represent the temperature behaviour of the magnetisation following mean field theory (MFT), the 2D XY model and the 2D Ising model.

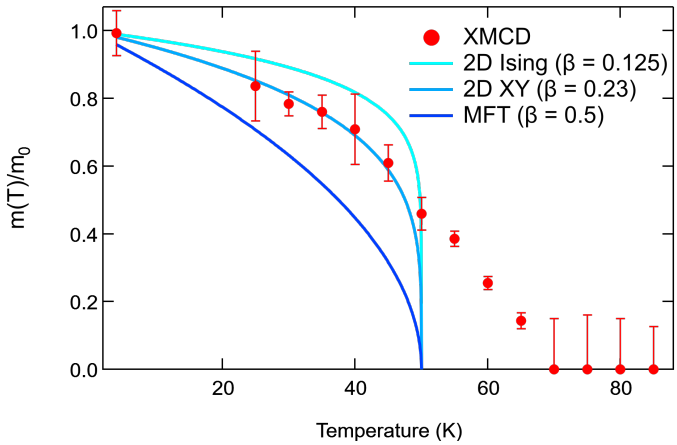

Figure 6.11: Temperature dependence of the average V^{3+} magnetic moment in VI_3 (H_{ext} = 2 T). Expected behaviour of the magnetic moment in case of 2D Ising, 2D XY and 3D MFT universality classes are also displayed.

The permanence of a dichroic signal above T_C is again attributable to the external magnetic field, as testified also in (Tian et al., 2019), because of the additional energy supplied to the spin system opposing the spin fluctuations induced by entropy. Below T_C, where VI_3 is ferromagnetic, the paramagnetic contribution should be relatively small.

We can immediately notice that the behaviour near the critical point conflicts with both classical mean field theory ($\beta = 0.5$) and 2D Ising-type interaction ($\beta = 0.125$). A fitting of experimental data below T_C finds the critical exponent $\beta = 0.21(2)$, which is close to the 2D XY model (S. Bramwell and P. Holdsworth, 1993): VI_3 seems incompatible with isotropic 3D ferromagnetism (represented by the MFT curve) and with strict 2D ferromagnetism with out-of-plane spins (represented by the Ising-type curve), exhibiting instead a "hybrid" behaviour, indicative of a crossover between 2D and 3D properties.

If we compare this result with other halides, we see that a vast phenomenology in the effect of dimensionality has been discovered.

$CrBr_3$ displays $\beta = 0.37$ (M. Kim et al., 2019); this means that a 2D Ising model describes this system rather poorly, whereas the anisotropic Heisenberg model (XXZ) is much more suited. Interestingly, T_C only weakly depends on the number of layers, and the value of β for a monolayer is compatible with the value obtained for bulk $CrBr_3$ (Ho and Litster, 1969). The XXZ model has been proposed also for CrI_3 and $CrGeTe_3$: the physical origin of this behaviour has been ascribed to the strength of SOC in the heavy ligands, giving rise to a superexchange mechanism between metallic centres mediated by I or Te (C. Xu et al., 2018). These materials thus show a more pronounced 3D behaviour, which has also been demonstrated by a relatively high exfoliation energy for the standard of van der Waals crystals (Yan et al., 2019).

Conversely, Fe_3GeTe_2 exhibits a strong dependence on the thickness: the critical exponent β in the range from 0.25 to 0.27 above 5 nm thickness rapidly decreases and approaches 0.14(2) for a monolayer (Zaiyao et al., 2018). Another case is the XMCD study on a $CrCl_3$ monolayer in (Bedoya-Pinto et al., 2021), where $\beta = 0.227(21)$ indicates that this material can be described by the 2D XY model. VI_3 seems to lay within this second category: magnetometry measurements have also revealed that bulk VI_3 approaches criticality with $\beta = 0.244(2)$ (Y. Liu, Abeykoon and Petrovic, 2020).

The distribution of the critical exponent β for 2D systems has been proven to be in the range of $0.1 < \beta < 0.25$ (Taroni, S. T. Bramwell and P. C. W. Holdsworth, 2008). Given this context, we may ascertain that VI_3 displays strong 2D character; VI_3 belongs therefore to the universality class of 2D systems with easy-plane anisotropy (spin dimensionality n = 2), and in particular a strong out-of-plane anisotropy giving rise to a magnetic moment along the *c* axis, exemplified by a 2D XY model. The strong electron confinement on 2D planes even in the bulk crystal is already suggested by the presence of an on-site Coulomb energy correction in DFT calculations (section 6.5), hinting at relevant electronic correlations within layers.

6.8 Closing remarks

In the previous sections, we characterised the ground state electronic structure of CrI_3 and VI_3: based on the excellent agreement between photoemission data (angle-resolved, light polarisation-dependent and resonant) and DFT-calculated band dispersion and orbital-resolved density of states, we give evidence of how substantially different can be the orbital configuration of magnetic trihalides for different TM ions.

We observe that CrI_3 shows a three-fold t_{2g} orbital degeneracy with a wide bandgap opening between majority spin e_g and t_{2g} states, whilst VI_3 shows a Mott-insulator-like ground state with (filled) e'_g - (empty) a_{1g} orbital splitting and a narrower bandgap.

Single-layer band structure calculations compare well with ARPES spectra, suggesting a reduced importance of interlayer electronic interactions in determining the stable ground state configuration, including between the surface layer and the bulk. Moreover,

comparison of surface-sensitive (ARPES) and bulk-sensitive (XAS) measurements in VI_3 supports the occupancy of the a_{1g} state at the surface of VI_3.

This fact is interpreted in view of the stabilisation of a different ground state at the surface, characterised by an unconventional V^{2+} valence state and an occupied a_{1g} band, at variance with the V^{3+} bulk valency. This suggests that that ground state electronic properties, and orbital filling in particular, are strongly influenced by dimensionality effects.

Said dimensionality effects clearly emerge also when looking at the magnetic degrees of freedom. Element-sensitive XMCD reveal ferromagnetic order on V up to the Curie temperature, without evidence of a second ferromagnetic transition due to the constraint of H_{ext}; the behaviour near criticality, suggestive of a universality class with n = 2 character, points at a crossover from 3D to 2D properties, differently from CrI_3. We may suggest this variation comes from a higher orbital confinement, resulting in increased on-site electron-electron correlations as postulated by DFT calculations.

Future research in ultrathin films or nanoparticles of MI_3 van der Waals materials, with variable surface to bulk ratios, should carefully explore the effective ionic configurations that determine their electronic properties. Pushing towards the monolayer limit may attain a crossover to Ising-type (uniaxial anisotropy) behaviour, which would be crucial for heterostructure engineering and related potential functionalities.

Conclusions and future directions

Objectives

In this thesis I explored the properties of systems exhibiting ferromagnetic behaviour and ideally aimed at novel functionalities to enhance speed and efficiency of modern devices. I focused on the characterisation of their electronic properties with resolution to the spin degree of freedom, in order to access the information retained by band electrons.

Case studies and results

The systems of choice were Fe(001)-p(1x1)O/MgO , $EuSn_2P_2$ and MI_3 (M = Cr,V), by virtue of their differences in dimensionality. I employed a wide number of experimental techniques to directly access electron states and investigate their spin. The main spectroscopic method that I adopted was ARPES, a powerful technique to assess the dispersion of the valence band. Combining ARPES with other spectroscopies based on core-level absorption (XAS, XMCD) and/or spin (Spin-ARPES) or time (TR-polarimetry) resolution allowed for a diversified characterisation, always grounded on the structure of electronic bands.

ARPES measurements determined the structure of the near-Fermi region of the valence band in Fe(001)-p(1x1)O/MgO . This information has been used to identify the electronic states that are accessed by threshold photons ($h\nu$ = 4.8 eV), which revealed a high (57(5) %) spin polarisation. I was able to access the in-band spin polarisation of bulk states, unaffected by the surface: indeed, threshold photoemission selects very low energy photoelectrons with long mean free path and low scattering probability from a specific region in the Brillouin zone.

Employing the same threshold photons as probe, I studied the ultrashort response of this spin polarisation signal when the system is brought out of equilibrium by an 800 nm ultrashort laser pulse: I found that the quenching of the spin polarisation is driven by the energy exchange between the electron and spin reservoirs leading to phonon-mediated electron scattering, whereas carriers redistribution and superdiffusive spin currents play a minor role. The low pump fluence allowed to study a regime where there is no collapse of the exchange splitting, and the dynamics of the spin polarisation is instead dominated by Elliot-Yafet-type spin-flip scattering; by means of a microscopic model, I extracted the quantities governing this process and found good consistency with expected results.

ARPES spectra were also the first ingredient in revealing the termination-dependent behaviour of electronic states in $EuSn_2P_2$: I found that only the P-terminated surface hosts linearly-dispersing bands, which are well-separated from the localised Eu *4f* electrons. The magnetic ordering in $EuSn_2P_2$ below the Néel temperature is completely

Eu-derived, with in-plane magnetic moments and antiferromagnetic coupling between layers, as revealed by XMCD and Spin-ARPES. A direct assessment of the spin polarisation of the P-derived surface states finds opposite sign of the spin polarisation at opposite *k*-space points; this behaviour is independent of the temperature, confirming their topological nature due to spin-momentum locking arguments.

In MI_3 , the characterisation of the valence band by ARPES pinpoints the key differences in band ordering and correlation degree between the transition metals (V or Cr): CrI_3 t_{2g} states are threefold-degenerate with a wide bandgap, whereas VI_3 shows a Mott insulating state with an e'_g-a_{1g} orbital splitting. I also located an unorthodox V^{2+} valence state at the surface of VI_3, thanks to resonant photoemission confirming the orbital character of the valence band maximum. A further inquiry on the V magnetic moment in VI_3 by XMCD below the Curie temperature and near criticality suggests that this material belongs to the universality class n = 2, *i.e.* displays a strong 2D character, at variance with CrI_3.

Significance

Environments with reduced dimensionality are a thriving and ever-expanding topic due to their potential in technological applications. Modern devices based on CMOS logic have reached a degree of miniaturisation to the point that effects of surface and dimensionality on stability, efficiency and energy consumption cannot be ignored.

Rather than trying to mitigate these effects, an exploration of the role of electron spatial confinement marks a change in paradigm. As a matter of fact, research is pushing towards alternative solutions; new quantum phenomena are already being exploited (see the Introduction and the literature therein cited); magnetism in its more unconventional forms is being harnessed for giving rise to novel properties.

For these reasons, the focus of any work that aims at a buildup of a new standard in magnetic storage and computation should fully embrace the shift away from pure 3D properties by deliberately tackling systems with $D < 3$. My research fits well in the need for an in-depth investigation of materials with different degree of spatial confinement, thanks to their potential technological relevance. The renowned motto "There's plenty of room at the bottom" by Richard Feynman can easily be adapted in view of the search for applications not only at a reduced size, but also at reduced dimensionality.

Outlook

What can we imagine about future advances in this field of research, starting from the work of this thesis?

The exciting perspective of axion physics in solid state physics should trigger the passage of materials such as $EuSn_2P_2$ to the testing ground of device fabrication. Within thir peculiar name is hidden the true strength of these systems. The name *axion*, from a popular detergent in the US during the 1950s, has been given by F. Wilczek to the hypothetical particle "since they clean up a problem with axial current.[2]" Much like modern commercial detergents, axion insulators exhibit "3 in 1" functionalities, thanks to the interplay between magnetism, topology and spin-orbit coupling. The key challenge in this case would be twofold, to achieve control on these properties and discern their different contributions to *e.g.* spin-to-charge current conversion or magnetoelectric effects.

In terms of applications of van der Waals materials, the drive towards the monolayer limit implies many future possibilities offered to technological applications. Not only

[2] F. A. Wilczek, *Asymptotic Freedom: From Paradox to Paradigm* (2004).

in 2D can we induce a phenomenology unheard of in the 3D world; the combination of different 2D layers with different properties may create unique physical effects. 2D materials are effectively powerful building blocks whose versatility calls for channeling their properties for heterostructures. Curiously enough, the *top-down* approach in characterising 2D materials should be replaced with a *bottom-up* method back to 3D-like structures, but with engineered properties directly inherited from the 2D nature of their constituent "Lego bricks".

Lastly, we can certainly forecast a fruitful development in the time-resolved department. Any study looking for solutions in magnetic storage should emphasise the role of electron dynamics and the interactions of energy reservoirs in determining transient states and the following relaxation to the ground state. Studying the ultrafast response to excitations in a pump-probe framework constituted a part of my work on Fe(001)-p(1x1)O/MgO ; this characterisation should hopefully be extended to the other systems presented here, as well as to those parent compounds that exhibit increased dimensionality effects.

All in all, many technical and conceptual challenges are waiting in line before the full integration in a device of the systems and physical phenomena presented in this thesis. However, the countless possibilities that are offered by moving towards the 2D limit will at some point permit us to circumvent those obstacles; in the end, the desire for exploring the plethora of novel effects and functionalities is the only true limit posed ahead of us.

Bibliography

Aeschlimann, M., M. Bauer, S. Pawlik, W. Weber, R. Burgermeister, D. Oberli and H. C. Siegmann (1997). 'Ultrafast Spin-Dependent Electron Dynamics in fcc Co'. In: *Phys. Rev. Lett.* 79 (25), pp. 5158–5161.

Aeschlimann, M., C. A. Schmuttenmaer, H. E. Elsayed-Ali, R. J. D. Miller, J. Cao, Y. Gao and D. A. Mantell (1995). 'Observation of surface enhanced multiphoton photoemission from metal surfaces in the short pulse limit'. In: *The Journal of Chemical Physics* 102.21, pp. 8606–8613.

Afanasiev, D., J.R. Hortensius, B.A. Ivanov, A. Sasani, E. Bousquet, Y.M. Blanter, R.V. Mikhaylovskiy, A.V. Kimel and A.D. Caviglia (2021). 'Ultrafast control of magnetic interactions via light-driven phonons'. In: *Nature Mater.* 20 (5), pp. 607–611.

Alford, T.L., L.C. Feldman and J.W. Mayer (2007). *Fundamentals of Nanoscale Film Analysis*. Springer New York. ISBN: 978-0-387-29260-1.

Allaria, E., D. Castronovo, P. Cinquegrana, P. Craievich, M. Dal Forno, M.B. Danailov, G. D'Auria, A. Demidovich, G. De Ninno, S. Di Mitri, B. Diviacco, W.M. Fawley, M. Ferianis, E. Ferrari, L. Froehlich, G. Gaio, D. Gauthier, L. Giannessi, R. Ivanov, B. Mahieu, N. Mahne, I. Nikolov, F. Parmigiani, G. Penco, L. Raimondi, C. Scafuri, C. Serpico, P. Sigalotti, S. Spampinati, C. Spezzani, M. Svandrlik, C. Svetina, M. Trovo, M. Veronese, D. Zangrando and M. Zangrando (2013). 'Two-stage seeded soft-X-ray free-electron laser'. In: *Nature Photon.* 7, pp. 913–918.

Anderson, Nathaniel A., Myron Hupalo, David Keavney, Michael C. Tringides and David Vaknin (2017). 'Intercalated europium metal in epitaxial graphene on SiC'. In: *Phys. Rev. Materials* 1 (5), p. 054005.

Ando, Yoichi (2013). 'Topological Insulator Materials'. In: *Journal of the Physical Society of Japan* 82.10, p. 102001.

Anisimov, S. I., B. L. Kapeliovich and T. L. Perel'Man (1974). 'Electron emission from metal surfaces exposed to ultrashort laser pulses'. In: *Soviet Journal of Experimental and Theoretical Physics* 39, pp. 375–377.

Arguilla, M. Q., N. D. Cultrara, Z. J. Baum, S. Jiang, R. D. Ross and J. E. Goldberger (2017). 'EuSn2As2: an exfoliatable magnetic layered Zintl–Klemm phase'. In: *Inorg. Chem. Front.* 4 (2), pp. 378–386.

Armitage, N.P. and L. Wu (2019). 'On the matter of topological insulators as magnetoelectrics'. In: *SciPost Phys.* 6 (4), p. 46.

Battiato, M., K. Carva and P. M. Oppeneer (2010). 'Superdiffusive Spin Transport as a Mechanism of Ultrafast Demagnetization'. In: *Phys. Rev. Lett.* 105 (2), p. 027203.

Beaurepaire, E., J.-C. Merle, A. Daunois and J.-Y. Bigot (1996). 'Ultrafast Spin Dynamics in Ferromagnetic Nickel'. In: *Phys. Rev. Lett.* 76 (22), pp. 4250–4253.

Bedoya-Pinto, Amilcar, Jing-Rong Ji, Avanindra K. Pandeya, Pierluigi Gargiani, Manuel Valvidares, Paolo Sessi, James M. Taylor, Florin Radu, Kai Chang and Stuart S. P. Parkin (2021). 'Intrinsic 2D-XY ferromagnetism in a van der Waals monolayer'. In: *Science* 374.6567, pp. 616–620.

Berglund, C. N. and W. E. Spicer (1964). 'Photoemission Studies of Copper and Silver: Theory'. In: *Phys. Rev.* 136 (4A), A1030–A1044.

Bertacco, R., M. Marcon, G. Trezzi, L. Duò and F. Ciccacci (2002). 'Spin and energy analysis of electron beams: Coupling a polarimeter based on exchange scattering to a hemispherical analyzer'. In: *Review of Scientific Instruments* 73.11, pp. 3867–3871.

Bertacco, Riccardo and Franco Ciccacci (1999). 'Oxygen-induced enhancement of the spin-dependent effects in electron spectroscopies of Fe(001)'. In: *Phys. Rev. B* 59 (6), pp. 4207–4210.

Beuneu, F. and P. Monod (1978). 'The Elliott relation in pure metals'. In: *Phys. Rev. B* 18 (6), pp. 2422–2425.

Bigi, Chiara, Pranab K. Das, Davide Benedetti, Federico Salvador, Damjan Krizmancic, Rudi Sergo, Andrea Martin, Giancarlo Panaccione, Giorgio Rossi, Jun Fujii and Ivana Vobornik (2017). 'Very efficient spin polarization analysis (VESPA): new exchange scattering-based setup for spin-resolved ARPES at APE-NFFA beamline at Elettra'. In: *Journal of Synchrotron Radiation* 24.4, pp. 750–756.

Bigot, Jean-Yves, Mircea Vomir and Eric Beaurepaire (2009). 'Coherent ultrafast magnetism induced by femtosecond laser pulses'. In: *Nature Phys.* 5, pp. 515–520.

Blackburn, L.D, Larry Kaufman and Morris Cohen (1965). 'Phase transformations in iron-ruthenium alloys under high pressure'. In: *Acta Metallurgica* 13.5, pp. 533–541. ISSN: 0001-6160.

Bormann, R., M. Gulde, A. Weismann, S. V. Yalunin and C. Ropers (2010). 'Tip-Enhanced Strong-Field Photoemission'. In: *Phys. Rev. Lett.* 105 (14), p. 147601.

Bramwell, S.T. and P.C.W. Holdsworth (1993). 'Magnetization and universal sub-critical behaviour in two-dimensional XY magnets'. In: *Journal of Physics: Condensed Matter* 5.4, pp. L53–L59.

Brookes, N.B., F. Yakhou-Harris, K. Kummer, A. Fondacaro, J.C. Cezar, D. Betto, E. Velez-Fort, A. Amorese, G. Ghiringhelli, L. Braicovich, R. Barrett, G. Berruyer, F. Cianciosi, L. Eybert, P. Marion, P. van der Linden and L. Zhang (2018). 'The beamline ID32 at the ESRF for soft X-ray high energy resolution resonant inelastic X-ray scattering and polarisation dependent X-ray absorption spectroscopy'. In: *Nuclear Instruments and Methods in Physics Research Section A: Accelerators, Spectrometers, Detectors and Associated Equipment* 903, pp. 175–192.

Bühlmann, K., G. Saerens, A. Vaterlaus and Y. Acremann (2020). 'Detection of femtosecond spin voltage pulses in a thin iron film'. In: *Structural Dynamics* 7.6, p. 065101.

Butler, S.Z., S.M. Hollen, L. Cao, Y. Cui, J.A. Gupta, H.R. Gutiérrez, T.F. Heinz, S.S. Hong, J. Huang, A.F. Ismach, E. Johnston-Halperin, M. Kuno, V.V. Plashnitsa, R.D. Robinson, R.S. Ruoff, S. Salahuddin, J. Shan, L. Shi, M.G. Spencer, M. Terrones, W. Windl and J.E. Goldberger (2013). 'Progress, challenges, and opportunities in two-dimensional materials beyond graphene'. In: *ACS Nano* 7 (4), pp. 2898–2926.

Cacho, C., A. Crepaldi, M. Battiato, J. Braun, F. Cilento, M. Zacchigna, M. C. Richter, O. Heckmann, E. Springate, Y. Liu, S. S. Dhesi, H. Berger, Ph. Bugnon, K. Held, M. Grioni, H. Ebert, K. Hricovini, J. Minár and F. Parmigiani (2015). 'Momentum-Resolved Spin Dynamics of Bulk and Surface Excited States in the Topological Insulator Bi_2Se_3'. In: *Phys. Rev. Lett.* 114 (9), p. 097401.

Caputo, M., J. Jandke, E. Cappelli, S.K. Chaluvadi, E. Bonini Guedes, M. Naamneh, G. Vinai, J. Fujii, P. Torelli, I. Vobornik, A. Goldoni, P. Orgiani, F. Baumberger, M. Radovic

and G. Panaccione (2022). 'Metal to insulator transition at the surface of V2O3 thin films: An in-situ view'. In: *Applied Surface Science* 574, p. 151608. ISSN: 0169-4332.

Carpene, E., H. Hedayat, F. Boschini and C. Dallera (2015). 'Ultrafast demagnetization of metals: Collapsed exchange versus collective excitations'. In: *Phys. Rev. B* 91 (17), p. 174414.

Carpene, E., E. Mancini, C. Dallera, M. Brenna, E. Puppin and S. De Silvestri (2008). 'Dynamics of electron-magnon interaction and ultrafast demagnetization in thin iron films'. In: *Phys. Rev. B* 78 (17), p. 174422.

Carra, Paolo, B. T. Thole, Massimo Altarelli and Xindong Wang (1993). 'X-ray circular dichroism and local magnetic fields'. In: *Phys. Rev. Lett.* 70 (5), pp. 694–697.

Castán-Guerrero, C., D. Krizmancic, V. Bonanni, R. Edla, A. Deluisa, F. Salvador, G. Rossi, G. Panaccione and P. Torelli (2018). 'A reaction cell for ambient pressure soft x-ray absorption spectroscopy'. In: *Review of Scientific Instruments* 89.5, p. 054101.

Chang, Cui-Zu, Jinsong Zhang, Xiao Feng, Jie Shen, Zuocheng Zhang, Minghua Guo, Kang Li, Yunbo Ou, Pang Wei, Li-Li Wang, Zhong-Qing Ji, Yang Feng, Shuaihua Ji, Xi Chen, Jinfeng Jia, Xi Dai, Zhong Fang, Shou-Cheng Zhang, Ke He, Yayu Wang, Li Lu, Xu-Cun Ma and Qi-Kun Xue (2013). 'Experimental Observation of the Quantum Anomalous Hall Effect in a Magnetic Topological Insulator'. In: *Science* 340.6129, pp. 167–170.

Chen, Huan-Cheng, Zhe-Feng Lou, Yu-Xing Zhou, Qin Chen, Bin-Jie Xu, Shui-Jin Chen, Jian-Hua Du, Jin-Hu Yang, Hang-Dong Wang and Ming-Hu Fang (2020). 'Negative Magnetoresistance in Antiferromagnetic Topological Insulator $EuSn_2As_2$*'. In: *Chinese Physics Letters* 37.4, p. 047201.

Chen, Lebing, Matthew B Stone, Alexander I Kolesnikov, Barry Winn, Wonhyuk Shon, Pengcheng Dai and Jae-Ho Chung (2021). 'Massless Dirac magnons in the two dimensional van der Waals honeycomb magnet $CrCl_3$'. In: *2D Materials* 9.1, p. 015006.

Chen, Y. J., L. X. Xu, J. H. Li, Y. W. Li, H. Y. Wang, C. F. Zhang, H. Li, Y. Wu, A. J. Liang, C. Chen, S. W. Jung, C. Cacho, Y. H. Mao, S. Liu, M. X. Wang, Y. F. Guo, Y. Xu, Z. K. Liu, L. X. Yang and Y. L. Chen (2019a). 'Topological Electronic Structure and Its Temperature Evolution in Antiferromagnetic Topological Insulator $MnBi_2Te_4$'. In: *Phys. Rev. X* 9 (4), p. 041040.

— (2019b). 'Topological Electronic Structure and Its Temperature Evolution in Antiferromagnetic Topological Insulator $MnBi_2Te_4$'. In: *Phys. Rev. X* 9 (4), p. 041040.

Chubb, S. R. and W. E. Pickett (1987). 'First-principles determination of giant adsorption-induced surface relaxation in p(11) O/Fe(001)'. In: *Phys. Rev. Lett.* 58 (12), pp. 1248–1251.

Cinchetti, M., M. Sánchez Albaneda, D. Hoffmann, T. Roth, J.-P. Wüstenberg, M. Krauß, O. Andreyev, H. C. Schneider, M. Bauer and M. Aeschlimann (2006). 'Spin-Flip Processes and Ultrafast Magnetization Dynamics in Co: Unifying the Microscopic and Macroscopic View of Femtosecond Magnetism'. In: *Phys. Rev. Lett.* 97 (17), p. 177201.

Clarke, A., N. B. Brookes, P. D. Johnson, M. Weinert, B. Sinkovi ć and N. V. Smith (1990). 'Spin-polarized photoemission studies of the adsorption of O and S on Fe(001)'. In: *Phys. Rev. B* 41 (14), pp. 9659–9667.

Colón Santana, Juan A (2015). *Quantitative Core Level Photoelectron Spectroscopy: Brief theory of photoemission spectroscopy*. Morgan & Claypool Publishers, pp. 1–33. ISBN: 978-1-6270-5306-8.

Cucini, Riccardo, Tommaso Pincelli, Giancarlo Panaccione, Damir Kopic, Fabio Frassetto, Paolo Miotti, Gian Marco Pierantozzi, Simone Peli, Andrea Fondacaro, Aleksander De Luisa, Alessandro De Vita, Pietro Carrara, Damjan Krizmancic, Daniel T. Payne, Federico Salvador, Andrea Sterzi, Luca Poletto, Fulvio Parmigiani, Giorgio Rossi and

Federico Cilento (2020). 'Coherent narrowband light source for ultrafast photoelectron spectroscopy in the 17–31 eV photon energy range'. In: *Structural Dynamics* 7.1, p. 014303.

Dalla Longa, F., J. T. Kohlhepp, W. J. M. de Jonge and B. Koopmans (2007). 'Influence of photon angular momentum on ultrafast demagnetization in nickel'. In: *Phys. Rev. B* 75 (22), p. 224431.

Damascelli, Andrea, Zahid Hussain and Zhi-Xun Shen (2003). 'Angle-resolved photoemission studies of the cuprate superconductors'. In: *Rev. Mod. Phys.* 75 (2), pp. 473–541.

De Groot, Frank and Akio Kotani (2008). *Core Level Spectroscopy of Solids*. CRC Press. ISBN: 978-0-849-3-9071-5.

De Vita, A., T.T.P. Nguyen, R. Sant, G.M. Pierantozzi, D. Amoroso, C. Bigi, V. Polewczyk, G. Vinai, L.T. Nguyen, T. Kong, J. Fujii, I. Vobornik, N.B. Brookes, G. Rossi, R.J. Cava, F. Mazzola, K. Yamauchi, S. Picozzi and G. Panaccione (2022). 'Influence of Orbital Character on the Ground State Electronic Properties in the van Der Waals Transition Metal Iodides VI_3 and CrI_3'. In: *Nano Letters* X (X), pp. XXXX–XXXX.

Del Fatti, N., C. Voisin, M. Achermann, S. Tzortzakis, D. Christofilos and F. Vallée (2000). 'Nonequilibrium electron dynamics in noble metals'. In: *Phys. Rev. B* 61 (24), pp. 16956–16966.

Dillon, J. F. and C. E. Olson (1965). 'Magnetization, Resonance, and Optical Properties of the Ferromagnet CrI3'. In: *Journal of Applied Physics* 36.3, pp. 1259–1260.

— (1965). 'Magnetization, Resonance, and Optical Properties of the Ferromagnet CrI3'. In: *Journal of Applied Physics* 36.3, pp. 1259–1260.

Disa, A.S., M. Fechner, T.F. Nova, B. Liu, M. Först, D. Prabhakaran, P.G. Radaelli and A. Cavalleri (2020). 'Polarizing an antiferromagnet by optical engineering of the crystal field'. In: *Nature Phys.* 16, pp. 937–941.

Disa, Ankit S., Tobia F. Nova and Andrea Cavalleri (2021). 'Engineering crystal structures with light'. In: *Nature Physics* 17, pp. 1087–1092.

Eich, Steffen, Moritz Plötzing, Markus Rollinger, Sebastian Emmerich, Roman Adam, Cong Chen, Henry Cornelius Kapteyn, Margaret M. Murnane, Lukasz Plucinski, Daniel Steil, Benjamin Stadtmüller, Mirko Cinchetti, Martin Aeschlimann, Claus M. Schneider and Stefan Mathias (2017). 'Band structure evolution during the ultrafast ferromagnetic-paramagnetic phase transition in cobalt'. In: *Science Advances* 3.3, e1602094.

Einstein, A. (1905). 'Über einen die Erzeugung und Verwandlung des Lichtes betreffenden heuristischen Gesichtspunkt'. In: *Annalen der Physik* 322.6, pp. 132–148.

Engelhardt, J. B., H. Dabringhaus and K. Wandelt (2000). 'Atomic force microscopy study of the CaF2(111) surface : from cleavage via island to evaporation topographies'. In: *Surface Science* 448, pp. 187–200.

— (2000). 'Atomic force microscopy study of the CaF2(111) surface: from cleavage via island to evaporation topographies'. In: *Surface Science* 448.2, pp. 187–200. ISSN: 0039-6028.

Essin, Andrew M., Joel E. Moore and David Vanderbilt (2009). 'Magnetoelectric Polarizability and Axion Electrodynamics in Crystalline Insulators'. In: *Phys. Rev. Lett.* 102 (14), p. 146805.

Fann, W. S., R. Storz, H. W. K. Tom and J. Bokor (1992). 'Direct measurement of nonequilibrium electron-energy distributions in subpicosecond laser-heated gold films'. In: *Phys. Rev. Lett.* 68 (18), pp. 2834–2837.

Farnsworth, H. E. (1926). 'Secondary Electrons from Iron'. In: *Phys. Rev.* 27 (4), pp. 413–422.

Fechner, M., A. Sukhov, L. Chotorlishvili, C. Kenel, J. Berakdar and N. A. Spaldin (2018). 'Magnetophononics: Ultrafast spin control through the lattice'. In: *Phys. Rev. Materials* 2 (6), p. 064401.

Ferrini, Gabriele, Francesco Banfi, Claudio Giannetti and Fulvio Parmigiani (2009). 'Nonlinear electron photoemission from metals with ultrashort pulses'. In: *Nuclear Instruments and Methods in Physics Research Section A: Accelerators, Spectrometers, Detectors and Associated Equipment* 601.1, pp. 123–131. ISSN: 0168-9002.

Finardi, Alice Margherita (2020). 'All-resolved photoemission spectroscopy of Fe(100) and passivated Fe-p(1x1)O surfaces'. BSc Thesis. Università degli Studi di Milano.

Fink, R. L., G. A. Mulhollan, A. B. Andrews, J. L. Erskine and G. K. Walters (1992). 'Spin- and angle-resolved photoemission study of chemisorbed p(1×1) O on epitaxial ultrathin Fe/W(001) films'. In: *Phys. Rev. B* 45 (17), pp. 9824–9833.

Fognini, A., T. U. Michlmayr, G. Salvatella, C. Wetli, U. Ramsperger, T. Bähler, F. Sorgenfrei, M. Beye, A. Eschenlohr, N. Pontius, C. Stamm, F. Hieke, M. Dell'Angela, S. de Jong, R. Kukreja, N. Gerasimova, V. Rybnikov, A. Al-Shemmary, H. Redlin, J. Raabe, A. Föhlisch, H. A. Dürr, W. Wurth, D. Pescia, A. Vaterlaus and Y. Acremann (2014). 'Ultrafast reduction of the total magnetization in iron'. In: *Applied Physics Letters* 104.3, p. 032402.

Frazer, Bradley H, Benjamin Gilbert, Brandon R Sonderegger and Gelsomina De Stasio (2003). 'The probing depth of total electron yield in the sub-keV range: TEY-XAS and X-PEEM'. In: *Surface Science* 537.1, pp. 161–167.

Fu, Liang (2009). 'Hexagonal Warping Effects in the Surface States of the Topological Insulator Bi_2Te_3'. In: *Phys. Rev. Lett.* 103 (26), p. 266801.

— (2011). 'Topological Crystalline Insulators'. In: *Phys. Rev. Lett.* 106 (10), p. 106802.

Fu, Liang and C. L. Kane (2006). 'Time reversal polarization and a Z_2 adiabatic spin pump'. In: *Phys. Rev. B* 74 (19), p. 195312.

Fujii, Jun et al. (in preparation). '–'. In: –.

Gati, Elena, Yuji Inagaki, Tai Kong, Robert J. Cava, Yuji Furukawa, Paul C. Canfield and Sergey L. Bud'ko (2019). 'Multiple ferromagnetic transitions and structural distortion in the van der Waals ferromagnet VI_3 at ambient and finite pressures'. In: *Phys. Rev. B* 100 (9), p. 094408.

Gay, T. J. and F. B. Dunning (1992). 'Mott electron polarimetry'. In: *Review of Scientific Instruments* 63.2, pp. 1635–1651.

Geim, A. K. and K. S. Novoselov (2007). 'The rise of graphene'. In: *Nature Mater.* 6, pp. 183–191.

Gerth, Ch., K. Godehusen, M. Richter, P. Zimmermann, J. Schulz, Ph. Wernet, B. Sonntag, A. G. Kochur and I. D. Petrov (2000). 'Multiplet and lifetime effects in the 4d photoelectron spectrum of Eu'. In: *Phys. Rev. A* 61 (2), p. 022713.

Gibertini, M., M. Koperski, A.F. Morpurgo and K.S. Novoselov (2019). 'Magnetic 2D materials and heterostructures'. In: *Nat. Nanotechnol.* 14, pp. 408–419.

Giuliani, Gabriele and Giovanni Vignale (2005a). *Quantum Theory of the Electron Liquid*. Cambridge University Press.

— (2005b). *Quantum Theory of the Electron Liquid*. Cambridge University Press. ISBN: 978-0-511-61991-5.

Groeneveld, Rogier H. M., Rudolf Sprik and Ad Lagendijk (1992). 'Effect of a nonthermal electron distribution on the electron-phonon energy relaxation process in noble metals'. In: *Phys. Rev. B* 45 (9), pp. 5079–5082.

Groot, F. M. F. de, J. C. Fuggle, B. T. Thole and G. A. Sawatzky (1990). '2p x-ray absorption of 3d transition-metal compounds: An atomic multiplet description including the crystal field'. In: *Phys. Rev. B* 42 (9), pp. 5459–5468.

Güdde, J., U. Conrad, V. Jähnke, J. Hohlfeld and E. Matthias (1999). 'Magnetization dynamics of Ni and Co films on Cu(001) and of bulk nickel surfaces'. In: *Phys. Rev. B* 59 (10), R6608–R6611.

Gui, Xin, Ivo Pletikosic, Huibo Cao, Hung-Ju Tien, Xitong Xu, Ruidan Zhong, Guangqiang Wang, Tay-Rong Chang, Shuang Jia, Tonica Valla, Weiwei Xie and Robert J. Cava (2019). 'A New Magnetic Topological Quantum Material Candidate by Design'. In: *ACS Central Science* 5.5, pp. 900–910.

Guo, Zongxia, Jialiang Yin, Yue Bai, Daoqian Zhu, Kewen Shi, Gefei Wang, Kaihua Cao and Weisheng Zhao (2021). 'Spintronics for Energy- Efficient Computing: An Overview and Outlook'. In: *Proceedings of the IEEE* 109.8, pp. 1398–1417.

Harris, L B and J Fiasson (1985). 'Direct determination of surface potential on sodium chloride single crystals. I. Analysis of measurements'. In: *Journal of Physics C: Solid State Physics* 18.25, pp. 4845–4862.

Hasan, M. Z. and C. L. Kane (2010). 'Colloquium: Topological insulators'. In: *Rev. Mod. Phys.* 82 (4), pp. 3045–3067.

He, Junjie, Shuangying Ma, Pengbo Lyu and Petr Nachtigall (2016). 'Unusual Dirac half-metallicity with intrinsic ferromagnetism in vanadium trihalide monolayers'. In: *J. Mater. Chem. C* 4 (13), pp. 2518–2526.

Hertz, H. (1887). 'Ueber einen Einfluss des ultravioletten Lichtes auf die electrische Entladung'. In: *Annalen der Physik* 267.8, pp. 983–1000.

Hippert, F., E. Geissler, J.L. Hodeau, E. Lelièvre-Berna and J.R. Regnard (2006). *Neutron and X-ray Spectroscopy*. Springer Dordrecht. ISBN: 978-1-4020-3336-0.

Ho, J.T. and J.D. Litster (1969). 'Divergences of the Magnetic Properties of CrBr3 near the Critical Point'. In: *Journal of Applied Physics* 40.3, pp. 1270–1271.

Hofmann, J.A., A. Paskin, K.J. Tauer and R.J. Weiss (1956). 'Analysis of ferromagnetic and antiferro-magnetic second-order transitions'. In: *Journal of Physics and Chemistry of Solids* 1.1, pp. 45–60. ISSN: 0022-3697.

Hopkinson, J.F.L., J.B. Pendry and D.J. Titterington (1980). 'Calculation of photoemission spectra for surfaces of solids'. In: *Computer Physics Communications* 19.1, pp. 69–92. ISSN: 0010-4655.

Hopster, H., R. Raue, E. Kisker, G. Güntherodt and M. Campagna (1983). 'Evidence for Spin-Dependent Electron-Hole-Pair Excitations in Spin-Polarized Secondary-Electron Emission from Ni(110)'. In: *Phys. Rev. Lett.* 50 (1), pp. 70–73.

Hou, Yusheng and Ruqian Wu (2019). 'Axion Insulator State in a Ferromagnet/Topological Insulator/Antiferromagnet Heterostructure'. In: *Nano Letters* 19 (4), pp. 2472–2477.

Huang, B., G. Clark, E. Navarro-Moratalla, D.R. Klein, R. Cheng, K.L. Seyler, D. Zhong, E. Schmidgall, M.A. McGuire, D.H. Cobden, W. Yao, D. Xiao, P. Jarillo-Herrero and X. Xu (2017). 'Layer-dependent ferromagnetism in a van der Waals crystal down to the monolayer limit'. In: *Nature* 546, pp. 270–273.

Huang, Chengxi, Fang Wu, Shunli Yu, Puru Jena and Erjun Kan (2020). 'Discovery of twin orbital-order phases in ferromagnetic semiconducting VI3 monolayer'. In: *Phys. Chem. Chem. Phys.* 22 (2), pp. 512–517.

Huang, Hong and J. Hermanson (1985). 'Bonding and magnetism of chemisorbed oxygen on Fe(001)'. In: *Phys. Rev. B* 32 (10), pp. 6312–6318.

Jensen, J. and A.R. Mackintosh (1991). *Rare Earth Magnetism: Structure and Excitations*. Oxford University Press. ISBN: 9780198520276.

Jozwiak, C., Y L. Chen, A V. Fedorov, J G. Analytis, C R. Rotundu, A K. Schmid, J D. Denlinger, Y.-D. Chuang, D.-H. Lee, I R. Fisher, R J. Birgeneau, Z.-X. Shen, Z. Hussain and A. Lanzara (2011). 'Widespread spin polarization effects in photoemission from topological insulators'. In: *Phys. Rev. B* 84 (16), p. 165113.

Jozwiak, C., J.A. Sobota, K. Gotlieb, A.F. Kemper, C.R. Rotundu, R.J. Birgeneau, Z. Hussain, D.H. Lee, Z.X. Shen and A. Lanzara (2016). 'Spin-polarized surface resonances accompanying topological surface state formation'. In: *Nature Communications* 14.7, p. 13143.

Kane, C. L. and E. J. Mele (2005). 'Z_2 Topological Order and the Quantum Spin Hall Effect'. In: *Phys. Rev. Lett.* 95 (14), p. 146802.

Kaufman, Larry, E.V Clougherty and R.J Weiss (1963). 'The lattice stability of metals—III. Iron'. In: *Acta Metallurgica* 11.5, pp. 323–335. ISSN: 0001-6160.

Kawamoto, Takahiro, Koji Fujita, Hirofumi Akamatsu, Tetsuya Nakamura, Toyohiko Kinoshita, Masaichiro Mizumaki, Naomi Kawamura, Motohiro Suzuki, Yoshiro Kususe, Shunsuke Murai and Katsuhisa Tanaka (2013). 'Ferromagnetic amorphous oxides in the EuO-TiO_2 system studied by the Faraday effect in the visible region and the x-ray magnetic circular dichroism at the Eu $M_{4,5}$ and $L_{2,3}$ edges'. In: *Phys. Rev. B* 88 (2), p. 024405.

Kim, Dong-Hwan, Kyoo Kim, Kyung-Tae Ko, JunHo Seo, Jun Sung Kim, Tae-Hwan Jang, Younghak Kim, Jae-Young Kim, Sang-Wook Cheong and Jae-Hoon Park (2019). 'Giant Magnetic Anisotropy Induced by Ligand LS Coupling in Layered Cr Compounds'. In: *Phys. Rev. Lett.* 122 (20), p. 207201.

Kim, M., P. Kumaravadivel, J. Birkbeck, W. Kuang, S. G. Xu, D. G. Hopkinson, J. Knolle, P. A. McClarty, A. I. Berdyugin, M. Ben Shalom, R. V. Gorbachev, S. J. Haigh, S. Liu, J. H. Edgar, K. S. Novoselov, I. V. Grigorieva and A. K. Geim (2019). 'Micromagnetometry of two-dimensional ferromagnets'. In: *Nature Electron.* 2, pp. 457–463.

King, P.D.C., S. Picozzi, R.G. Egdell and G. Panaccione (2021). 'Angle, Spin, and Depth Resolved Photoelectron Spectroscopy on Quantum Materials'. In: *Chem. Rev.* 121 (5), pp. 2816–2856.

Kirilyuk, Andrei, Alexey V. Kimel and Theo Rasing (2010). 'Ultrafast optical manipulation of magnetic order'. In: *Rev. Mod. Phys.* 82 (3), pp. 2731–2784.

Kisker, E., W. Gudat and K. Schröder (1982). 'Observation of a high spin polarization of secondary electrons from single crystal Fe and Co'. In: *Solid State Communications* 44.5, pp. 591–595. ISSN: 0038-1098.

Kong, Tai, Karoline Stolze, Erik I. Timmons, Jing Tao, Danrui Ni, Shu Guo, Zoë Yang, Ruslan Prozorov and Robert J. Cava (2019). 'VI_3 – a New Layered Ferromagnetic Semiconductor'. In: *Advanced Materials* 31.17, p. 1808074.

Koopmans, B., M. van Kampen, J. T. Kohlhepp and W. J. M. de Jonge (2000). 'Ultrafast Magneto-Optics in Nickel: Magnetism or Optics?' In: *Phys. Rev. Lett.* 85 (4), pp. 844–847.

Koopmans, B., G. Malinowski, F. Dalla Longa, D. Steiauf, M. Fähnle, T. Roth, M. Cinchetti and M. Aeschlimann (2010). 'Explaining the paradoxical diversity of ultrafast laser-induced demagnetization'. In: *Nature Mater.* 9, pp. 259–265.

Kratochvílová, M., K. Uhlířová, M. Míšek, V. Holý, J. Zázvorka, M. Veis, J. Pospíšil, S. Son, J.-G. Park and V. Sechovský (2022). 'The surface degradation and its impact on the magnetic properties of bulk VI_3'. In: *Materials Chemistry and Physics* 278, p. 125590.

Krüger, M., M. Schenk, M. Förster and P. Hommelhoff (2012). 'Attosecond physics in photoemission from a metal nanotip'. In: *Journal of Physics B: Atomic, Molecular and Optical Physics* 45.7, p. 074006.

Kummer, K., A. Fondacaro, E. Jimenez, E. Velez-Fort, A. Amorese, M. Aspbury, F. Yakhou-Harris, van der Linden P and Brookes NB (2016). 'The high-field magnet endstation for X-ray magnetic dichroism experiments at ESRF soft X-ray beamline ID32'. In: *Journal of Synchrotron Radiation* 23.2, pp. 464–473.

Kundu, A.K., Y. Liu, C. Petrovic and T. Valla (2020). 'Valence band electronic structure of the van der Waals ferromagnetic insulators: VI_3 and CrI_3'. In: *Sci. Rep.* 10, p. 15602.

Landolt, M. and D. Mauri (1982). 'Spin-Polarized Auger Spectroscopy from Magnetically Ordered Solids'. In: *Phys. Rev. Lett.* 49 (24), pp. 1783–1786.

Lawler, J. F., R. Schad, S. Jordan and H. van Kempen (1997). 'Structure of epitaxial Fe films on MgO(100)'. In: *Journal of Magnetism and Magnetic Materials* 165.1-3, pp. 224–226.

Lee, K., J. H. Bak, Y. J. Kim, C. K. Kim, A. Antonyan, D. H. Chang, S. H. Hwang, G. W. Lee, N. Y. Ji, W. J. Kim, J. H. Lee, B. J. Bae, J. H. Park, I. H. Kim, B. Y. Seo, S. H. Han, Y. Ji, H. T. Jung, S. O. Park, O. I. Kwon, J. W. Kye, Y. D. Kim, S. W. Pae, Y. J. Song, G. T. Jeong, K. H. Hwang, G. H. Koh, H. K. Kang and E. S. Jung (2019). '1Gbit High Density Embedded STT-MRAM in 28nm FDSOI Technology'. In: *2019 IEEE International Electron Devices Meeting (IEDM)*, pp. 2.2.1–2.2.4.

Lee, Tien-Lin and David A. Duncan (2018). 'A Two-Color Beamline for Electron Spectroscopies at Diamond Light Source'. In: *Synchrotron Radiation News* 31.4, pp. 16–22.

Li, Hang, Shun-Ye Gao, Shao-Feng Duan, Yuan-Feng Xu, Ke-Jia Zhu, Shang-Jie Tian, Jia-Cheng Gao, Wen-Hui Fan, Zhi-Cheng Rao, Jie-Rui Huang, Jia-Jun Li, Da-Yu Yan, Zheng-Tai Liu, Wan-Ling Liu, Yao-Bo Huang, Yu-Liang Li, Yi Liu, Guo-Bin Zhang, Peng Zhang, Takeshi Kondo, Shik Shin, He-Chang Lei, You-Guo Shi, Wen-Tao Zhang, Hong-Ming Weng, Tian Qian and Hong Ding (2019). 'Dirac Surface States in Intrinsic Magnetic Topological Insulators $EuSn_2As_2$ and $MnBi_{2n}Te_{3n+1}$'. In: *Phys. Rev. X* 9 (4), p. 041039.

Li, Jiaheng, Yang Li, Shiqiao Du, Zun Wang, Bing-Lin Gu, Shou-Cheng Zhang, Ke He, Wenhui Duan and Yong Xu (2019). 'Intrinsic magnetic topological insulators in van der Waals layered MnBi¡sub¿2¡/sub¿Te¡sub¿4¡/sub¿-family materials'. In: *Science Advances* 5.6, eaaw5685.

Liqin, K. and M.I. Katsnelson (2021). 'Electron correlation effects on exchange interactions and spin excitations in 2D van der Waals materials'. In: *npj Comput. Mater.* 7 (4).

Liu, Chang, Yongchao Wang, Hao Li, Yang Wu, Yaoxin Li, Jiaheng Li, Ke He, Yong Xu, Jinsong Zhang and Yayu Wang (2020). 'Robust axion insulator and Chern insulator phases in a two-dimensional antiferromagnetic topological insulator'. In: *Nature Materials* 19, pp. 522–527.

Liu, Yu, Milinda Abeykoon and C. Petrovic (2020). 'Critical behavior and magnetocaloric effect in VI_3'. In: *Phys. Rev. Research* 2 (1), p. 013013.

Maganas, Dimitrios, Joanna K. Kowalska, Casey Van Stappen, Serena DeBeer and Frank Neese (2020). 'Mechanism of $L_{2,3}$-edge x-ray magnetic circular dichroism intensity from quantum chemical calculations and experiment – A case study on V(IV)/V(III) complexes'. In: *The Journal of Chemical Physics* 152.11, p. 114107.

Magnusson, K. O. and B. Reihl (1989). 'Surface electronic structure of submonolayer to full-monolayer coverages of alkali metals on GaAs(110): K and Cs'. In: *Phys. Rev. B* 40 (11), pp. 7814–7818.

Mak, Kin Fai, Changgu Lee, James Hone, Jie Shan and Tony F. Heinz (2010). 'Atomically Thin MoS_2: A New Direct-Gap Semiconductor'. In: *Phys. Rev. Lett.* 105 (13), p. 136805.

Manipatruni, S., D.E.. Nikonov, C.C. Lin, T.A. Gosavi, H. Liu, B. Prasad, Y.L. Huang, E. Bonturim, R. Ramesh and I.A. Young (2019). 'Scalable energy-efficient magnetoelectric spin-orbit logic'. In: *Nature* 565, pp. 35–42.

Marx, G. K. L., P.-O. Jubert, A. Bischof and R. Allenspach (2003). 'Probing depth of threshold photoemission electron microscopy'. In: *Applied Physics Letters* 83.14, pp. 2925–2927.

Mathias, Stefan, Chan La-o-vorakiat, Justin M. Shaw, Emrah Turgut, Patrik Grychtol, Roman Adam, Dennis Rudolf, Hans T. Nembach, Thomas J. Silva, Martin Aeschlimann, Claus M. Schneider, Henry C. Kapteyn and Margaret M. Murnane (2013). 'Ultrafast element-specific magnetization dynamics of complex magnetic materials on a tabletop'. In: *Journal of Electron Spectroscopy and Related Phenomena* 189, pp. 164–170. ISSN: 0368-2048.

Mazin, I. I. (1999). 'How to Define and Calculate the Degree of Spin Polarization in Ferromagnets'. In: *Phys. Rev. Lett.* 83 (7), pp. 1427–1430.

McGuire, Michael A., Genevieve Clark, Santosh KC, W. Michael Chance, Gerald E. Jellison, Valentino R. Cooper, Xiaodong Xu and Brian C. Sales (2017). 'Magnetic behavior and spin-lattice coupling in cleavable van der Waals layered $CrCl_3$ crystals'. In: *Phys. Rev. Materials* 1 (1), p. 014001.

McGuire, Michael A., Hemant Dixit, Valentino R. Cooper and Brian C. Sales (2015). 'Coupling of Crystal Structure and Magnetism in the Layered, Ferromagnetic Insulator CrI_3'. In: *Chemistry of Materials* 27.2, pp. 612–620.

Minár, J., J. Braun, S. Mankovsky and H. Ebert (2011). 'Calculation of angle-resolved photo emission spectra within the one-step model of photo emission—Recent developments'. In: *Journal of Electron Spectroscopy and Related Phenomena* 184.3, pp. 91–99. ISSN: 0368-2048.

Mobilio, S., F. Boscherini and C. Meneghini (2015). *Synchrotron Radiation*. Springer Berlin. ISBN: 978-3-642-55315-8.

Mong, Roger S. K., Andrew M. Essin and Joel E. Moore (2010a). 'Antiferromagnetic topological insulators'. In: *Phys. Rev. B* 81 (24), p. 245209.

— (2010b). 'Antiferromagnetic topological insulators'. In: *Phys. Rev. B* 81 (24), p. 245209.

Moulder, J.F., W.F. Stickle, P.E. Sobol and K.D. Bomben (1992). *Rare Earth Magnetism: Structure and Excitations*. Ed. by Jill Chastain. Perkin-Elmer Corporation, Physical Electronics Division. ISBN: 9780962702624.

Mounet, N., M. Gibertini, P. Schwaller, D. Campi, A. Merkys, A. Marrazzo, T. Sohier, I.E. Castelli, A. Cepellotti, G. Pizzi and N. Marzari (2018). 'Two-dimensional materials from high-throughput computational exfoliation of experimentally known compounds'. In: *Nat. Nanotechnol.* 13, pp. 246–252.

Mueller, B Y, T Roth, M Cinchetti, M Aeschlimann and B Rethfeld (2011). 'Driving force of ultrafast magnetization dynamics'. In: *New Journal of Physics* 13.12, p. 123010.

Negusse, Ezana, J. Dvorak, J. S. Holroyd, M. Liberati, T. S. Santos, J. S. Moodera, E. Arenholz and Y. U. Idzerda (2009). 'Magnetic characterization of ultrathin EuO films with XMCD'. In: *Journal of Applied Physics* 105.7, p. 07C930.

Nguyen, Thi Phuong Thao, Kunihiko Yamauchi, Tamio Oguchi, Danila Amoroso and Silvia Picozzi (2021). 'Electric-field tuning of the magnetic properties of bilayer VI_3: A first-principles study'. In: *Phys. Rev. B* 104 (1), p. 014414.

Novoselov, K. S., A. K. Geim, S. V. Morozov, D. Jiang, Y. Zhang, S. V. Dubonos, I. V. Grigorieva and A. A. Firsov (2004). 'Electric Field Effect in Atomically Thin Carbon Films'. In: *Science* 306.5696, pp. 666–669.

Novoselov, K. S., D. Jiang, F. Schedin, T. J. Booth, V. V. Khotkevich, S. V. Morozov and A. K. Geim (2005). 'Two-dimensional atomic crystals'. In: *Proceedings of the National Academy of Sciences* 102.30, pp. 10451–10453.

La-O-Vorakiat, Chan, Mark Siemens, Margaret M. Murnane, Henry C. Kapteyn, Stefan Mathias, Martin Aeschlimann, Patrik Grychtol, Roman Adam, Claus M. Schneider, Justin M. Shaw, Hans Nembach and T. J. Silva (2009). 'Ultrafast Demagnetization Dynamics at the M Edges of Magnetic Elements Observed Using a Tabletop High-Harmonic Soft X-Ray Source'. In: *Phys. Rev. Lett.* 103 (25), p. 257402.

Al-Obaidi, R, M Wilke, M Borgwardt, J Metje, A Moguilevski, N Engel, D Tolksdorf, A Raheem, T Kampen, S Mähl, I Yu Kiyan and E F Aziz (2015). 'Ultrafast photoelectron spectroscopy of solutions: space-charge effect'. In: *New Journal of Physics* 17.9, p. 093016.

Offi, F., L. Avaldi, R. Camilloni, G. Dawber, G.C. King and G. Stefani (2007). 'Threshold photoemission spectroscopy in solids'. In: *Journal of Electron Spectroscopy and Related Phenomena* 154.3, pp. 63–68. ISSN: 0368-2048.

Oloff, L.P., K. Hanff, A. Stange, G. Rohde, F. Diekmann, M. Bauer and K. Rossnagel (2016). 'Pump laser-induced space-charge effects in HHG-driven time- and angle-resolved photoelectron spectroscopy'. In: *Journal of Applied Physics* 119.22, p. 225106.

Oloff, Lars-Philip, Ashish Chainani, Masaharu Matsunami, Kazutoshi Takahashi, Tadashi Togashi, Hitoshi Osawa, Kerstin Hanff, Arndt Quer, Ryuki Matsushita, Ryutaro Shiraishi, Maki Nagashima, Ayato Kimura, Kotaro Matsuishi, Makina Yabashi, Yoshihito Tanaka, Giorgio Rossi, Tetsuya Ishikawa, Kai Rossnagel and Masaki Oura (2016). 'Time-resolved HAXPES using a microfocused XFEL beam: From vacuum space-charge effects to intrinsic charge-carrier recombination dynamics'. In: *Scientific reports* 6.35087. ISSN: 2045-2322.

Otrokov, M. M., I. I. Klimovskikh, H. Bentmann, D. Estyunin, A. Zeugner, Z. S. Aliev, S. Gaß, A. U. B. Wolter, A. V. Koroleva, A. M. Shikin, M. Blanco-Rey, M. Hoffmann, I. P. Rusinov, A. Yu. Vyazovskaya, S. V. Eremeev, Yu. M. Koroteev, V. M. Kuznetsov, F. Freyse, J. Sánchez-Barriga, I. R. Amiraslanov, M. B. Babanly, N. T. Mamedov, N. A. Abdullayev, V. N. Zverev, A. Alfonsov, V. Kataev, B. Büchner, E. F. Schwier, S. Kumar, A. Kimura, L. Petaccia, G. Di Santo, R. C. Vidal, S. Schatz, K. Kißner, M. Ünzelmann, C. H. Min, S. Moser, T. R. F. Peixoto, F. Reinert, A. Ernst, P. M. Echenique, A. Isaeva and E. V. Chulkov (2019). 'Prediction and observation of an antiferromagnetic topological insulator'. In: *Nature* 576, pp. 416–422.

Panaccione, Giancarlo, Ivana Vobornik, Jun Fujii, Damjan Krizmancic, Emilia Annese, L Giovanelli, Francesco Maccherozzi, Federico Salvador, Aleksander De Luisa, Davide Benedetti, Ana Gruden, Paolo Bertoch, Francois A. Polack, Daniele Cocco, Giovanni Sostero, Bruno Diviacco, Michael Hochstrasser, Urs Maier, Danilo Pescia, Christian H. Back, Thomas Greber, Jürg Osterwalder, M. S. Galaktionov, Massimo Sancrotti and Giorgio Rossi (2009). 'Advanced photoelectric effect experiment beamline at Elettra: A surface science laboratory coupled with Synchrotron Radiation.' In: *The Review of scientific instruments* 80 4, p. 043105.

Panzner, G., D. R. Mueller and T. N. Rhodin (1985). 'Angle-resolved photoemission studies of oxygen adsorbed on Fe(100)'. In: *Phys. Rev. B* 32 (6), pp. 3472–3478.

Pasmans, P. L. E. M., D. C. van Vugt, J. P. van Lieshout, G. J. H. Brussaard and O. J. Luiten (2016). 'Extreme regimes of femtosecond photoemission from a copper cathode in a dc electron gun'. In: *Phys. Rev. Accel. Beams* 19 (10), p. 103403.

Paul, O., S. Toscano, K. Totland and M. Landolt (1991). 'The spatial origin of the spin-polarization of secondary-electron emission from Fe'. In: *Surface Science* 251-252, pp. 27–30. ISSN: 0039-6028.

Pelli Cresi, Jacopo Stefano, Eleonora Spurio, Lorenzo Di Mario, Patrick O'Keeffe, Stefano Turchini, Stefania Benedetti, Gian Marco Pierantozzi, Alessandro De Vita, Riccardo Cucini, Daniele Catone and Paola Luches (2022). 'Lifetime of Photogenerated Positive Charges in Hybrid Cerium Oxide-Based Materials from Space and Mirror Charge Effects in Time-Resolved Photoemission Spectroscopy'. In: *J. Phys. Chem. C* 126.27, pp. 11174–11181.

Pendry, J.B. (1976). 'Theory of photoemission'. In: *Surface Science* 57.2, pp. 679–705. ISSN: 0039-6028.

Penn, David R., S. Peter Apell and S. M. Girvin (1985). 'Theory of spin-polarized secondary electrons in transition metals'. In: *Phys. Rev. Lett.* 55 (5), pp. 518–521.

Pierantozzi, Gian Marco, Alessandro De Vita, Chiara Bigi, Xin Gui, Hung-Ju Tien, Debashis Mondal, Federico Mazzola, Jun Fujii, Ivana Vobornik, Giovanni Vinai, Alessandro Sala, Cristina Africh, Tien-Lin Lee, Giorgio Rossi, Tay-Rong Chang, Weiwei Xie, Robert J. Cava and Giancarlo Panaccione (2022). 'Evidence of magnetism-induced topological protection in the axion insulator candidate $EuSn_2P_2$'. In: *Proceedings of the National Academy of Sciences* 119.4, e2116575119.

Pincelli, T., F. Grasselli, V.N. Petrov, P. Torelli and G. Rossi (2017). 'Performance of photoelectron spin polarimeters with continuous and pulsed sources: from storage rings to free electron lasers,' in: *Journal of Synchrotron Radiation* 24 (175).

Pincelli, T., V. N. Petrov, G. Brajnik, R. Ciprian, V. Lollobrigida, P. Torelli, D. Krizmancic, F. Salvador, A. De Luisa, R. Sergo, A. Gubertini, G. Cautero, S. Carrato, G. Rossi and G. Panaccione (2016). 'Design and optimization of a modular setup for measurements of three-dimensional spin polarization with ultrafast pulsed sources'. In: *Review of Scientific Instruments* 87.3, p. 035111.

Popmintchev, Tenio, Ming-Chang Chen, Paul Arpin, Margaret M. Murnane and Henry C. Kapteyn (2010). 'The attosecond nonlinear optics of bright coherent X-ray generation'. In: *Nature Photon.* 4, pp. 822–832.

Reinsel, David, John Gantz and John Rydning (2017). *Data Age 2025: The Evolution of Data to Life-Critical*. IDC White Paper sponsored by Seagate. IDC. URL: https://www.import.io/wp-content/uploads/2017/04/Seagate-WP-DataAge2025-March-2017.pdf.

— (2018). *The Digitization of the World: From Edge to Core*. IDC White Paper sponsored by Seagate. IDC. URL: https://www.seagate.com/files/www-content/our-story/trends/files/idc-seagate-dataage-whitepaper.pdf.

Reinsel, David, John Rydning and John Gantz (2021). *Worldwide Global DataSphere Forecast, 2021-2025*. IDC Market Forecast. IDC.

Reutzel, Marcel, Andi Li and Hrvoje Petek (2020). 'Above-threshold multiphoton photoemission from noble metal surfaces'. In: *Phys. Rev. B* 101 (7), p. 075409.

Reyes-Retana, J.A. and F. Cervantes-Sodi (2016). 'Spin-orbital effects in metal-dichalcogenide semiconducting monolayers'. In: *Sci. Rep.* 6, p. 24093.

Rhie, H.-S., H. A. Dürr and W. Eberhardt (2003). 'Femtosecond Electron and Spin Dynamics in Ni/W(110) Films'. In: *Phys. Rev. Lett.* 90 (24), p. 247201.

Ruck, B. J., H. J. Trodahl, J. H. Richter, J. C. Cezar, F. Wilhelm, A. Rogalev, V. N. Antonov, Binh Do Le and C. Meyer (2011). 'Magnetic state of EuN: X-ray magnetic circular dichroism at the Eu $M_{4,5}$ and $L_{2,3}$ absorption edges'. In: *Phys. Rev. B* 83 (17), p. 174404.

Samarth, N. (2017). 'Magnetism in flatland'. In: *Nature* 546, pp. 216–217.

Sánchez-Barriga, J., A. Varykhalov, J. Braun, S.-Y. Xu, N. Alidoust, O. Kornilov, J. Minár, K. Hummer, G. Springholz, G. Bauer, R. Schumann, L. V. Yashina, H. Ebert, M. Z. Hasan and O. Rader (2014). 'Photoemission of Bi_2Se_3 with Circularly Polarized Light: Probe of Spin Polarization or Means for Spin Manipulation?' In: *Phys. Rev. X* 4 (1), p. 011046.

Sato, Takafumi, Zhiwei Wang, Daichi Takane, Seigo Souma, Chaoxi Cui, Yongkai Li, Kosuke Nakayama, Tappei Kawakami, Yuya Kubota, Cephise Cacho, Timur K. Kim, Arian Arab, Vladimir N. Strocov, Yugui Yao and Takashi Takahashi (2020). 'Signature of band inversion in the antiferromagnetic phase of axion insulator candidate $EuIn_2As_2$'. In: *Phys. Rev. Research* 2 (3), p. 033342.

Schellekens, A. J., W. Verhoeven, T. N. Vader and B. Koopmans (2013). 'Investigating the contribution of superdiffusive transport to ultrafast demagnetization of ferromagnetic thin films'. In: *Applied Physics Letters* 102.25, p. 252408.

Schenk, Markus, Michael Krüger and Peter Hommelhoff (2010). 'Strong-Field Above-Threshold Photoemission from Sharp Metal Tips'. In: *Phys. Rev. Lett.* 105 (25), p. 257601.

Schmitz, Detlef, Carolin Schmitz-Antoniak, Florin Radu, Hanjo Ryll, Chen Luo, Sumanta Bhandary, Silke Biermann, Konrad Siemensmeyer, Heiko Wende, Sergey Ivanov and Olle Eriksson (2020). 'Soft X-Ray Magnetic Circular Dichroism of Vanadium in the Metal–Insulator Two-Phase Region of Paramagnetic V2O3 Doped with 1.1 % Chromium'. In: *physica status solidi (b)* 257.3, p. 1900456.

Seah, M. P. and W. A. Dench (1979). 'Quantitative electron spectroscopy of surfaces: A standard data base for electron inelastic mean free paths in solids'. In: *Surface and Interface Analysis* 1.1, pp. 2–11.

Shen, S.Q. (2017). *Topological Insulators*. Springer Singapore. ISBN: 978-981-10-4606-3.

Shu-hua, Li (1954). 'Origine de la Boussole II. Aimant et Boussole'. In: *Isis* 45.2, pp. 175–196.

Sirotti, F., G. Panaccione and G. Rossi (1994). 'Spin filtering effect on secondary electrons crossing an iron overlayer'. In: *Journal de Physique IV Proceedings* 04.C9, pp. C9-175-C9–178.

Sobota, J. A., S.-L. Yang, A. F. Kemper, J. J. Lee, F. T. Schmitt, W. Li, R. G. Moore, J. G. Analytis, I. R. Fisher, P. S. Kirchmann, T. P. Devereaux and Z.-X. Shen (2013). 'Direct Optical Coupling to an Unoccupied Dirac Surface State in the Topological Insulator Bi_2Se_3'. In: *Phys. Rev. Lett.* 111 (13), p. 136802.

Son, Suhan, Matthew J. Coak, Nahyun Lee, Jonghyeon Kim, Tae Yun Kim, Hayrullo Hamidov, Hwanbeom Cho, Cheng Liu, David M. Jarvis, Philip A. C. Brown, Jae Hoon Kim, Cheol-Hwan Park, Daniel I. Khomskii, Siddharth S. Saxena and Je-Geun Park (2019). 'Bulk properties of the van der Waals hard ferromagnet VI_3'. In: *Phys. Rev. B* 99 (4), p. 041402.

Spesyvtsev, R., J.G. Underwood and H.H. Fielding (2014). *Ultrafast Phenomena in Molecular Sciences: Time-Resolved Photoelectron Spectroscopy for Excited State Dynamics*. Springer Cham. ISBN: 978-3-319-02050-1.

Stöhr, J. and H. König (1995). 'Determination of Spin- and Orbital-Moment Anisotropies in Transition Metals by Angle-Dependent X-Ray Magnetic Circular Dichroism'. In: *Phys. Rev. Lett.* 75 (20), pp. 3748–3751.

Stöhr, Joachim and Hans Christoph Siegmann (2006). *Magnetism: From Fundamentals to Nanoscale Dynamics*. Springer Berlin. ISBN: 978-3-540-30282-7.

Stolow, A., A.E. Bragg and D.M. Neumark (2004). 'Femtosecond Time-Resolved Photoelectron Spectroscopy'. In: *Chem. Rev.* 104.4, pp. 1719–1758.

Sun, C.-K., F. Vallée, L. H. Acioli, E. P. Ippen and J. G. Fujimoto (1994). 'Femtosecond-tunable measurement of electron thermalization in gold'. In: *Phys. Rev. B* 50 (20), pp. 15337–15348.

Suzuki, M., B. Gao, K. Koshiishi, S. Nakata, K. Hagiwara, C. Lin, Y. X. Wan, H. Kumigashira, K. Ono, Sungmo Kang, Seungjin Kang, J. Yu, M. Kobayashi, S.-W. Cheong and A. Fujimori (2019). 'Coulomb-interaction effect on the two-dimensional electronic structure of the van der Waals ferromagnet $Cr_2Ge_2Te_6$'. In: *Phys. Rev. B* 99 (16), p. 161401.

Suzuki, Toshinori (2012). 'Time-resolved photoelectron spectroscopy of non-adiabatic electronic dynamics in gas and liquid phases'. In: *International Reviews in Physical Chemistry* 31.2, pp. 265–318.

Taroni, A, S T Bramwell and P C W Holdsworth (2008). 'Universal window for two-dimensional critical exponents'. In: *Journal of Physics: Condensed Matter* 20.27, p. 275233.

Tengdin, Phoebe, Wenjing You, Cong Chen, Xun Shi, Dmitriy Zusin, Yingchao Zhang, Christian Gentry, Adam Blonsky, Mark Keller, Peter M. Oppeneer, Henry C. Kapteyn, Zhensheng Tao and Margaret M. Murnane (2018). 'Critical behavior within 20 fs drives the out-of-equilibrium laser-induced magnetic phase transition in nickel'. In: *Science Advances* 4.3, eaap9744.

Teo, Jeffrey C. Y., Liang Fu and C. L. Kane (2008). 'Surface states and topological invariants in three-dimensional topological insulators: Application to $Bi_{1-x}Sb_x$'. In: *Phys. Rev. B* 78 (4), p. 045426.

Thole, B. T., P. Carra, F. Sette and G. van der Laan (1992). 'X-ray circular dichroism as a probe of orbital magnetization'. In: *Phys. Rev. Lett.* 68 (12), pp. 1943–1946.

Thole, B. T., G. van der Laan, J. C. Fuggle, G. A. Sawatzky, R. C. Karnatak and J.-M. Esteva (1985). '3d x-ray-absorption lines and the $3d^9 4f^{n+1}$ multiplets of the lanthanides'. In: *Phys. Rev. B* 32 (8), pp. 5107–5118.

Tian, Shangjie, Jian-Feng Zhang, Chenghe Li, Tianping Ying, Shiyan Li, Xiao Zhang, Kai Liu and Hechang Lei (2019). 'Ferromagnetic van der Waals Crystal VI_3'. In: *Journal of the American Chemical Society* 141.13, pp. 5326–5333.

Tono, K., T. Togashi, Y. Inubushi, T. Sato, T. Katayama, K. Ogawa, H. Ohashi, H. Kimura, S. Takahashi, K. Takeshita, H. Tomizawa, S. Goto, T. Ishikawa and M. Yabashi (2013). 'Beamline, experimental stations and photon beam diagnostics for the hard x-ray free electron laser of SACLA'. In: *New J. Phys.* 15, p. 083035.

Turgut, Emrah, Chan La-o-vorakiat, Justin M. Shaw, Patrik Grychtol, Hans T. Nembach, Dennis Rudolf, Roman Adam, Martin Aeschlimann, Claus M. Schneider, Thomas J. Silva, Margaret M. Murnane, Henry C. Kapteyn and Stefan Mathias (2013). 'Controlling the Competition between Optically Induced Ultrafast Spin-Flip Scattering and Spin Transport in Magnetic Multilayers'. In: *Phys. Rev. Lett.* 110 (19), p. 197201.

Turgut, Emrah, Dmitriy Zusin, Dominik Legut, Karel Carva, Ronny Knut, Justin M. Shaw, Cong Chen, Zhensheng Tao, Hans T. Nembach, Thomas J. Silva, Stefan Mathias, Martin Aeschlimann, Peter M. Oppeneer, Henry C. Kapteyn, Margaret M. Murnane and Patrik Grychtol (2016). 'Stoner versus Heisenberg: Ultrafast exchange reduction and magnon generation during laser-induced demagnetization'. In: *Phys. Rev. B* 94 (22), p. 220408.

Unguris, J., D. T. Pierce, A. Galejs and R. J. Celotta (1982). 'Spin and Energy Analyzed Secondary Electron Emission from a Ferromagnet'. In: *Phys. Rev. Lett.* 49 (1), pp. 72–76.

Varnava, Nicodemos and David Vanderbilt (2018). 'Surfaces of axion insulators'. In: *Phys. Rev. B* 98 (24), p. 245117.

Vaterlaus, A., T. Beutler and F. Meier (1991). 'Spin-lattice relaxation time of ferromagnetic gadolinium determined with time-resolved spin-polarized photoemission'. In: *Phys. Rev. Lett.* 67 (23), pp. 3314–3317.

Verna, Adriano, Giovanni Stefani, Francesco Offi, Tatsuo Gejo, Yoshihito Tanaka, Kenta Tanaka, Tatsuru Nishie, Kiyonobu Nagaya, Akinobu Niozu, Ryosuke Yamamura, Taiga Suenaga, Osamu Takahashi, Hikaru Fujise, Tadashi Togashi, Makina Yabashi and Masaki Oura (2020). 'Photoemission from the gas phase using soft x-ray fs pulses: an investigation of the space-charge effects'. In: *New Journal of Physics* 22.12, p. 123029.

Vinai, G., C. Bigi, A. Rajan, M. D. Watson, T.-L. Lee, F. Mazzola, S. Modesti, S. Barua, M. Ciomaga Hatnean, G. Balakrishnan, P. D. C. King, P. Torelli, G. Rossi and G. Panaccione (2020). 'Proximity-induced ferromagnetism and chemical reactivity in few-layer VSe_2 heterostructures'. In: *Phys. Rev. B* 101 (3), p. 035404.

Wang, Yun-Peng and Meng-Qiu Long (2020). 'Electronic and magnetic properties of van der Waals ferromagnetic semiconductor VI_3'. In: *Phys. Rev. B* 101 (2), p. 024411.

Wang, Z., I. Gutiérrez-Lezama, N. Ubrig, M. Kroner, M. Gibertini, T. Taniguchi, K. Watanabe, A. Imamoğlu, E. Giannini and A.F. Morpurgo (2018). 'Very large tunneling magnetoresistance in layered magnetic semiconductor CrI_3'. In: *Nat. Commun.* 9, p. 2516.

Weber, A., F. Pressacco, S. Günther, E. Mancini, P. M. Oppeneer and C. H. Back (2011). 'Ultrafast demagnetization dynamics of thin Fe/W(110) films: Comparison of time- and spin-resolved photoemission with time-resolved magneto-optic experiments'. In: *Phys. Rev. B* 84 (13), p. 132412.

White, G.K. and M.L. Minges (1997). 'Thermophysical properties of some key solids: An update'. In: *Int. J. Thermophys.* 18.5, pp. 1269–1327.

Wieczorek, J., A. Eschenlohr, B. Weidtmann, M. Rösner, N. Bergeard, A. Tarasevitch, T. O. Wehling and U. Bovensiepen (2015). 'Separation of ultrafast spin currents and spin-flip scattering in Co/Cu(001) driven by femtosecond laser excitation employing the complex magneto-optical Kerr effect'. In: *Phys. Rev. B* 92 (17), p. 174410.

Wintle, H J (1997). 'Interpretation of atomic force microscope (AFM) signals from surface charge on insulators'. In: *Measurement Science and Technology* 8.5, pp. 508–513.

Xu, Changsong, Junsheng Feng, Hongjun Xiang and Laurent Bellaiche (2018). 'Interplay between Kitaev interaction and single ion anisotropy in ferromagnetic CrI_3 and $CrGeTe_3$ monolayers'. In: *npj Comput. Mater.* 4.57.

Xu, Gang, Hongming Weng, Zhijun Wang, Xi Dai and Zhong Fang (2011). 'Chern Semimetal and the Quantized Anomalous Hall Effect in $HgCr_2Se_4$'. In: *Phys. Rev. Lett.* 107 (18), p. 186806.

Xu, Yuanfeng, Zhida Song, Zhijun Wang, Hongming Weng and Xi Dai (2019). 'Higher-Order Topology of the Axion Insulator $EuIn_2As_2$'. In: *Phys. Rev. Lett.* 122 (25), p. 256402.

Yan, J., X. Luo, F. C. Chen, J. J. Gao, Z. Z. Jiang, G. C. Zhao, Y. Sun, H. Y. Lv, S. J. Tian, Q. W. Yin, H. C. Lei, W. J. Lu, P. Tong, W. H. Song, X. B. Zhu and Y. P. Sun (2019). 'Anisotropic magnetic entropy change in the hard ferromagnetic semiconductor VI_3'. In: *Phys. Rev. B* 100 (9), p. 094402.

Yang, Ke, Fengren Fan, Hongbo Wang, D. I. Khomskii and Hua Wu (2020). 'VI_3: A two-dimensional Ising ferromagnet'. In: *Phys. Rev. B* 101 (10), p. 100402.

Yang, T.Y., Q. Wan, D.Y. Yan, Z. Zhu, Z.W.. Wang, C. Peng, Y.B.. Huang, R. Yu, J. Hu, Z.Q. Mao, S. Li, S.A. Yang, H. Zheng, J. Jia, Y.G. Shi and N. Xu (2020). 'Directional massless Dirac fermions in a layered van der Waals material with one-dimensional long-range order'. In: *Nat. Mater.* 19 (1), pp. 27–33.

Yeh, J.J. and I. Lindau (1985). 'Atomic subshell photoionization cross sections and asymmetry parameters: $1 \leq Z \leq 103$'. In: *Atomic Data and Nuclear Data Tables* 32.1, pp. 1–155. ISSN: 0092-640X.

Yu, Rui, Xiao Liang Qi, Andrei Bernevig, Zhong Fang and Xi Dai (2011). 'Equivalent expression of $\mathbb{Z}_2$ topological invariant for band insulators using the non-Abelian Berry connection'. In: *Phys. Rev. B* 84 (7), p. 075119.

Yu, Rui, Wei Zhang, Hai-Jun Zhang, Shou-Cheng Zhang, Xi Dai and Zhong Fang (2010). 'Quantized Anomalous Hall Effect in Magnetic Topological Insulators'. In: *Science* 329.5987, pp. 61–64.

Zaiyao, Fei, Huang Bevin, Malinowski Paul, Wang Wenbo, Song Tiancheng, Sanchez Joshua, Yao Wang, Xiao Di, Zhu Xiaoyang, May Andrew F., Wu Weida, Cobden David H., Chu Jiun-Haw and Xu Xiaodong (2018). 'Two-dimensional itinerant ferromagnetism in atomically thin Fe_3GeTe_2'. In: *Nature Mater.* 17, pp. 778–782.

Zeisner, J., A. Alfonsov, S. Selter, S. Aswartham, M. P. Ghimire, M. Richter, J. van den Brink, B. Büchner and V. Kataev (2019). 'Magnetic anisotropy and spin-polarized

two-dimensional electron gas in the van der Waals ferromagnet $Cr_2Ge_2Te_6$'. In: *Phys. Rev. B* 99 (16), p. 165109.

Zeisner, J., K. Mehlawat, A. Alfonsov, M. Roslova, T. Doert, A. Isaeva, B. Büchner and V. Kataev (2020). 'Electron spin resonance and ferromagnetic resonance spectroscopy in the high-field phase of the van der Waals magnet $CrCl_3$'. In: *Phys. Rev. Materials* 4 (6), p. 064406.

Zhan, Qing-feng, Stijn Vandezande, Kristiaan Temst and Chris Van Haesendonck (2009). 'Magnetic anisotropies of epitaxial Fe/MgO(001) films with varying thickness and grown under different conditions'. In: *New Journal of Physics* 11.6, p. 063003.

Zhang, G. P. and W. Hübner (2000). 'Laser-Induced Ultrafast Demagnetization in Ferromagnetic Metals'. In: *Phys. Rev. Lett.* 85 (14), pp. 3025–3028.

Zhang, J. and R.D. Averitt (2014). 'Dynamics and Control in Complex Transition Metal Oxides'. In: *Annual Review of Materials Research* 44.1, pp. 19–43.

Zhang, Yi, Miguel M. Ugeda, Chenhao Jin, Su-Fei Shi, Aaron J. Bradley, Ana Martín-Recio, Hyejin Ryu, Jonghwan Kim, Shujie Tang, Yeongkwan Kim, Bo Zhou, Choongyu Hwang, Yulin Chen, Feng Wang, Michael F. Crommie, Zahid Hussain, Zhi-Xun Shen and Sung-Kwan Mo (2016). 'Electronic Structure, Surface Doping, and Optical Response in Epitaxial WSe2 Thin Films'. In: *Nano Letters* 16.4, pp. 2485–2491.

Zhou, Zhimou, Shishir Kumar Pandey and Ji Feng (2021). 'Dynamical correlation enhanced orbital magnetization in VI_3'. In: *Phys. Rev. B* 103 (3), p. 035137.

Zhu, Siyuan, Yukiaki Ishida, Kenta Kuroda, Kazuki Sumida, Mao Ye, Jiajia Wang, Hong Pan, Masaki Taniguchi, Shan Qiao, Shik Shin and Akio Kimura (2015). 'Ultrafast electron dynamics at the Dirac node of the topological insulator Sb_2Te_3'. In: *Scientific Reports* 5, p. 13213.

Zollner, Klaus, Martin Gmitra and Jaroslav Fabian (2020). 'Swapping Exchange and Spin-Orbit Coupling in 2D van der Waals Heterostructures'. In: *Phys. Rev. Lett.* 125 (19), p. 196402.

List of Publications

As of 21st November 2022

Refereed publications

A. De Vita†, T.T.P. Nguyen†, R. Sant, G.M. Pierantozzi, D. Amoroso, C. Bigi, V. Polewczyk, G. Vinai, L.T. Nguyen, T. Kong, J. Fujii, I. Vobornik, N.B. Brookes, G. Rossi, R.J. Cava, F. Mazzola, K. Yamauchi, S. Picozzi and G. Panaccione, *Influence of Orbital Character on the Ground State Electronic Properties in the van Der Waals Transition Metal Iodides VI_3 and CrI_3*, Nano Letters, 22, 17, 7034-7041 (2022).
DOI: 10.1021/acs.nanolett.2c01922.

J.S. Pelli Cresi, E. Spurio, L. Di Mario, P. O'Keeffe, S. Turchini, S. Benedetti, G.M. Pierantozzi, **A. De Vita**, R. Cucini, D. Catone and P. Luches, *Lifetime of Photogenerated Positive Charges in Hybrid Cerium Oxide-Based Materials from Space and Mirror Charge Effects in Time-Resolved Photoemission Spectroscopy*, J. Phys. Chem. C, **126**, 27, pp. 11174-11181 (2022).
DOI: 10.1021/acs.jpcc.2c02148.

G. M. Pierantozzi†, **A. De Vita**†, C. Bigi, X. Gui, H.J. Tien, D. Mondal, F. Mazzola, J. Fujii, I. Vobornik, G. Vinai, A. Sala, C. Africh, T.L. Lee, G. Rossi, T.R. Chang, W. Xie, R.J. Cava and G. Panaccione, *Evidence of magnetism-induced topological protection in the axion insulator candidate* $EuSn_2P_2$, PNAS **119**, 4, e2116575119 (2022).
DOI: 10.1073/pnas.2116575119.

G. M. Pierantozzi, G. Vinai, A.Y. Petrov, **A. De Vita**, F. Motti, V. Polewczyk, D. Mondal, T. Pincelli, R. Cucini, C. Bigi, I. Vobornik, J. Fujii, P. Torelli, F. Offi, G. Rossi, G. Panaccione and F. Borgatti, *Evidence of Robust Half-Metallicity in Strained Manganite Films*, J. Phys. Chem. C **125**, 26, 14430–14437 (2021).
DOI: 10.1021/acs.jpcc.1c02323.

M. Sygletou, S. Benedetti, M. Ferrera, G.M. Pierantozzi, R. Cucini, G. Della Valle, P. Carrara, **A. De Vita**, A. Di Bona, P. Torelli, D. Catone, G. Panaccione, M. Canepa and F. Bisio, *Quantitative Ultrafast Electron-Temperature Dynamics in Photo-Excited Au Nanoparticles*, Small **17**, 2100050 (2021).
DOI: 10.1002/smll.202100050.

R. Cucini, T. Pincelli, G. Panaccione, D. Kopic, F. Frassetto, P. Miotti, G.M. Pierantozzi, S. Peli, A. Fondacaro, A. De Luisa, **A. De Vita**, P. Carrara, D. Krizmancic, D.T. Payne, F. Salvador, A. Sterzi, L. Poletto, F. Parmigiani, G. Rossi and F. Cilento, *Coherent narrowband light source for ultrafast photoelectron spectroscopy in the 17-31 eV photon energy range*, Struct. Dyn. **7**, 014303 (2020).
DOI: 10.1063/1.5131216.

† These authors contributed equally.

Publications under review

F. Mazzola, S. Enzner, P. Eck, C. Bigi, G.M. Pierantozzi, **A. De Vita**, P. Carrara, J. Fujii, P.D.C. King, G. Vinai, P. Orgiani, C. Cacho, M.D. Watson, G. Rossi, I. Vobornik, T. Kong, D. Di Sante, G. Sangiovanni and G. Panaccione, *Observation of termination-dependent topological connectivity in a magnetic Weyl kagome-lattice*, submitted.

Publications in preparation

A. De Vita, R. Cucini, A.M. Finardi, T. Pincelli, F. Sirotti, J. Fujii, G. Rossi, G. Panaccione and G.M. Pierantozzi, *Ultrafast near Fermi d–band dynamics and spin character in Fe(001)*, in preparation.

R. Sant, **A. De Vita**, V. Polewczyk, G.M. Pierantozzi, F. Mazzola, G. Vinai, G. van der Laan, N.B. Brookes and G. Panaccione, *Origin of the magnetic Mott insulating phase in VI_3 van der Waals ferromagnet*, in preparation.

G.M. Pierantozzi, **A. De Vita**, R. Cucini, S. Fiori, C. Dri, V. Polewczyk, S. Park, F. Cadiz, L. Martinelli, G. Panaccione and F. Sirotti, *Electron Spin dynamics in GaAs studied with short laser excitation*, in preparation.

Acknowledgments

> Centoundici anni di vita in mezzo a gente così straordinaria ed ammirevole non sono sufficienti. [...] Conosco la metà di voi solo a metà; e nutro, per meno della metà di voi, metà dell'affetto che meritate.
>
> Bilbo Baggins, *La Compagnia dell'Anello*

Scrivere la tesi è il passo finale che riassume il lavoro durante l'intero arco dei tre anni di dottorato: per questo il suo contenuto è rigorosamente scientifico, fatto di ipotesi, dati e discussioni. Ciò che necessariamente non include sono i contributi "soft" che si sono accumulati nel corso dei tre anni di dottorato: le relazioni interpersonali, il lato parlato, ascoltato e vissuto della scienza. Dato che penso di essere molto prodigo di ringraziamenti a voce, ma parco di espressioni scritte, sapendo che *Verba volant, scripta manent* questa sezione è riservata proprio per rendere giustizia a ciò che a volte nelle tesi passa sotto silenzio.

Il primo ringraziamento va senza dubbio a Giorgio: il tuo perenne supporto non si è mai interrotto, nonostante i vortici di impegni istituzionali al quale, specialmente nell'ultimo periodo, sei stato sottoposto. Per ogni necessità e richiesta, dalle approfondite discussioni sul caro ferro fino ai ritmi serrati per la correzione della tesi, sei sempre stato disponibile, senza mai però imporre decisioni dall'alto. Mi ritengo molto fortunato di aver avuto grande libertà decisionale in laboratorio, con la possibilità di provare (e sbagliare) indipendentemente; e al contempo un definitivo test di Litmus sulla bontà dei miei risultati e sulla mia conoscenza della fisica, grazie alle tue domande e osservazioni sempre precise.

Allo stesso modo, non posso esimermi dal ringraziare di tutto cuore Giancarlo, anima santa che ha dovuto avere a che fare giorno per giorno con il circo equestre che è stato il mio progetto di ricerca. Grazie infinite per il conforto nei giorni in cui mi è sembrato di interpretare una grottesca riedizione di Hollywood Party nel ruolo di Hrundi Bakshi; grazie per la pazienza con cui hai approcciato le nostre chiacchierate, seguendo poi da lontano le mie decisioni e dimostrandomi che alla fine avevi ragione tu; grazie per la occasionale fermezza con cui hai riportato i miei progetti sulla giusta carreggiata prima che si perdessero; e, non in maniera secondaria, grazie per la tua sterminata conoscenza della fisica, che mi ha insegnato a ricercare eleganza e semplicità anche nella complessità e ad andare al vero cuore delle questioni.

Non posso esprimere quanto sia grato a tutti gli Sprinters: innanzitutto Gian, fondamentale pilastro che ha condiviso con me frustrazioni e dolori della vita di laboratorio, prendendone su di sé la porzione più grande, e mi ha incoraggiato verso sempre maggiore rigore sperimentale; Riccardo, del quale, oltre a una competenza straordinaria, ho potuto apprezzare preziosissimi insegnamenti sul funzionamento del mondo scientifico, sul futuro e sulla musica, e ancor più memorabili scambi di opinioni su B-movie e Steven Seagal; Pietro e Marta, i Cip e Ciop del TG, aperti a nuove proposte anche sotto forma di brutti scherzi (sapete di cosa sto parlando) e che hanno condiviso con me l'indignazione di fronte a una specifica serie TV; Sara, che è stata sempre disponibile all'ascolto e mi ha insegnato a dare il giusto peso alle cose ("Stai calmo, Ale!"); e ovviamente Michele, il nostro nuovo acquisto, il cui entusiasmo e dedizione alle sue attività, che siano scienza, corsa o scacchi, è sempre contagioso.

A tutti questi va aggiunto un grande grazie a Tom, Sprinter emerito, per il supporto che mi ha continuativamente offerto: da quando ero uno studente a quando ho concluso il percorso del dottorato, il tempo che ha speso per me non potrà mai essere ripagato abbastanza.

Devo poi sinceramente ringraziare Andrea Fondacaro, il nostro "calabrese di Düsseldorf", non unicamente per la sua impressionante efficienza e professionalità, ma anche e soprattutto per il suo profondo lato umano e il suo fortissimo impegno per la società, che spesso mi ha fatto meditare e imparare.

Un grande ringraziamento va ovviamente a tutti i cugini del gruppone di APE LE e HE: Ivana, Jun (五度も十度も、その機合の人をもて和を入て、教訓正路にあるべし。), Federico che con ogni probabilità ha una procedura anche per scrivere articoli automaticamente, Chiara che è riuscita a sopravvivere a due beamtime con me senza fuggire, Debashis che è impossibile vedere demoralizzato; Giovanni che trova un momento per ogni cosa e la cui pazienza non conosce davvero limiti, Vincent che è diventato più italiano di me e a cui (insieme all'adorabile Barbara) auguro bon courage per la sua nuova avventura a Grenoble; Luca, Federico, Piero, Sasha, Pasquale, Sandeep e altri che sto dimenticando ma meriterebbero di sicuro una menzione. È difficile trovare un gruppo così numeroso di persone che è più facile chiamare amici che colleghi.

Grazie al fenomenale gruppo di Giuseppe Cautero: Rudi, Gabriele e Carlo di certo avrebbero potuto sabotare ogni nostro sforzo sul Mott con il pigro movimento di un solo dito, ma con straordinaria tenacia e dedizione si sono impegnati al nostro fianco per migliorare sempre di più il laboratorio, contagiandoci con la loro positività e allegria a ogni visita. E un grazie va anche a Federico Cilento, le cui risposte sibilline e ammantate di mistero (ma sempre condite dal suo caratteristico *humour*) portano sempre spunti di riflessione, e a tutto il gruppo T-Rex: Denny, Manuel e Wibke, di sicuro grazie a voi il lavoro di laboratorio è molto più leggero!

Grazie agli utenti esterni con cui ho avuto il piacere di lavorare, su Sprint e non solo: la categoria degli utenti di una beamline, solitamente bistrattata, merita invece i ringraziamenti di chi, come me, ha molto da imparare. Maria Sygletou e il gruppo di Francesco Bisio; Daniele Catone, Stefano Turchini e tutta la loro brigata, con i quali è impossibile non trovarsi bene; Giovanni Zamborlini e le sue castagne al bake-out; Francesco Borgatti e le sue mail motivazionali della domenica pomeriggio; Alberto Brambilla e la sua gentilezza dentro e fuori il lavoro; Roberto Sant e i beamtime condivisi a Elettra e ESRF; e soprattutto Fausto Sirotti, un vero e proprio uragano in forma di uomo, senza il cui fondamentale contributo Sprint sarebbe un laboratorio molto diverso.

Gli anni a Trieste non hanno rappresentato solo duro lavoro. La scienza al sincrotrone costituisce una parte della mia crescita personale, mentre il resto è attribuibile alle straordinarie persone che ho incontrato: molto di ciò che ho acquisito durante questo pe-

riodo è dovuto a loro. Per questo, un immenso grazie va agli amici della 7c, che in questi anni sono stati compagni di avventure dentro e fuori la scherma: Luca il Sensei, che si sobbarca il compito di coltivare e indirizzare il nostro dispersivo entusiasmo; Giorgio il sergente, instancabile e diabolico architetto d'ingegno di esercizi e forme che non hanno senso finché l'ultimo pezzo del puzzle non si incastra al suo posto; Davide il guerriero, la cui maestria sul campo è eguagliata solo da quella sul tavolo da gioco del GM; Gian Maria il motivatore, vulcano di proposte e di attività più o meno serie; Gil la risoluta, di cui vorrei possedere un decimo della grinta e determinazione; Riccardo il lacone, le cui pochissime parole sempre ben calibrate non mancano mai di strapparmi una risata; e poi Žiga, Mario, Giulio, Ermanno, Francesco, Daniele, Paolo e gli altri, tutti in pari ordine di importanza.

Grazie a Jacopo per le conversazioni su argomenti improponibili a ore improponibili, e a Lorenzo con il quale si può perdere i contatti per mesi e rivedersi come se non fosse passato un giorno. Giacomo, che dire? La più longeva amicizia della mia vita, che procede intatta nonostante la distanza che ci separa da molti anni: grazie per la tua arguzia e le tue osservazioni mai banali. Grazie a Seba e Ale, che ormai da più di dieci anni si spendono per trascinarmi di fronte a una birra media, con scarso successo (mio) e grande disappunto (loro), ma della cui compagnia non mi priverei mai quando rientro a casa. Grazie a Silvia, amica senza compromessi, a cui auguro ogni bene nella nuova vita insieme a Davide. Grazie a Claudio, esule come me ma con il quale i contatti e l'affinità per il *nonsense* non si sono mai persi. Grazie a Nico, collega dall'inizio alla fine dell'università con il quale ho condiviso infinite soddisfazioni e infinite+1 frustrazioni. E poi grazie a Giacomo, a Chiara, a Gabri, a Pietro e Giulia, a Filippo, a Davide, a Marco, a tutti quegli amici che conservo da anni e che spero di non perdere mai.

Non posso non ringraziare anche il professor Fumagalli e la sua acuta sensibilità, appena nascosta sotto una scorza che solo superficialmente potrebbe sembrare ruvida: i suoi libri sono stati fedeli compagni nel difficile periodo che è stato la pandemia, e nelle nostre chiacchierate più che sui banchi di scuola ho veramente compreso di avere di fronte una persona straordinaria.

Tutta la mia gratitudine va alla mia famiglia che non ha mai smesso di incoraggiarmi e starmi vicino sin dall'inizio di questa mia trasferta triestina. Grazie mamma e papà, supporti incrollabili, per avermi sempre spinto a volare in alto, per avermi dato l'opportunità di scegliere liberamente il mio futuro e per non aver mai dubitato delle mie decisioni; grazie nonno Giorgio e nonna Sissi, che con tutti i vostri gesti mi date la certezza di essere nei vostri pensieri; grazie agli zii e ai cugini che mai smettono di interessarsi e informarsi sulla mia vita a Trieste e sulle mie attività future; e in particolare allo zio Marco, che penso più di tutti abbia beneficiato del mio interesse verso il triestino ("Ulo!"). Vorrei anche dedicare un ricordo a Sandro, alla zia Grazia e al nonno Lele: avrei voluto avervi accanto, e nonostante la vita abbia deciso altrimenti vi conserverò sempre nel mio cuore.

E infine riservo l'ultimo grazie per Liliana, anche se non esistono abbastanza parole per farlo. Per prima mi hai fatto conoscere Trieste, e i giorni che lì abbiamo condiviso sono stati i più belli e felici. Mi sento pieno di gioia per aver scoperto e continuare a scoprire tutto quello che ci accomuna, e anche per quello che ci distingue e che rende inaspettato e straordinario ogni momento con te. Grazie a te posso guardare al futuro, qualunque esso sia, con un sorriso, perché so che ti avrò accanto. La tua dolcezza e la fiducia che hai in me hanno reso questi anni la più meravigliosa delle esperienze.